

## NEAR-INFRARED STRUCTURE OF FAST AND SLOW ROTATING DISK GALAXIES

ANDREW SCHECHTMAN-ROOK<sup>1</sup>, MATTHEW A. BERSHADY<sup>1</sup>

*Draft version August 18, 2018*

### ABSTRACT

We investigate the stellar disk structure of six nearby edge-on spiral galaxies using high-resolution  $JHK_s$ -band images and 3D radiative transfer models. To explore how mass and environment shape spiral disks, we selected galaxies with rotational velocities between  $69 < V_{\text{rot}} < 245 \text{ km sec}^{-1}$ , and two with unusual morphologies. We find a wide diversity of disk structure. Of the fast-rotating ( $V_{\text{rot}} > 150 \text{ km sec}^{-1}$ ) galaxies, only NGC 4013 has the super-thin+thin+thick nested disk structure seen in NGC 891 and the Milky Way, albeit with decreased oblateness, while NGC 1055, a disturbed massive spiral galaxy, contains disks with  $h_z \lesssim 200 \text{ pc}$ . NGC 4565, another fast-rotator, contains a prominent ring at a radius  $\sim 5 \text{ kpc}$  but no super-thin disk. Despite these differences, all fast-rotating galaxies in our sample have inner truncations in at least one of their disks. These truncations lead to Freeman Type II profiles when projected face-on. Slow-rotating galaxies are less complex, lacking inner disk truncations and requiring fewer disk components to reproduce their light distributions. Super-thin disk components in undisturbed disks contribute  $\sim 25\%$  of the total  $K_s$ -band light, up to that of the thin-disk contribution. The presence of super-thin disks correlates with infrared flux ratios; galaxies with super-thin disks have  $f_{K_s}/f_{60\mu\text{m}} \leq 0.12$  for integrated light, consistent with super-thin disks being regions of on-going star-formation. Attenuation-corrected vertical color gradients in  $(J - K_s)$  correlate with the observed disk structure and are consistent with population gradients with young-to-intermediate ages closer to the mid-plane, indicating that disk heating—or cooling—is a ubiquitous phenomenon.

*Subject headings:* galaxies: spiral – galaxies: stellar content – galaxies: individual (NGC 522, NGC 891, NGC 1055, NGC 4013, NGC 4144, NGC 4244, NGC 4565)

### 1. INTRODUCTION

Determining the vertical structure of spiral disks is central to understanding how they form and evolve over time. The notion of galaxy formation as a monolithic gravitational collapse (Eggen et al. 1962) has long since fallen by the wayside in favor of a hierarchical buildup of mass that comes naturally in a cold dark-matter cosmological scenario ( $\Lambda$ CDM). However, in the context of the disk galaxies like the Milky Way that we see today, the two scenarios may not be too dissimilar if the bulk of the mass assembly takes place early or very slowly. What matters is the detailed interplay between the initial mass build-up, angular momentum, and cooling of the gaseous disk; and the subsequent kinematic heating of the stellar disk through internal dynamical interactions, instabilities, and external mergers (Walker et al. 1996; Abadi et al. 2003). These conditions set the physical parameters of the disks (for discussion see Bird et al. 2013).

Where  $\Lambda$ CDM is particularly helpful is in its statistical prescription for the lumpiness and history of mass accretion; where it is particularly uninformative concerns the coupling of the baryons to the dark matter, and their processing into stars. Consequently, a detailed picture of galaxy formation requires observational constraints and independent (dynamical) arguments. For example, we know that thick disks are forming at  $z \sim 2$  (Förster Schreiber et al. 2009), although it is less clear if these are related to the fairly ubiquitous thick disk com-

ponents that we see in nearby galaxies like the Milky Way today (e.g., Yoachim & Dalcanton 2006, Comerón et al. 2011c). Any very thin disks that we observe today may have formed recently, since such disks are prone to disruption even in minor satellite accretion events (Purcell et al. 2009). These issues highlight the uncertainties in our knowledge of the assembly and dynamical evolution of disks, and point to the need to empirically characterize the fossil record in today’s disks.

The vertical distribution of mass and different stellar populations are also critical variables in efforts to break the disk-halo degeneracy and isolate the contributions of dark and luminous matter to the gravitational potential of spiral galaxies (Bershady et al. 2010a,b). While recent efforts have indicated that galaxy disks contribute significantly less than the theoretical maximum (contradicting the hypothesis of ‘disk maximality’; Bershady et al. 2011; Westfall et al. 2011; Martinsson et al. 2013) to the gravitational potential, if significant luminosity is contained in very thin disks it would serve to increase the estimate of disk maximality from kinematic measurements of face-on disks. This fact was part of the initial motivation for the current study.

In the Milky Way (MW) the distribution of stars as a function of distance from the disk midplane is relatively well known for stars of different spectral types in the solar cylinder, e.g., Aumer & Binney (2009), and more broadly within the disk for G-dwarfs of different abundance and metallicity (e.g., Bovy et al. 2012). However, resolved stellar population studies are currently relegated to the MW and only the brightest stars in very nearby galaxies. A study of nearby, edge-on galaxies (Seth et al.

<sup>1</sup> University of Wisconsin, Department of Astronomy, 475 N. Charter St., Madison, WI 53706; andrew@astro.wisc.edu

2005) also find evidence for vertical population gradients, but their study does not contain any fast-rotating ( $V_{\text{rot}} > 130 \text{ km s}^{-1}$ ) disks. Because of the large optical midplane dust attenuation found in all fast-rotating edge-on spiral galaxies, the MW is the *only* galaxy of this type for which we have an unambiguous (albeit radially limited) sampling of stellar population gradients near the midplane. Consequently our understanding of the midplane structure of spiral galaxy disks is incomplete at best. This has necessarily led to simplified models of these systems which tend to focus on the characterization of the more easily visible thicker disk components.

We have undertaken a study of the vertical structure of nearby spiral galaxies using high-resolution ( $\leq 1''$  FWHM) near-infrared (NIR) imaging, specifically focused on the light distribution near the mid-plane. In order to probe the light distribution at these small heights, we have employed state-of-the-art radiative transfer (RT) models to estimate dust attenuation corrections. In Schechtman-Rook & Bershadsky (2013, hereafter Paper 1) we demonstrated our methods, constructing full spectral energy distribution (SED) RT models of the well-studied MW-like galaxy NGC 891. These models contained multiple stellar populations as well as fractal dust clumps, and were used to compute a general relationship between infrared color and attenuation. When applying these corrections to NIR data for NGC 891, we found not only a super-thin disk ( $h_z \sim 100 \text{ pc}$ ) but also an inner disk truncation, an exponential-like bar, and a nuclear disk.

In this work we apply an improved version of this procedure to a small sample of 6 nearby edge-on spiral galaxies, including three massive spirals with  $V_{\text{rot}} > 150 \text{ km s}^{-1}$  and morphological similarity to NGC 891 (NGC 522, 4013, and 4565), one massive spiral with disturbed morphology (NGC 1055), and two low-mass systems with  $V_{\text{rot}} < 100 \text{ km s}^{-1}$  (NGC 4144 and 4244). The latter are known to lack prominent dust lanes (Dalcanton et al. 2004) and therefore may possess dramatically different disk structure than seen in more massive spiral galaxies. While this is a modest sample, it does span an intentionally broad range of parameters for star-forming disk galaxies, and constitutes a large fraction of edge-on galaxies that are close enough to resolve at or below the 70 pc level (the super-thin disk scale-height of NGC 891 from (Schechtman-Rook & Bershadsky 2013)) with extant wide-field NIR imaging facilities.

The paper is organized as follows. In Section 2 we describe the reduction process for our data. Section 3 contains significant revisions to our dust attenuation estimation method based on (a) an improved coupling to stellar population synthesis to our RT models; and (b) a new RT model more suitable to the dust and stellar geometries of the slow-rotating galaxies in our samples (detailed in the Appendix). This section also presents the attenuation-corrected light profiles of our sample. In Section 4 we compare the apparent and corrected near-infrared colors and their gradients in the context of expectations from stellar population synthesis models for the purpose of verifying our attenuation corrections. The multi-component modeling of the two-dimensional light profiles for each galaxy is detailed in Section 5. In Section 6 we revisit the inferred color gradients in the context of a multi-component disk populations and disk heating,

and characterize the oblateness and luminosity contributions of different disk components in the context of disk maximality estimates. The face-on appearance of the sample and indirect methods for inferring the presence of super-thin disks in spiral galaxies are also presented in this section. The results of our study are summarized in Section 7. Note that all magnitudes used in this work are in the Vega system unless otherwise specified.

## 2. DATA

As in Paper 1, our data come from the WIYN<sup>2</sup> High-resolution InfraRed Camera (WHIRC; Meixner et al. 2010) as well as archival IRAC observations<sup>3</sup>. Our basic reduction procedure is mostly unchanged from Paper 1, which can be referred to for details. In brief, we first trim, Fowler correct, and linearity correct the images. Then we use temporally adjacent images to compute and subtract a sky background. All sky-subtracted images for a given galaxy in each filter are combined to produce a mosaic, which is then used to create a mask of all foreground stars, background galaxies, and the light from the target galaxy itself. The mask is applied to the individual images and the background subtraction is repeated, which produces a more accurate estimate for the sky level. Finally, the mosaics are post-processed to obtain astrometric and photometric calibrations. A log of our observations is presented in Table 1. We have made some important improvements to parts of our reduction scheme, specifically in our foreground subtraction, cosmic-ray cleaning, error propagation, and the masking of residual image gradients. These improvements are detailed in the following sections. False-color RGB images of our final mosaics are compared to *Sloan Digital Sky Survey* (SDSS; York et al. 2000) *gri* color images in Figure 1.

### 2.1. Foreground Subtraction

In Paper 1, we found that NGC 891 was large enough on the sky to force the use of dedicated sky frames. These provided very accurate sky subtraction at the cost of a  $\sim 50\%$  penalty in observing efficiency. Some galaxies in our sample, however, are small enough that the vertical scales we wish to probe are smaller than half the size of WHIRC. Therefore, using a careful dither pattern which placed the galaxy on alternating sides of the chip (similar to the method used by Dalcanton & Bernstein 2000) we avoided the need for dedicated sky frames in these cases and doubled our efficiency. Galaxies with which we were able to use this technique are noted in Table 1.

While the main purpose of this specialized dither pattern was to “chop” the target galaxy to different sides of the detector, we also superimposed small ( $\sim 3''$ ) offsets along both dither axes. These offsets are small enough to subtract extended emission from the galaxy on the “wrong” half of the detector, but large enough to preserve stellar sources (masked from the sky image). Due to the small size of the WHIRC field and the fact that most of our target galaxies are in the North Galactic

<sup>2</sup> The WIYN Observatory is a joint facility of the University of Wisconsin-Madison, Indiana University, Yale University, and the National Optical Astronomy Observatory.

<sup>3</sup> AORs 31044096, 37342720, 42245120, 14479104, 3626240, and 3628032.

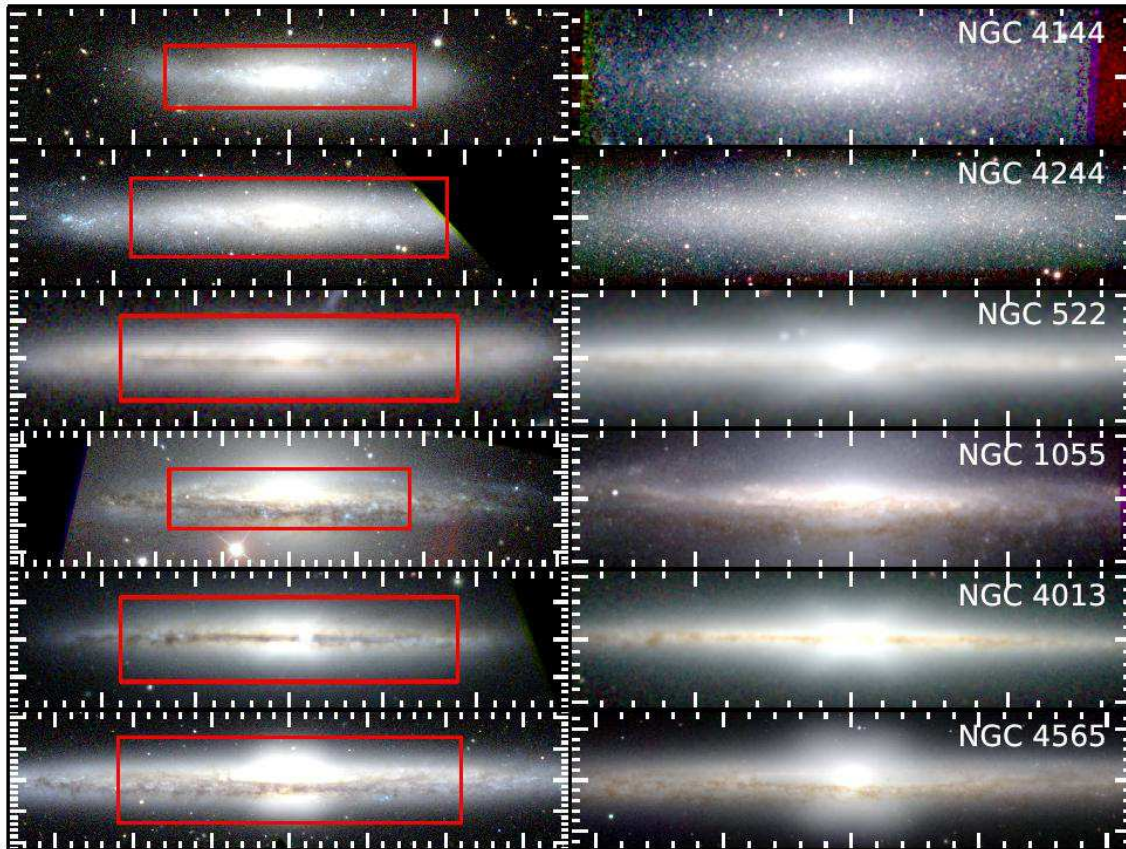


FIG. 1.— SDSS gri' (left panel) and our full WHIRC JHK<sub>s</sub> (right panel) images of the galaxies in our sample, sorted by increasing  $V_{\text{rot}}$ . Red boxes in the SDSS images indicate WHIRC FOV. Tickmarks show projected physical distance in increments of 1 kpc (x axis) and 400 pc (y axis).

Cap, having fluxes for these stars was crucial for computing our flux calibration.

Finally, the iterative relaxation algorithm used to interpolate over regions with zero good foreground pixels in Paper 1 was replaced by a third order polynomial fit to the pixels around each region where there was no overlap in the sky images. This was done mainly as a computational speed boost; the iterative relaxation algorithm slows down dramatically when overlap-free regions are more than a few pixels in size.

### 2.1.1. IRAC Foregrounds

All of the IRAC images had non-zero foregrounds, and therefore also needed foreground subtraction. Unlike in Paper 1, the foreground levels appeared to be generally constant offsets, and were removed by first computing a clipped mean flux in a region well away from the galaxy using the IRAF<sup>4</sup> task IMSTAT and then subtracting this value from the entire image.

### 2.2. Cosmic Ray Cleaning

In Paper 1 we did not perform a dedicated cosmic ray cleaning, relying on the process of making the mosaics to average out any cosmic rays. In visual inspections of the

<sup>4</sup> IRAF is distributed by the National Optical Astronomy Observatory, which is operated by the Association for Research in Astronomy, Inc. under cooperative agreement with the National Science Foundation.

final mosaics of the other galaxies in our sample, however, it was apparent that for at least some images there were still visible cosmic rays and/or chip defects. Therefore, we added two algorithms we developed for our post-processing steps to remove these features from our final images. These algorithms are based on the IRAF CR-CLEAN program, but allow for iterative cleaning, better statistical control over thresholding, interactive inspection, and control over pixel replacement using simple image arithmetic and pixel masks to replace bad pixels with linearly interpolated values from neighboring regions.

### 2.3. Error Propagation

Despite a careful and thorough propagation of different sources of errors for NGC 891 in Paper 1, we neglected to account for data covariance that naturally arises in registered, coadded data. Here we have added the suitable correction for the errors that come from the correlation of adjacent pixels in the geometric transformation and mosaic-making steps of our reduction. This addition results in slightly ( $\sim 1.36$  times) larger errors, especially in regions of low surface brightness. While likely not an issue for any of our fitting (considering that our fits were clearly not biased by the low surface brightness data) in Paper 1, it is something to be aware of when inspecting those results.

### 2.4. Image Masking

TABLE 1  
SUMMARY OF OBSERVATIONS AND IMAGE MOSAIC QUALITY

Galaxy	Distance <sup>a</sup> (Mpc)	V <sub>rot</sub> <sup>b</sup> (km s <sup>-1</sup> )	Filter	Exposure Time (s)		Seeing FWHM <sup>e</sup>	$\mu(S/N=10)^f$ (mag arcsec <sup>-2</sup> )	$\mu(\text{lim})^g$ (mag arcsec <sup>-2</sup> )	Pointings <sup>h</sup>	Dither Pattern <sup>i</sup>
				Individual <sup>c</sup>	Total <sup>d</sup>					
NGC 522	46.1	169	J	160	640	0''.5	18.1±0.1	23.1	1	A
	...	...	H	100	800	0''.6	17.4±0.1	22.2	1	A
	...	...	K <sub>s</sub>	40	6600	0''.6	16.5±0.1	21.9	1	A
NGC 1055	16.6	181	J	100	800	0''.6	18.0±0.0	22.8	1	S
	...	...	H	100	600	0''.7	17.2±0.0	22.1	1	S
	...	...	K <sub>s</sub>	40	12400	0''.7	16.7±0.2	20.7	2	S
NGC 4013	18.6	182	J	100	700	0''.7	18.1±0.1	22.9	2	A
	...	...	H	80	1040	0''.9	17.2±0.1	22.4	2	A
	...	...	K <sub>s</sub>	40	2640	0''.7	16.4±0.1	21.8	2	A
NGC 4144	6.6	69	J	60	900	0''.7	17.7±0.5	22.9	1	A
	...	...	H	60	1380	0''.6	17.2±0.3	23.0	1	A
	...	...	K <sub>s</sub>	40	7240	0''.6	16.2±0.8	21.9	1	A
NGC 4244	4.1	89	J	60	2100	0''.6	17.9±0.2	22.2	3	A
	...	...	H	60	3720	0''.6	17.4±0.3	21.5	3	A
	...	...	K <sub>s</sub>	40	11520	1''.0	15.9±1.4	...	3	S
NGC 4565	11.7	245	J	100	1000	0''.7	17.9±0.1	23.0	3	S
	...	...	H	100	1000	0''.8	17.1±0.1	21.5	3	S
	...	...	K <sub>s</sub>	40	3200	0''.6	16.4±0.1	22.1	3	S

<sup>a</sup> Distances come from the NASA/IPAC Extragalactic Database.

<sup>b</sup> From HyperLEDA (Paturel et al. 2003), <http://leda.univ-lyon1.fr>.

<sup>c</sup> Exposure time for a single exposure. These observations were taken during several observing runs that spanned the period of time between October 2010 and April 2012. The changing individual exposure times for the J and H filters are largely due to how our observing strategy evolved over that time.

<sup>d</sup> Total exposure time over the entire galaxy, not including frames that were removed during reduction due to image artifacts or other issues.

<sup>e</sup> Most galaxies required multiple pointings to obtain full coverage. Quoted seeing values are *worst case*; in several cases there are regions of the final image with  $\geq 0''.1$  better seeing than what is listed here.

<sup>f</sup> The surface brightness of a pixel at S/N=10.

<sup>g</sup> Limiting surface brightness due to large-scale image gradients. No value indicates images where gradients were not apparent. Limits used for masking, as noted in Section 2.4, are 1.2 mag arcsec<sup>-2</sup> brighter than these values.

<sup>h</sup> The number of observed positions along the major axis of the galaxy

<sup>i</sup> Our sky subtraction methodology: ‘A’ denotes the pattern which placed the galaxy on alternate sides of the detector, while ‘S’ indicates that dedicated sky dithers were used.

All images are masked to remove both foreground and background contaminants. This masking is done by hand, and aims to err on the side of mask-inclusion when it was unclear whether an apparent source was part of the galaxy or not. For NGC 4144 and 4244, which contain many discrete star clusters (or possibly even individual super-giant stars) across their disks, the false-color WHIRC images were consulted to aid in identifying objects to mask. Specifically, background galaxies visible through the disk had similar appearances to the star clusters but were generally much redder.

As a necessary compromise in order to subtract the foreground from galaxies which we dithered between sides of the detector to eliminate the need for dedicated sky frames, any faint extended galaxy light contaminating the ‘sky’ half of the WHIRC field was identically set to zero by the sky-subtraction process. For these galaxies we therefore masked out such regions of the final mosaics in order not to introduce any artificial high-latitude truncations caused by our sky subtraction.

Even with this effort, in most final mosaics there were still faint brightness gradients over portions of the field. We measured the magnitude of these gradients by hand over  $\sim 100$  arcsec<sup>2</sup> regions away from the galaxies, and found variations of  $\sim 1$  DN. We then computed the corresponding surface-brightness values, which are given in Table 1 as  $\mu(\text{lim})$ . For subsequent analysis, we mask out any pixels below three times this value (i.e.,  $\mu > \mu(\text{lim}) - 1.2$ ) to avoid regions of these images which

could be dominated by these erroneous features. Generally these gradients were at much lower surface brightness than regions of interest in the galaxy, and largely impact the vertical extent out to which we can constrain thick, low-surface-brightness disk components.

## 2.5. Image Quality and Depth

Table 1 provides information about the overall quality and depth of our sample images. Generally the resolution of our mosaics is excellent, with 50% at seeing  $\leq 0''.6$  and  $> 80\%$  having seeing  $\leq 0''.7$ . NGC 4244, the only galaxy in our sample with seeing at or above 1 arcsecond, happens to be the most nearby galaxy (D=4.1 Mpc), making excellent resolution less of a necessity. Also note that all of our data on NGC 522, our most distant target, has seeing  $\leq 0''.6$ , some of the best in our sample.

For any given filter we achieve fairly uniform depth across each mosaic and between sources. To provide a quantitative estimate on our depth we compute the surface brightness corresponding to a S/N $\approx 10$  in a single pixel. We compute statistics on all pixels with  $9.9 < S/N < 10.1$  to estimate the mean and standard deviation of this surface brightnesses value, given as  $\mu(S/N=10)$  in Table 1. We do the statistics in flux units before converting to surface brightness, and report the mean because it was always brighter than the median and is thus a more conservative estimate. These values are relatively bright, but note that each WHIRC pixel is only  $\approx 0.01$  arcsec<sup>2</sup>. When producing the vertical pro-

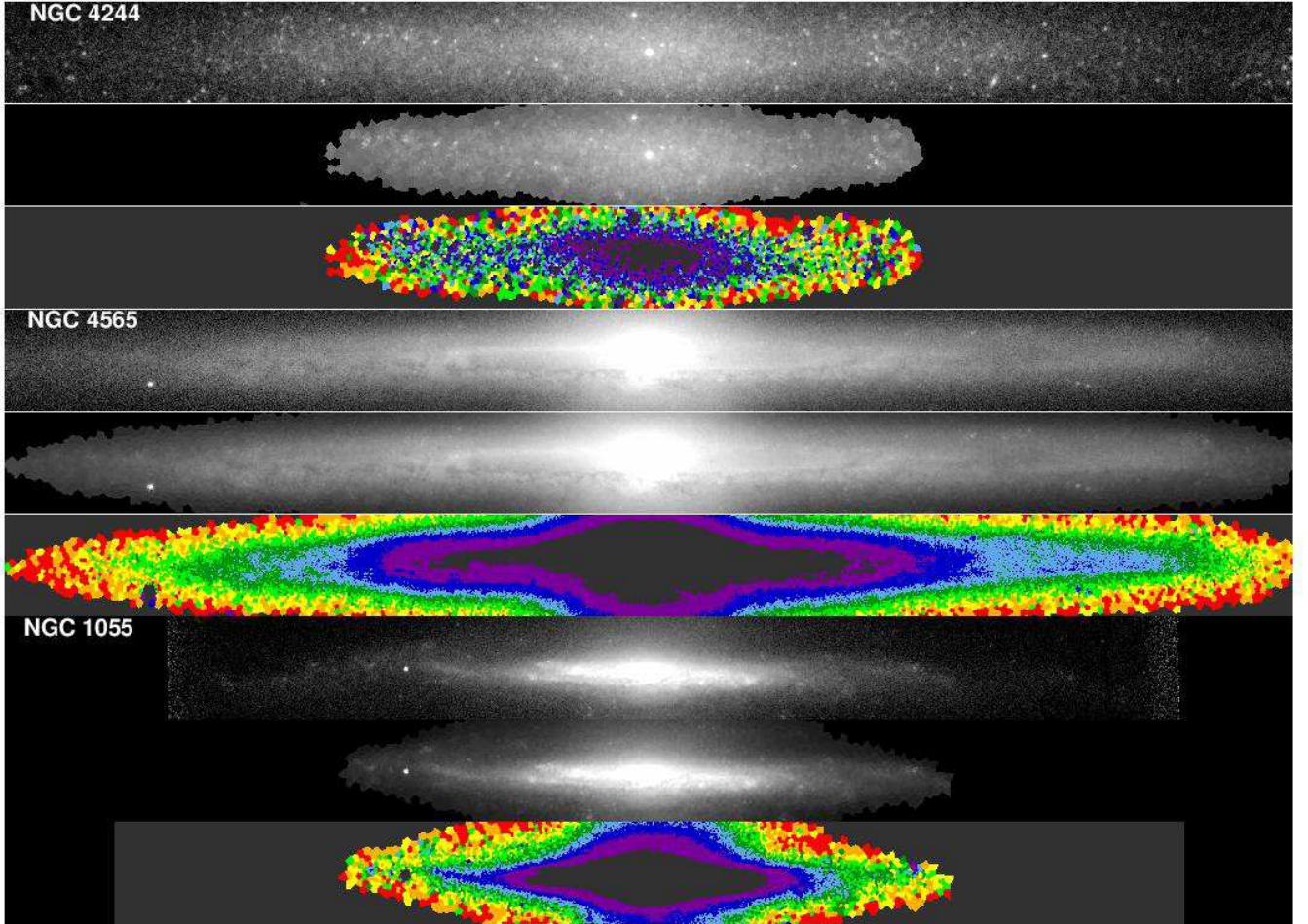


FIG. 2.— Voronoi binning applied to final  $K_s$ -band mosaics to achieve  $S/N=20$  per bin for three representative galaxies in our sample (the slow-rotator NGC 4244, the fast-rotator NGC 4565, and the disturbed NGC 1055). The top panel for each galaxy shows the original  $K_s$ -band mosaic, the middle panel shows the rebinned image chosen by the Voronoi binning algorithm and the same look-up table and stretch, and the bottom panel shows the bins color-coded by internal bin ID number to show the borders of the bins more clearly. In regions with very low  $S/N$  we truncate the binning process, and assume zero attenuation for our analysis. The grayscale stretch limits are 16.6–20.9, 15.4–21.4, and 15.4–21.2 mag arcsec $^{-2}$  for NGC 4244, NGC 4565, and NGC 1055, respectively.

files we bin our data to ensure high  $S/N$  over our entire region of interest. As discussed in Section 2.4, the practical limit for accurate surface-photometry is governed by small residual gradients in our images which persist even after attempting to minimize them in our sky subtraction. Table 1 indicates that these gradients are generally faint enough to pose little problem for our analysis.

### 3. ATTENUATION CORRECTION

#### 3.1. *Slow Rotators*

We expect that the dust properties of fast-rotating galaxies will be relatively similar to NGC 891 in their basic composition and geometry (e.g., clumping fractions, dust density thresholds for embedding young stars, scale-heights), although there will be differences in the details. For example, NGC 891’s extended dust tendrils at large scale-heights may be unusual. Nonetheless, our attenuation correction strategy is based on correlating the effective attenuation with changes of near-to-mid-infrared colors that we find in our models, and applying this *correlation* to the observations. Insofar as the correlation is relatively immune to details of the models, so too are our

estimated effective attenuations.

For the two slow-rotating galaxies in our sample, however, it is not clear that the assumed dust properties are even close to a good representation, given the different dust morphologies and metallicities of these systems compared to fast-rotators like NGC 891 and the MW (Dalcanton et al. 2004). Consequently, we re-did the attenuation correction modeling from Paper 1 for NGC 4244 (the better-studied of the two slow-rotators in our sample) to test the sensitivity of method to the details of the dust properties and geometry. A description of the procedure can be found in Paper 1, with the application and results for NGC 4244 presented in the Appendix A here. The salient feature of the modeling is that it must reproduce both the attenuated star-light and the re-radiated thermal and molecular dust emission.

We find that a slightly different attenuation correction is necessary for slow-rotators. However, as will be shown in Section 3.3, both slow-rotators appear to have very little  $K_s$ -band attenuation. As a result, the exact form of the slow-rotator attenuation correction is largely unimportant for our results in these galaxies. Moreover,

TABLE 2  
VORONOI BINNING REGIONS

Galaxy	Region Shape (kpc)
NGC 522	15x1.6
NGC 891	11x1.5
NGC 1055	9.8x2.1
NGC 4013	9.8x1.5
NGC 4144	1.5x0.54
NGC 4244	2.4x0.44
NGC 4565	15x1.5

<sup>a</sup> Regions are roughly elliptical, and are given as  $a \times b$ , where  $a$  and  $b$  are the semi-major and semi-minor axes.

given the very large difference in dust parameters and the rather modest change in the attenuation correction compared to the model for NGC 891, this supports our claim that our attenuation method, once properly calibrated by a realistic model, is relatively insensitive to the detailed dust prescription even for the fast rotating systems in our study.

### 3.2. Voronoi Binning

As in Paper 1, we focus our analysis on the  $K_s$ -band data as it is least likely to be affected by errors in the attenuation correction. Unlike NGC 891, however, many of these galaxies are at lower surface brightness, and as a result low S/N became an issue in computing the attenuation corrections at large radii. This is especially true for NGCs 4144 and 4244, the slow rotators, as well as NGC 1055, which as a disturbed galaxy at  $i \sim 85^\circ$  has large regions of stellar emission at low surface brightness.

As a result, we are forced to bin our data to ensure that our attenuation correction is not dominated by pixel-to-pixel variations in regions of low surface brightness. Since it is critical to maintain our excellent WHIRC resolution near the midplane (where S/N is high), we employ Voronoi binning to adaptively bin our data before computing an attenuation correction. Our algorithm, written in Python, is based on the procedure outlined by Cappellari & Copin (2003), but with significant numerical optimizations in order to run efficiently on images with  $>1$  million pixels. The most critical of these optimizations are the use of balltrees, which allow for the fast computation of nearest neighbors by partitioning the data into a binary tree (Omohundro 1989), and the use of fast native Numpy array operations wherever possible. Additionally, we choose a maximum height (by visual inspection), above which the attenuation is assumed to be zero. This keeps us from correcting low-SB data which we suspect to be uncontaminated by dust, and also serves to speed up the computation. While there are likely small amounts of high-latitude attenuation at UV/optical wavelengths in some of these galaxies (e.g. NGC 891; Howk & Savage 1997; Seon et al. 2014), the average attenuation at large heights in the NIR is likely minimal. To fully realize performance gains we are forced to relax the bin circularity and adjacency criteria of Cappellari & Copin (2003), but due to the relative smoothness of the underlying surface brightness distribution at low S/N we find no evidence of any issues arising as a result of these decisions. We set our binning threshold at  $S/N = 20$ , which we find empirically produces a

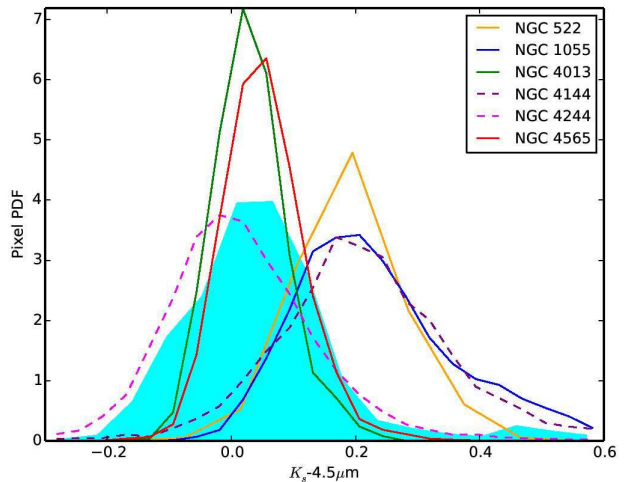


FIG. 3.— Probability distribution function (normalized so the integrated y-value = 1) of  $K_s-4.5\mu\text{m}$  colors for Voronoi-binned pixels in unattenuated regions of the galaxies in our sample, color-coded by galaxy. For fast rotators (solid lines) we only use bins with  $|z| \geq 1\text{kpc}$ , while due to their transparency we place no height restriction on the slow rotators (dashed lines). NGC 891, the galaxy on which we based our attenuation correction in Paper 1, is shown as the filled cyan curve.

smoothly varying attenuation map while preserving as much spatial structure as possible. The source code for the Voronoi binning script is available for general use on Github<sup>5</sup>.

After compiling the initial bins, we perform 20 iterations of the Centroidal Voronoi Tessellation algorithm (Du et al. 1999). As a final step, we reject very large bins, which we find tend to probe background fluctuations rather than real features in the galaxy. An example of the binning process is shown in Figure 2. With this method the excellent WHIRC resolution is maintained in the dusty midplane regions, while larger bins at large heights allow for a robust attenuation correction even in areas where the S/N per pixel is low. In regions with very low S/N (S/N per pixel  $\lesssim 0.6$ ) we truncate the binning process and treat those pixels as having zero attenuation. This assumption is well-justified by a visual inspection of the optical and NIR images, which show no indication of dust in these regions. Estimates of the physical size of the binned regions are shown in Table 2.

### 3.3. Improved Attenuation Correction Methodology

Although our attenuation correction method was quite effective for NGC 891, attempting to apply it in this work led to significant problems due to variations in the unattenuated near- and mid-IR colors of galaxies' stellar populations. The attenuation correction from Paper 1 assumed an underlying color of  $K_s-4.5\mu\text{m} \sim 0$ , which is plausible for a spectral energy distribution dominated by the Rayleigh-Jeans tail from stellar photospheric emission. As shown in Figure 3, however, there is a variation of  $\sim 0.3$  mag in mean color between and *within* galaxies in our sample. This variation is significantly larger than the photometric errors for our Voronoi-binned data; with a bin  $S/N \approx 20$ , the color errors are only  $\sim 0.07$  mag, a fac-

<sup>5</sup> <https://github.com/AndrewRook/astro/tree/master/voronoi>

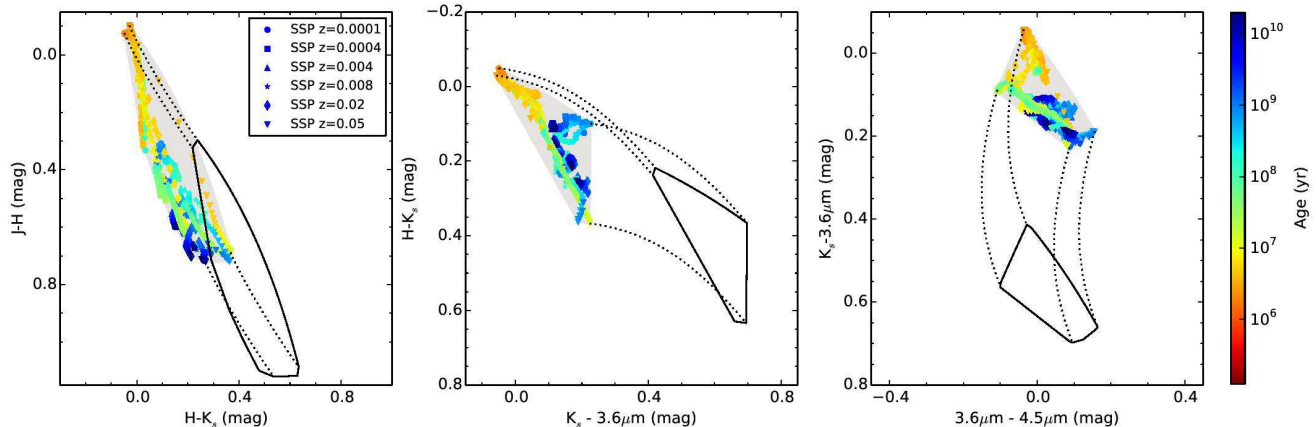


FIG. 4.— IR color dependence on age and metallicity for SSP models from Bruzual & Charlot (2003). The different symbols denote the metallicity of the SSPs, with 0.02 being solar. Colors indicate the age of the SSPs. The gray shaded region shows the color space accessible by linear combinations of SSPs, while the dotted black lines and solid black shape show that color space for  $A_{K_s}^e = 0.5$  mag. The attenuation correction results in a slight shift blueward in the  $3.6\mu\text{m}-4.5\mu\text{m}$  colors at small attenuations due to contributions from PAH emission.

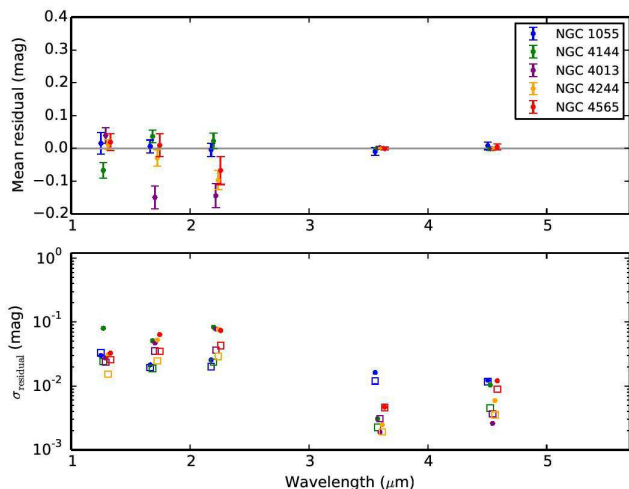


FIG. 5.— Residuals from fitting SSPs to the multi-band near- and mid-infrared fluxes of individual sightlines for several galaxies in our sample in regions expected to have low attenuation. Top panel: mean residual (weighted by the errors on the data) are plotted as a function of wavelength (from left to right,  $J$ ,  $H$ ,  $K_s$ , IRAC  $3.6\mu\text{m}$ , and IRAC  $4.5\mu\text{m}$ ). Errors indicate the weighted standard deviation about the mean residual. Bottom panel: weighted standard deviations (filled circles) are compared to the average uncertainty in the data (open squares). Points at each wavelength have been scattered slightly around the central wavelength of each filter to improve readability.

tor of over four times smaller than the observed range of  $K_s-4.5\mu\text{m}$ . There is no correlation between  $K_s-4.5\mu\text{m}$  color and rotation speed in this sample. The apparent bimodality in the intrinsic color distribution between galaxies see in Figure 3 may simply be an artifact of the small sample size, but this feature merits further exploration with larger samples.

Even though NGC 891 does have a mean  $K_s-4.5\mu\text{m} \approx 0$  in unattenuated regions, there appears to be some internal spread in this color. In general for this and the other galaxies in our sample, the assumption of zero color in our previous attenuation correction scheme leads to over or underpredictions of the actual attenuation when applied to galaxies with different colors. How-

ever, due to our RT modeling method, the *slope* of our derived attenuation correction is independent of the intrinsic (unattenuated) colors of the stellar population. That is, the inferred effective attenuation can still be determined by a *change* in, e.g.,  $K_s-4.5\mu\text{m}$  color relative to the unattenuated color. Henceforth we formulate our attenuation formulae in terms of the color excess  $E(K_s - 4.5\mu\text{m}) \equiv (K_s - 4.5\mu\text{m}) - (K_s - 4.5\mu\text{m})_0$ , where  $(K_s - 4.5\mu\text{m})_0$  is the unattenuated color, as we have done in the Appendix here. The task at hand is to determine better estimates for  $(K_s - 4.5\mu\text{m})_0$ .

It is tempting to account for the intrinsic variation of near- to mid-IR colors by setting  $(K_s - 4.5\mu\text{m})_0$  to the colors of the galaxy at a point well above the midplane that is presumed to be dust-free. However, given that we know the  $K_s-4.5\mu\text{m}$  color varies between galaxies, the assumption that it should be constant *within* a single galaxy is also significantly weakened, *especially given the fact that we are specifically seeking evidence for different stellar disk components*.

An inspection of model simple stellar populations (SSPs) from (Bruzual & Charlot 2003) indicates that there is a significant range of allowed IR colors (a spread of  $\sim 0.2$  mag in the  $K_s$ -IRAC colors), that depends both on the age of a population as well as its metallicity (Figure 4). This is simply a reflection of departures from pure black-body emission due to absorption features (mostly molecular) that arise in cool stars; the impact of these features on the integrated light at these wavelengths depends on both age and metallicity of the stellar population. However, the reddening vectors in Figure 4 indicate that we may be able to disentangle some of these effects from the attenuation by using our full suite of WHIRC+IRAC colors.

We undertook a brute-force modeling approach, fitting the five observed broad-band magnitudes ( $J$ ,  $H$ ,  $K_s$ ,  $3.6\mu\text{m}$ , and  $4.5\mu\text{m}$ ) for each Voronoi-binned pixel in each galaxy independently to SSPs over a wide range of ages and metallicities.<sup>6</sup> Our decision to use only

<sup>6</sup> Each SSP was convolved with the WHIRC and IRAC filter curves and magnitudes were generated taking into account the IRAC aperture corrections necessary to per-

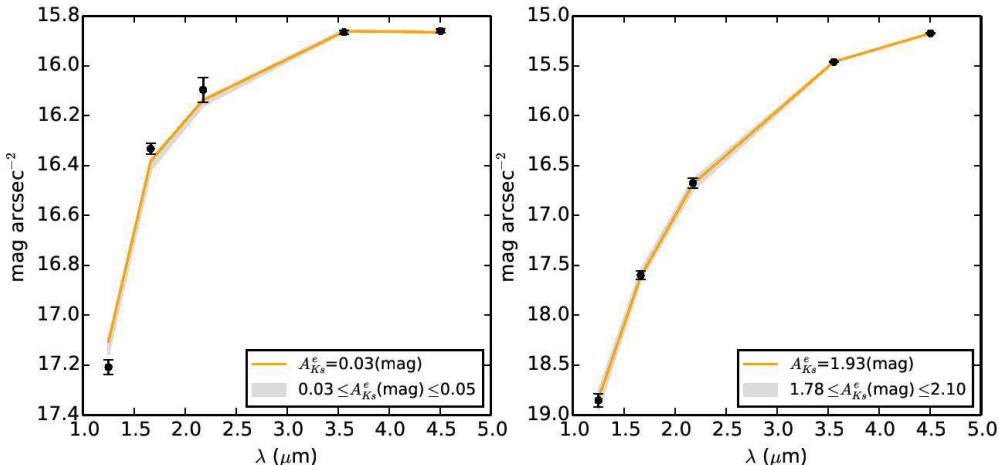


FIG. 6.— Demonstration of the attenuation correction method on individual binned pixels of NGC 891. Left panel: a low attenuation region at  $R \sim 2\text{kpc}$ ,  $z \sim 0.5\text{kpc}$ , with a bin size of  $0.25\text{ arcsec}^2$ . Right panel: a high attenuation region at  $R \sim 2\text{kpc}$ ,  $z \sim 0\text{kpc}$ , with a bin size of  $0.1\text{ arcsec}^2$ . Black points show the data, the orange line indicates the best fit, while the gray shaded region indicates the fits within our 67% confidence limits. The legend gives the best fitting attenuation, as well as the full range of  $A_{K_s}^e$  allowed by the models within the confidence limits.

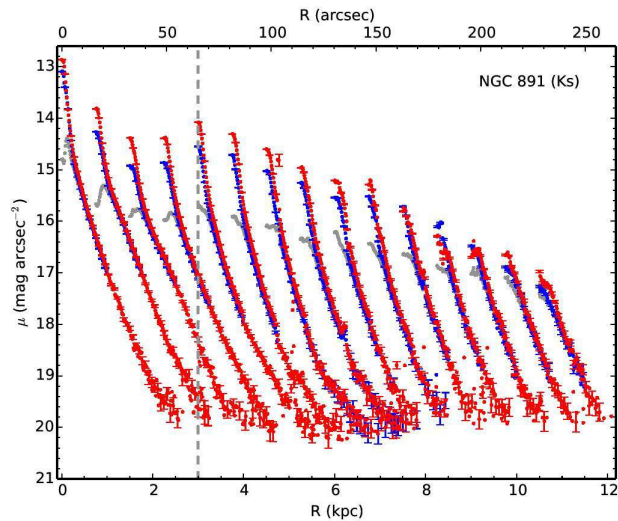


FIG. 7.— Comparison between the attenuation correction used in this work with that used on NGC 891 in Paper 1. Gray points show the uncorrected surface-brightness profiles, while the red and blue points denote profiles corrected with the Paper 1 method and the method from this work (respectively).

NIR and MIR but not optical bands was based on the desire to balance leverage on reddening with sensitivity to changes in the underlying population (e.g., age), while keeping the optical depth in different bands comparable and modest. For every model, the attenuation was tuned to optimize the fit (in a  $\chi^2$  sense) for a particular binned pixel:

$$\chi^2 = \sum_{i=J,H,K_s,3.6,4.5} \frac{(f_{d,i} - \xi f_{m,i})^2}{\delta f_{d,i}^2}, \quad (1)$$

where  $f_d$  and  $f_m$  are the fluxes from the binned data pixel and the model, respectively,  $\xi$  is a constant offset

from extended-source photometry, which the IRAF Handbook (<http://irsa.ipac.caltech.edu/data/SPITZER/docs/irac/irac-instrumenthandbook/>) gives as 0.10 and 0.07 mag for 3.6 and  $4.5\mu\text{m}$ , respectively.

set to minimize  $\chi^2$ , and  $\delta f_d$  is the error on the binned data pixel. Attenuated magnitudes were computed using the same differential attenuation-color relationship found in Paper 1 or Appendix A, using the  $E(K_s - 4.5\mu\text{m})$  formulation. The distribution of attenuation and  $\chi^2$  from all of the models was saved for every binned pixel.

As is well known, there is a significant degree of degeneracy in the range of models with different age or metallicity that yield comparably good fits to the data. However, there are always *some* single SSPs that are able to fit every binned pixel well. As shown in Figure 5, the standard deviation between best-fitting model and data, averaged over many binned pixels, is comparable to the measured errors, indicating that a more complex model would not result in an improvement in the overall goodness-of-fit. It was for these reasons that we did not consider a broader suite of models including varying star-formation histories. No doubt it is possible to reduce the number of models to a smaller number of principal components or eigenspectra, e.g., Bershady (1995) or Connolly et al. (1995), but this is a further refinement which essentially only improves computational performance.

This model degeneracy is not a concern for our analysis here so long as there is little covariance between different combinations of intrinsic model colors and inferred attenuation for the set of models that fit the data well. To account for this covariance, we compute the uncertainty in the attenuation correction to be the full range of attenuations found for all models with  $\chi^2$  values within a 67% confidence limit relative to the best-fitting model. We find that these uncertainties are generally small ( $\lesssim \pm 10\%$  of  $A_{K_s}^e$ ), and we treat this as a source of random error. We also consider the impact of distance-dependent resolution effects in the following section (see Figure 8), but we do not account for these effects in our calculation. Example fits from low and high attenuation regions of NGC 891 are shown in Figure 6 to illustrate the fidelity of our methodology. We compare the results of the new attenuation correction against the one used in Paper 1 in Figure 7. The most dramatic changes are



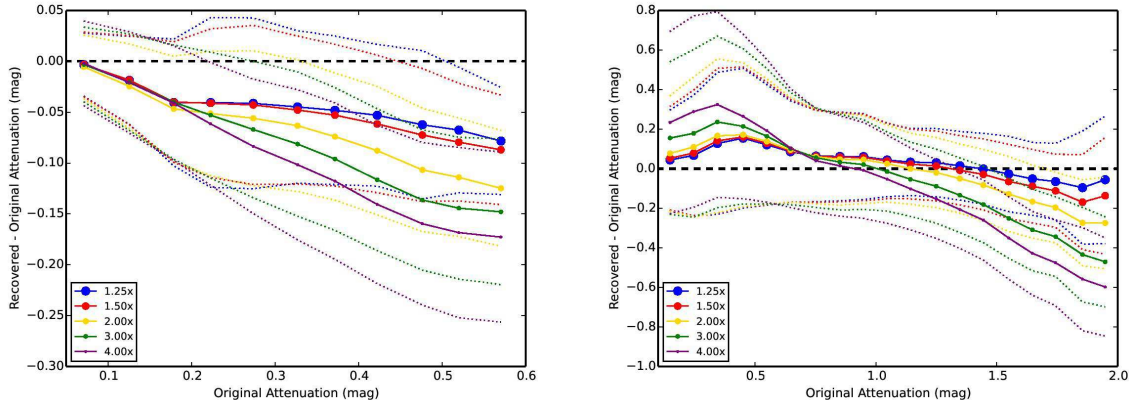


FIG. 8.— Effect of increasing galaxy distance on our attenuation correction, for NGC 4565 (left panel) and NGC 891 (right panel). Each point shows the residual between the recovered attenuation (averaged over individual pixels) at a given distance and the actual attenuation. Dotted lines show the standard deviation about the mean. Points are color coded by distance (shown as a multiplier on the actual distance to the galaxies, which is 11.7 and 9.5 Mpc for NGC 4565 and NGC 891, respectively). The dashed black line shows zero residual as reference, i.e., the ideal case where going out to larger distance has no bias on the attenuation measurement.

near the mid-plane in the sense that our attenuation corrections here are *smaller* than in our previous work. The impact of this change on our model fitting is discussed in §5.1.1.

Images showing the resulting attenuation maps, corrected data, and vertical attenuation profiles for our sample are shown in Figures 9 to 15, in order of the discussion of the surface brightness analysis in Section 5. This ordering roughly corresponds to the complexity of the modeling analysis (high to low), which interestingly corresponds closely to decreasing  $V_{\text{rot}}$ . Given the significant changes made to our attenuation correction technique, we re-analyzed our NGC 891 data from Paper 1; the NGC 891 attenuation corrections in Figure 9 (and the other figures in this work) show results using these new corrections.

### 3.3.1. NGC 522: Distance-Dependence of our Attenuation Correction

Despite the evidence for dust attenuation in NGC 522 (visible in the both the optical and NIR images in Figure 1) our correction method (Figure 12) finds very little attenuation in any part of the galaxy. This model-based conclusion is surprising, given the fact that this galaxy is a fast-rotator and should therefore have a dense dust lane. However, NGC 522 is  $\sim 2$  times more distant than any other galaxy in our sample, so we must investigate the possibility that this galaxy is beyond the range where our attenuation correction procedure is able to resolve dust structure in super-thin layers with the data we have in hand. If the spatial resolution of the IRAC is too low to resolve the dust features in this galaxy, regions of high attenuation are suppressed by mixing them with neighboring regions at lower attenuation. The poor resolution at  $4.5\mu\text{m}$  is readily apparent in Figure 12.

In general, we do not expect to be able to resolve dust structure on all physical scales, which makes investigating this potential issue difficult. Creating a galaxy model with high enough spatial resolution to perform a fully controlled test of this possibility is currently computationally infeasible (for an example of the state-of-the-art in this sort of modeling see Schechtman-Rook et al. 2012). What is relevant for this study, however, is that

we are able to resolve the physical scales necessary for the bulk characterization of disk structure. Based on what we know about the Milky Way and NGC 891, the smallest scale of interest in the edge-on perspective is the super-thin disk component with an expected scale-height of 50-100 pc. Therefore a suitable approximation for probing distance systematics is to rescale our data for NGC 891 and 4565, our two most nearby fast-rotators (both with resolution comparable to or better than 50 pc at their assumed distances), to simulate their appearance at larger distances. In this way we can test whether we can resolve comparable attenuation distributions over the full distance range of galaxies in our sample.

To simulate the appearance of NGC 891 and 4565 at larger distances, we convolve them with a suitable gaussian kernel for each distance, assuming the same seeing conditions. We then rebin the data to preserve the proper pixel scale. We compute the attenuation in each smoothed and rescaled pixel, and compare it to the attenuation estimated for the matching pixels in the original galaxy images, as shown in Figure 8. Since this Figure shows averages and standard deviations binned by values of the original attenuation value, each distance-shifted pixel is counted multiple times for the corresponding set of pixels matched to the original image.

As we expect, we find that increasing distance acts to flatten the attenuation distribution: Pixels with larger attenuations are suppressed while pixels with small attenuations are enhanced. This is simply a smoothing effect, the details of which depend on the intrinsic distribution of regions with different levels of attenuation. In edge-on disks (e.g., NGC 891), the regions of highest attenuation are very thin, linear structures, and are spatially promimate to more extended regions of lower attenuation (at larger scale height). As disk projection moves away from purely edge on (e.g., NGC 4565), the attenuation peak diminishes and the overall distribution of attenuation is spatially broader; these attributes tend to diminish the impact of spatial resolution on distance. This qualitative description matches the observed behavior in Figure 8. Overall, the result of moving either NGC 891 or NGC 4565 out to a distance comparable to NGC 522 (roughly four times as distant, corresponding

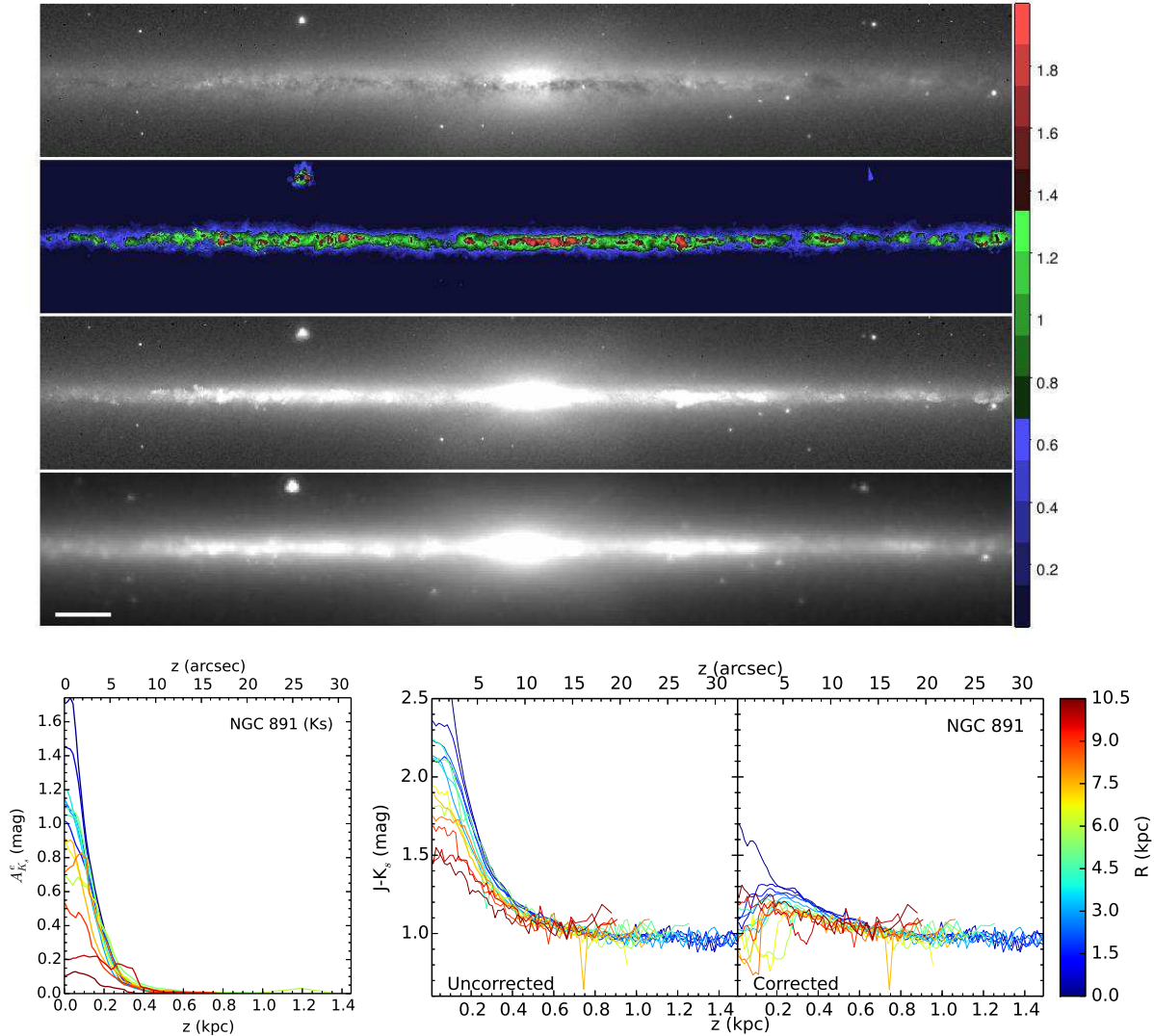


FIG. 9.— Images and vertical profiles illustrating attenuation effects and corrections for NGC 891. Images, top to bottom: central region of the  $K_s$ -band image (with a grayscale stretch from 14.7–21.2 mag arcsec $^{-2}$ );  $K_s$ -band attenuation map, in magnitude units; attenuation-corrected  $K_s$ -band image, with the same gray-scale as the top panel; IRAC  $4.5\mu$  image, for comparison. The white bar shows 1 kpc at the assumed distance to NGC 891. Bottom plots, left to right: vertical attenuation profiles; observed vertical  $J-K_s$  profiles; and attenuation-corrected vertical  $J-K_s$  profiles. The color of each line shows the radius of that profile. The profiles are adaptively binned in the  $z$  direction to maintain an error of  $\leq 0.05$  mag, out to the limiting surface brightness of our data. The  $z$  coordinate used here is the projected height, but this galaxy is estimated to be nearly perfectly edge on.

to the smallest points in Figure 8) is to bias estimates of the peak attenuation downward by  $\sim 15$ –60% (depending on whether one uses the peak attenuation difference in NGC 4565 or NGC 891, respectively).

Even after taking this correction into account, however, the peak attenuation in NGC 522 would still be  $\lesssim 0.1$  mag. There are some indications that NGC 522 is not exactly edge-on (most notably the fact that the light from the central region of this galaxy is not symmetrical above and below the dust lane in Figure 1), and may be more similar in gross morphology to NGC 4565. For NGC 4565, this lower inclination acts to suppress the peak attenuation since the super-thin mid-plane dust is projected over a substantially thicker line of sight. However, even NGC 4565 has attenuation  $\gtrsim 0.2$  mag. Applying a distance correction based on the NGC 4565 simulation in Figure 8 to NGC 522 does not bring its attenuation level on par.

The lower dust attenuation for NGC 522 relative to NGC 4565 may be due to the nearly  $100 \text{ km sec}^{-1}$  difference in  $V_{\text{rot}}$  between these two galaxies, perhaps indicating that while NGC 522 has sufficient mass to produce a dust lane (Dalcanton et al. 2004) it is not capable of compressing it to the level needed to produce significant  $K_s$ -band attenuation at its inclination. This explanation is conjecture, and requires higher resolution imaging data to confirm. We opt not to make any distance correction to NGC 522 in this work, due to the large uncertainty on such a correction (a result of both the intrinsic scatter and the large difference in the magnitude of the correction between NGCs 891 and 4565). Therefore we caution the reader to be aware of these issues when examining our results for this system.

Finally, while we were primarily interested in interpreting the unusual attenuation correction results for NGC 522, understanding how our attenuation estimates

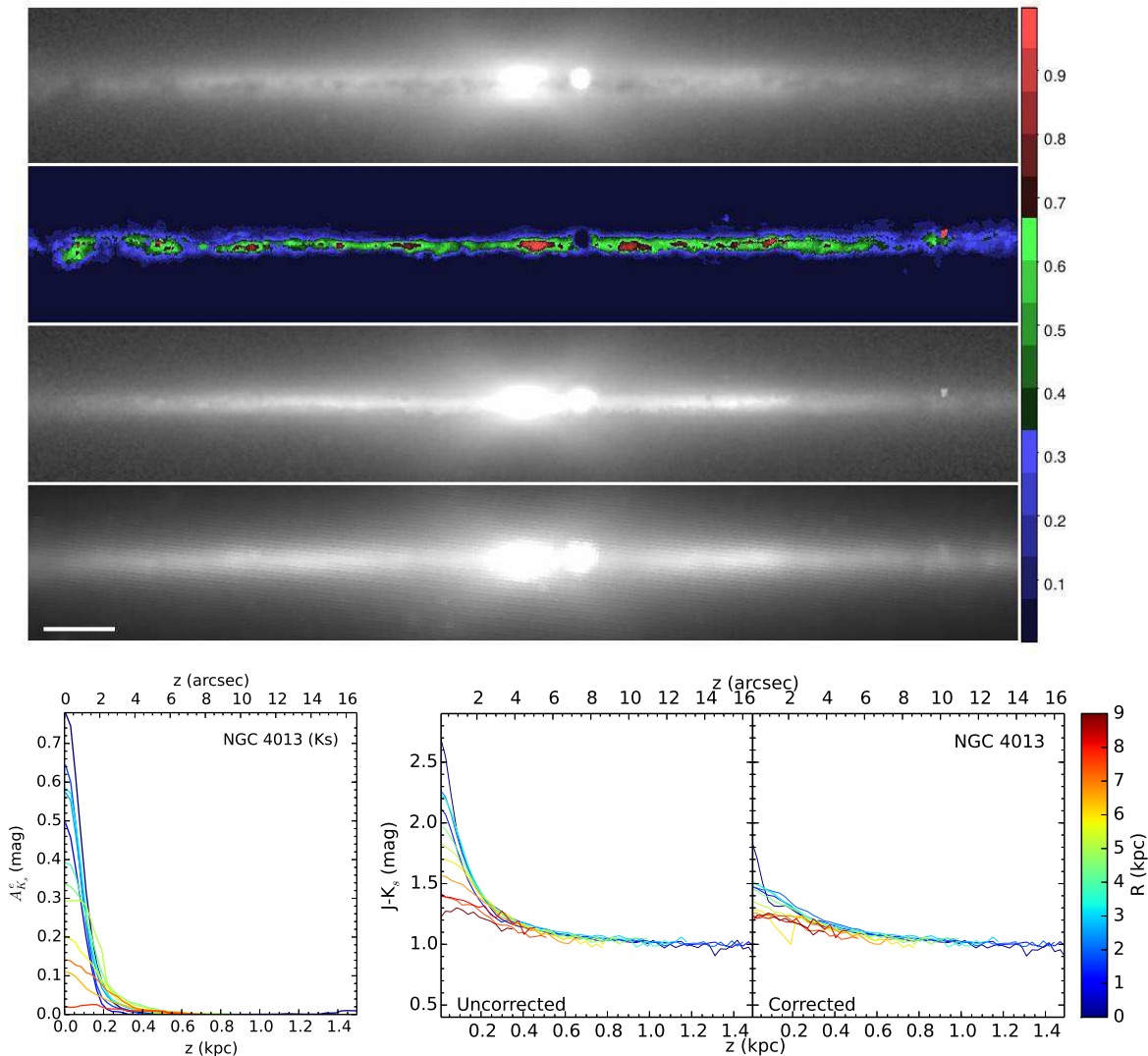


FIG. 10.— Same as Figure 9, but for NGC 4013 (the  $K_s$ -band images grayscale range is from 15.0-21.2 mag arcsec $^{-2}$ ). Note the bright star just to the right of the center of the galaxy is masked out from all of our data after this step and so does not appear in any of our attenuation, color, or surface brightness profiles, nor does it affect our model fits. The  $z$  coordinate used here is the *projected* height, but this galaxy is estimated to be nearly perfectly edge on.

depend on distance is important for the other fast-rotating galaxies in our sample. NGCs 1055 and 4013 are  $\sim$ twice as distant as NGCs 891 and 4565, and Figure 8 shows that we are likely underpredicting the actual peak attenuation by  $\sim$ 10-20%. This will primarily affect our measurements of very thin components, as the largest attenuations are almost always found near the midplanes of spiral galaxies, and would result in an *underestimate* of the central surface brightness and an *overestimate* of the scale-heights of such components, points which we return to below. The total light, however, will be properly estimated. In future analysis, we suggest a forward modeling approach might better account for the impact of spatial resolution on the inferred attenuation and unattenuated light profiles in a self-consistent manner; such an investigation is beyond the scope of this work.

#### 4. GALAXY COLORS

We show the vertical  $J - K_s$  color profiles for the galaxies in our sample in the bottom middle and right panels of Figures 9-15. These figures include both the appar-

ent and attenuation-corrected profiles. Several interesting features relevant to an assessment of our attenuation corrections, the distribution of dust, and gradients in stellar populations in these galaxies are apparent in these color profiles. The dust distribution and population gradients are interesting in their own right as well as pertinent to the following analysis of the photometric decomposition of these edge-on spiral galaxies into multiple components.

As a starting point for this discussion, we show the color excess  $E(J - K_s)$  as a function of attenuation in Figure 16 based on our RT modeling in Paper 1 for fast rotators and in the Appendix here for slow rotators. For  $A_{K_s}^e < 0.5$  mag the relation between color excess and attenuation is nearly linear with  $E(J - K_s)/A_{K_s}^e \sim 1.2$ . We also plot the  $J - K_s$  colors versus age and metallicity in Figure 17 for the same models used in Figure 4 as well as models using a different prescription for the late phases of intermediate-age stars from Maraston (2005). From this it can be seen that simple stellar populations

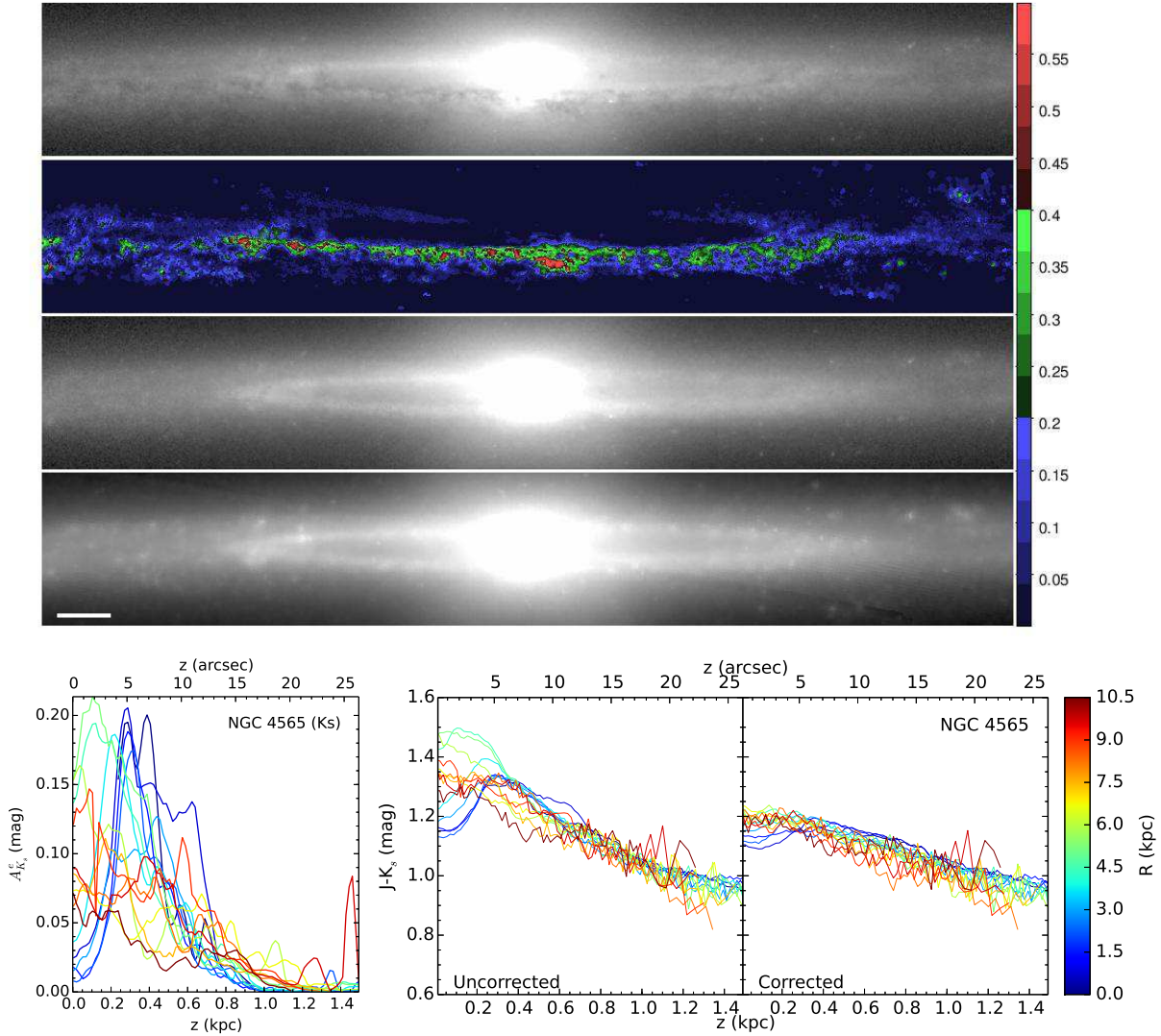


FIG. 11.— Same as Figure 9, but for NGC 4565 (the  $K_s$ -band images grayscale range is from 15.4–21.4 mag arcsec $^{-2}$ ). The  $z$  coordinate used here is the *projected* height; this galaxy is estimated to be inclined at 87.6 deg (see 5.2.3).

predicted from stellar population synthesis models are no redder than  $J - K_s \sim 1.2$ , corresponding to the stellar colors of M4–5 III giants<sup>7</sup>.

Based on dynamical argument, at large distances from the disk mid-plane we expect the stars to be primarily from old populations. For stellar populations older than  $\sim 1$  Gyr, different models yield comparable predictions for  $0.6 < J - K_s < 1.0$ , varying weakly with age and primarily with metallicity from about 1/20th to  $\sim 3$  times

<sup>7</sup> We refer to Bessell & Brett (1988), Tokunaga (2000), and Rayner et al. (2009) for our estimates of the NIR colors of stars. We also note that we loosely refer to  $J - K_s$  colors on the 2MASS photometric system (Carpenter 2001) for all studies discussed here, even though many of these studies predated 2MASS and therefore adopted slightly different systems. In the color range of our observations Frogel et al. (1978), Persson et al. (1983), Frogel & Whitford (1987), and Terndrup et al. (1994) calibrated to the CIT. Maraston (2005) adopted the Cousins-SAAO system. In the relevant color range their  $J - K$  colors are, respectively,  $\sim 0.04$  redder and  $\sim 0.07$  bluer than  $J - K_s$ . The Bruzual & Charlot (2003) colors were calculated by us directly from the spectra based on the correct filter transmission curves to place them in the 2MASS system.

solar. This variation reflects the position of the red giant branch which varies (in a luminosity-weighted sense) between effective spectral type K0 to M0. The colors of massive galaxies with little dust and old stellar populations, such as E/S0s (e.g., Frogel et al. 1978), are in good agreement with these models, having  $0.8 < J - K_s < 1.0$ . This, of course, is for integrated light. In the bulge of the Milky Way, however, Frogel & Whitford (1987) found a distribution of variable and non-variable giants up to  $J - K_s \lesssim 1.4$  in Baade’s window, with the integrated M-giant light dominated by spectral type M6, or  $J - K_s \sim 1.2$ . In the context of recent analysis of VVV and 2MASS data for the bulge by Gonzalez et al. (2013), who also find such red giant colors, this is an extension of the metallicity effect on the giant branch. We might expect, therefore, that in specific locations of galaxies that are super metal rich that the  $1 < J - K_s < 1.2$  would occur even for older stellar populations.

The situation closer to the disk mid-plane is potentially more complicated in the sense that a wider range of stellar population ages likely co-exist, depending sen-

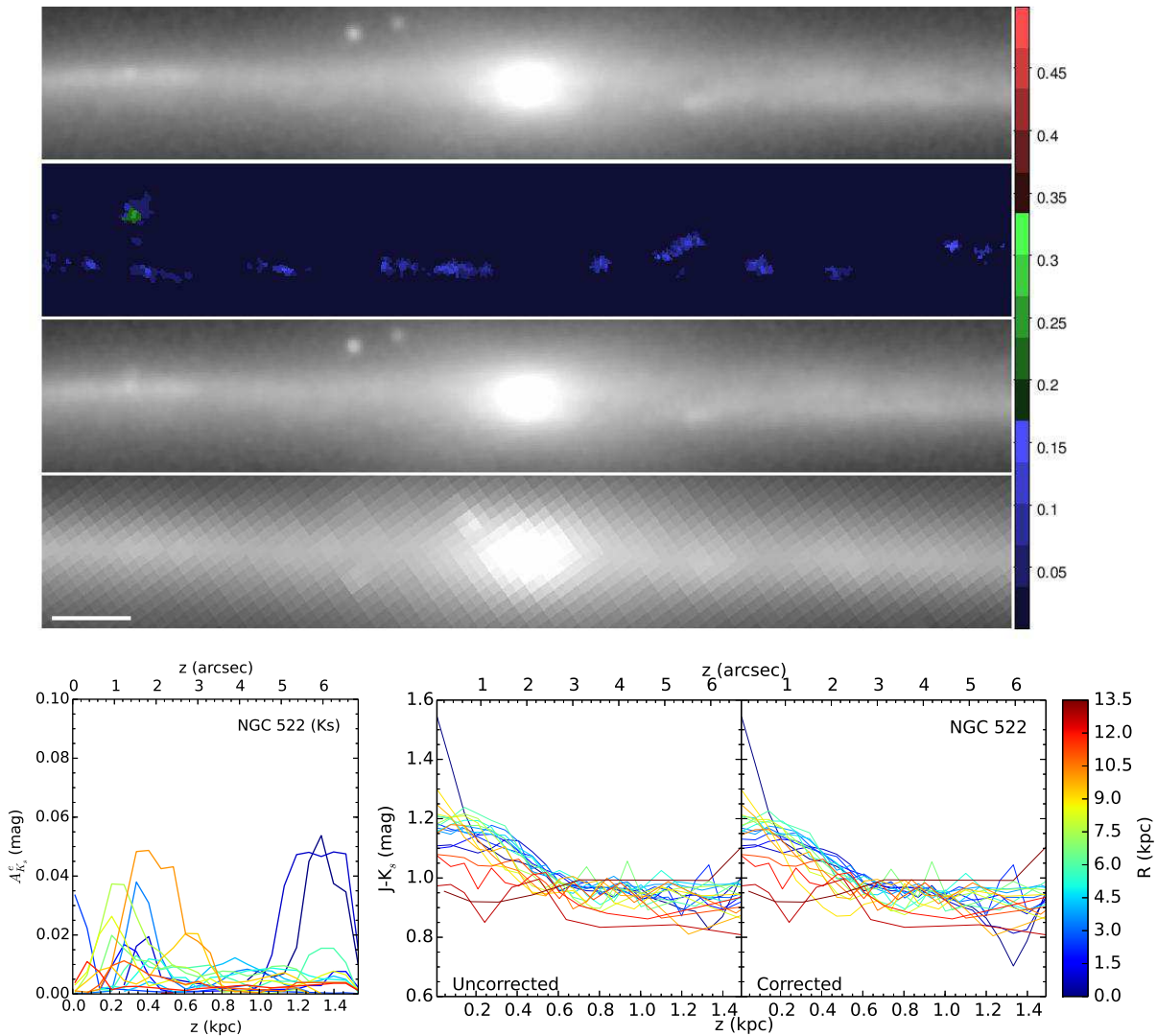


FIG. 12.— Same as Figure 9, but for NGC 522 (the  $K_s$ -band images grayscale range is from 15.4–21.2 mag arcsec $^{-2}$ ). The  $z$  coordinate used here is the *projected* height; this galaxy is estimated to be inclined at 88.5 deg (see 5.2.4).

sitively on the recent star-formation history and the dynamical heating of the disk. In the age range from 0.2 to 2 Gyr the models in Figure 17 are discrepant due primarily to the treatment of AGB stars. The seminal study by Persson et al. (1983) of the near-infrared properties of LMC and SMC star clusters show some have very red  $J - K_s$  colors, even after correcting for reddening. At intermediate ages there is a continuous distribution of colors extending up to  $J - K_s = 1.4$ , with an outlier (NGC 2209) at  $J - K_s = 1.7$ . Given the strength of the  $2.3\mu\text{m}$  CO feature in these red clusters, they conclude the colors are due to the presence of carbon AGBs. Both the integrated colors and the presence of carbon stars have been confirmed by more modern measurements (Mucciarelli et al. 2006). While using these results to constrain the plausible range of near-infrared colors for more massive, star-forming galaxies with possibly a wider range of metallicities and ages is somewhat uncertain, it does inform us as to what colors are plausible.

From these considerations, and accounting for an un-

certainty of  $\pm 0.1$  mag in our attenuation correction, we consider any  $J - K_s > 1.3$  is likely to arise from reddening or unusual stellar populations.

#### 4.1. Apparent Colors

All of the galaxies in our sample become redder in *apparent*  $J - K_s$  color near the mid-plane and at smaller radius, with NGC 4565 being one exception. These reddening trends are likely a confluence of dust attenuation *and* population gradients in radius and height above the disk.

For NGC 4565, while generally following the trend in apparent  $J - K_s$  color, there is significant drop in  $J - K_s$  color near the mid-plane at small radii. This feature corresponds to the regions of the galaxy inside the evacuated inner parts of this galaxy’s disk (readily visible in Figure 1), and is a strong indicator that this region has minimal attenuation. If NGC 4565 is not aberrant in this regard and dust-free inner regions are common in massive spiral galaxies, it would imply that much of the obscuring dust in these galaxies is not smoothly distributed over all radii, but instead preferentially at larger radii. This

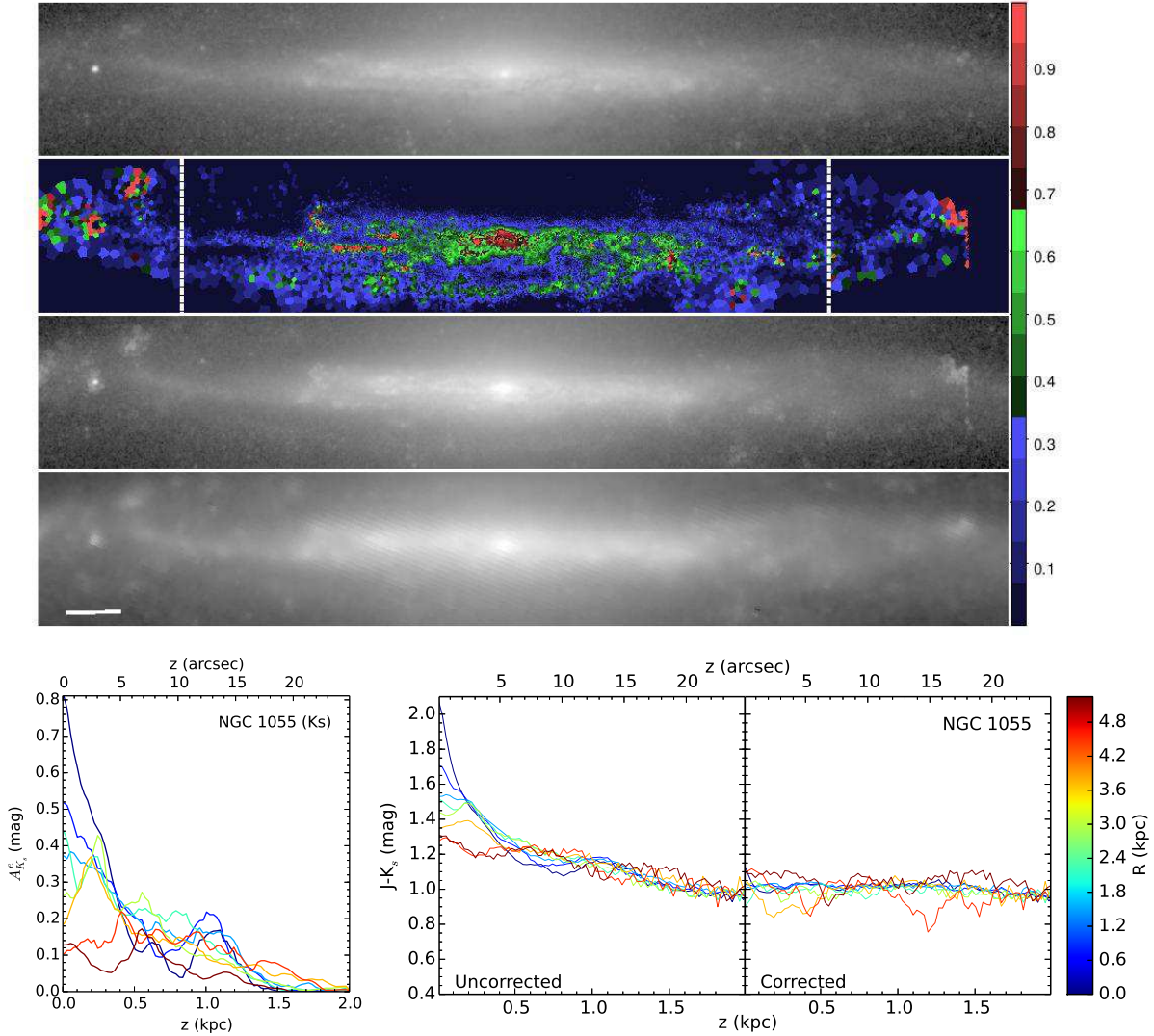


FIG. 13.— Same as Figure 9, but for NGC 1055 (the  $K_s$ -band images grayscale range is from 13.7-21.2 mag arcsec $^{-2}$ ). The vertical dashed lines in the top panel indicate the outer limit of our model fitting for this galaxy, which avoids regions of low S/N where flux from the galaxy’s spheroidal component begins to dominate over the disk. The  $z$  coordinate used here is the *projected* height; this galaxy is estimated to be inclined at 85.5 deg (see 5.2.5).

would explain, for example, the relative prominence of dust lanes in many highly-inclined spiral galaxies.

Only three galaxies have central apparent  $J - K_s$  colors significantly above 1.2 mag, namely NGCs 891, 4013, and 1055. All three are fast rotators. The apparent red colors of NGC 891 and 4013 are easily explained by their almost perfectly edge-on orientation. Given the amount of attenuation recovered by our correction (Figure 9), it is unsurprising to find that NGC 891 has significantly redder apparent  $J - K_s$  colors near the mid-plane than any of the other galaxies in our sample. Both NGCs 891 and 4013 have attenuation and  $J - K_s$  color profiles which become broader and shallower toward larger radii, possibly hinting at a thickening of the dust layer and a commensurate reduction in the mid-plane optical depth at larger radii. NGC 1055, however, is not exactly edge-on; its red colors likely are the result of the interaction that produced the other striking features of this galaxy (discussed in more detail in Section 5.2.5).

For the other fast-rotators, NGC 4565 has a peak color

of  $J - K_s \sim 1.4$  mag, because even though it probably contains a similar amount of dust as NGC 4013 it has  $i \sim 87^\circ$  (de Looze et al. 2012). NGC 522 also appears to have modest reddening near the mid-plane, consistent with the little attenuation found for this system. Both of these galaxies, and all of the fast rotators are distinguished from the two slow-rotating disk systems that have apparent  $J - K_s$  colors less than 1 mag. These blue  $J - K_s$  colors are consistent with the small amount of dust found in these systems, but also likely reflect differences in their stellar populations.

Most of the galaxies converge to a  $J - K_s$  color of  $\sim 0.9$ -1 mag at large heights where the dust attenuation is minimal. This is comparable to the color of a cool giant star in the spectral range of late K to early M—not unreasonable for what should be an old, metal-rich stellar population. The one exception is NGC 4144, which asymptotes to  $J - K_s \sim 0.65 \pm 0.1$ , similar to that of an early K giant. This is indicative of either an old, metal poor stellar population or a much younger system, the

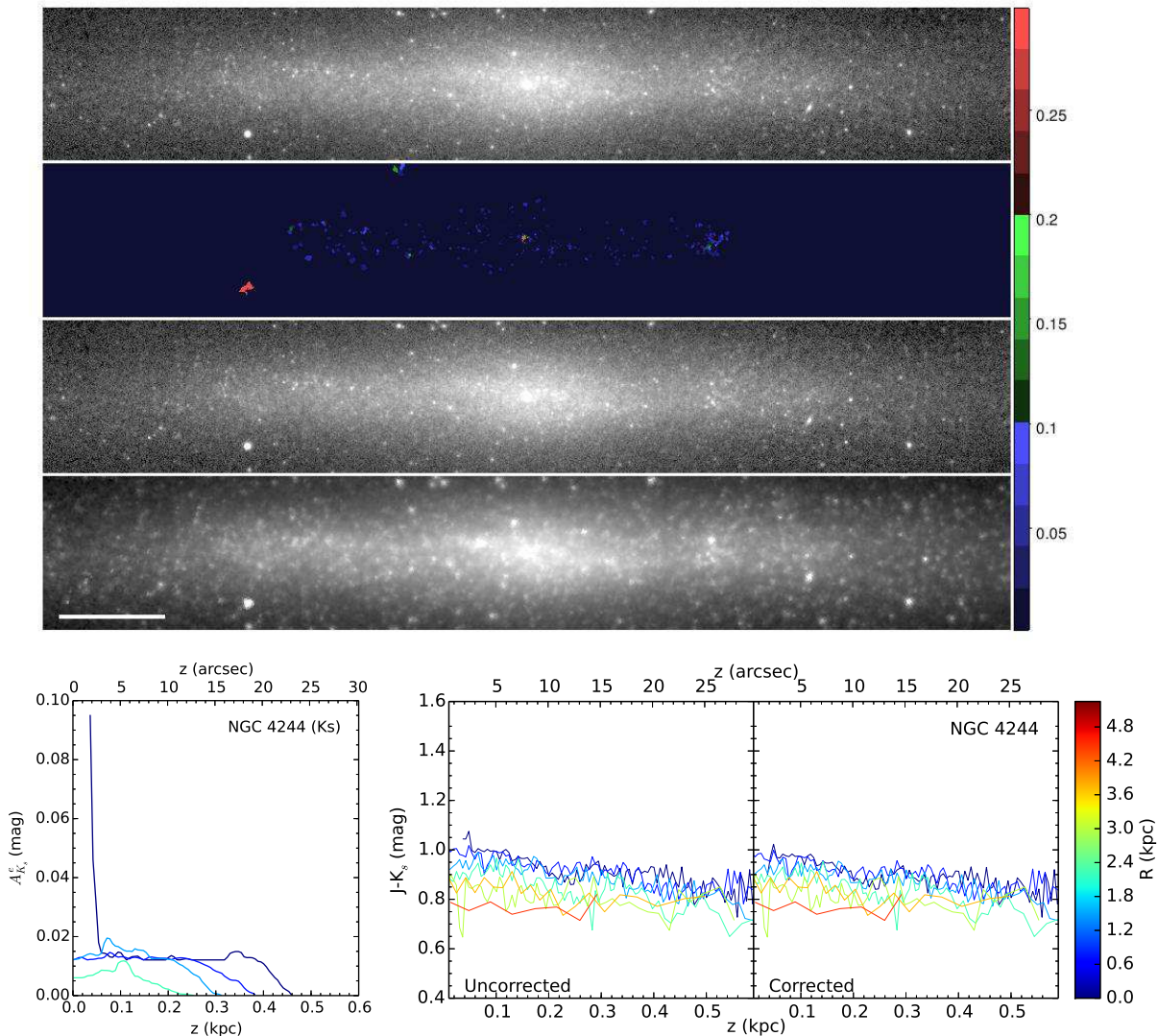


FIG. 14.— Same as Figure 9, but for NGC 4244 (the  $K_s$ -band images grayscale range is from 17.0–20.7 mag arcsec $^{-2}$ ). The  $z$  coordinate used here is the *projected* height; this galaxy is estimated to be inclined at 85.8 deg (see 5.2.6).

latter possibly the result of a recent global star-formation episode. NGC 4244, our other slow rotator, has somewhat redder  $J-K_s$  colors ( $0.85 \pm 0.1$ ), but is still slightly bluer than the fast rotators in our sample.

#### 4.2. Attenuation-Corrected Colors

Once the color profiles have been corrected for attenuation, the range of vertical and radial gradients in  $J-K_s$  diminish considerably, as expected. The two slow rotators NGC 4144 and 4244 exhibit shallow, nearly linear gradients in height of  $-0.2$  mag per kpc, independent of radius, i.e., the disks appear to get bluer with height above the mid-plane. These color profiles are largely unchanged by the attenuation corrections because the level of attenuation is small. With the exception of NGC 1055, all of the fast rotators show pronounced vertical gradients in  $J-K_s$ . NGC 1055’s lack of discernable color gradients in radius or height is likely associated with its morphological peculiarities, discussed in Section 5.2.5. Given the large attenuation and attenuation gradient in this galaxy, this indicates that the color gradients found in the corrected profiles of the other galaxies in the sample (most

notably NGCs 891, 4013, and 4565) are not associated with systematics in the attenuation corrections.

Above 300 pc, the remainder of the fast-rotating disks also become bluer with height, like the slow-rotators, while closer to the mid-plane there is more complex behavior. The color gradients for NGC 522, 891 and 4013 flatten at larger heights, but in all cases the amplitude of the gradient is comparable to what is found for the slow-rotators. The vertical gradients at large heights are plausibly interpreted as decreasing metallicity in thicker (presumably older) disk populations. If this is the case, as can be seen in Figure 17 the change in metallicity would easily be factors of 5–10 over the vertical range probed in these galaxies. Regardless, the presence of color gradients indicates these disks are not monolithic.

Near the disk mid-plane several features in the  $J-K_s$  colors and gradients for the fast rotators stand out. First, the gradients tend to flatten and in two cases (NGC 891 and 4565) reverse, leading to bluer mid-plane colors. The clear decrease in corrected  $J-K_s$  color near the midplane of NGC 891, especially for profiles at large distances from NGC 891’s center, is likely the product of young, super-

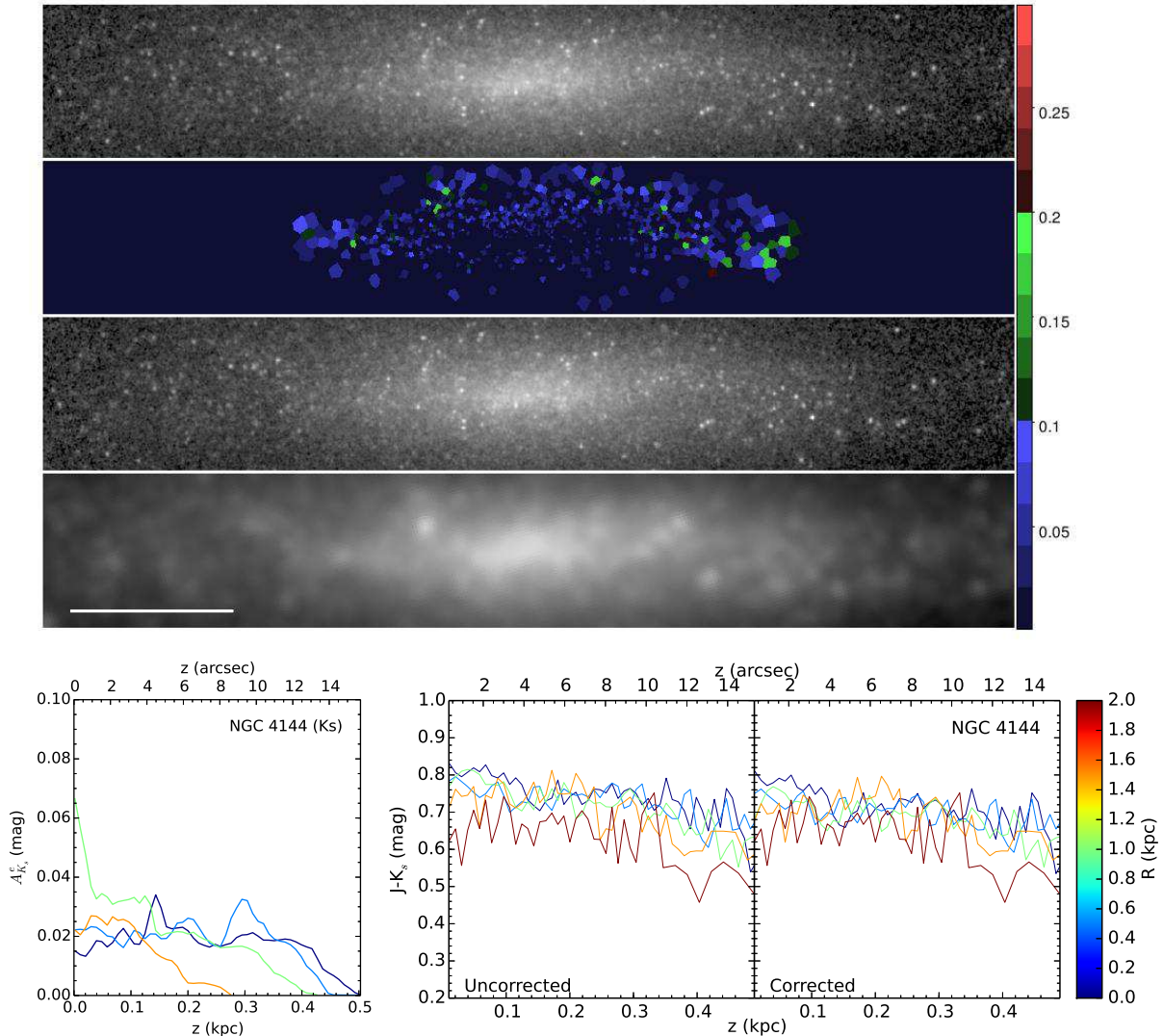


FIG. 15.— Same as Figure 9, but for NGC 4144 (the  $K_s$ -band images grayscale range is from 16.9–21.1 mag arcsec $^{-2}$ ). The  $z$  coordinate used here is the *projected* height; this galaxy is estimated to be inclined at  $85.2 \pm 0.09$  deg (see 5.2.7).

thin disk stars. Not only have we found evidence for such a disk in Paper 1 but NGC 891 is also known to have young stars visible over the dust lane from optical imaging (likely due to the presence of a grand design spiral pattern; Kamphuis et al. 2007). In NGC 4565, a small dip is still observed even in the attenuation-corrected profiles, most noticeably at small radii; it may be the result of a relatively young nuclear star-forming population. The lack of such a large downturn in our other fast rotators indicates they do not have as substantial a young stellar population near their mid-plane compared to NGC 891 and 4565 *unless* their super-thin disk populations are preferentially dominated by red super giants or intermediate-age asymptotic giant branch stars. On the other hand, the colors of all of the fast rotators (besides NGC 1055) have  $J - K_s > 1$ , indicating either a very metal rich giant branch or intermediate age (AGB) population. Testing this conjecture requires additional (spectral) diagnostics sensitive to surface-gravity in cool stars, which we will explore in future work.

For three galaxies in our sample (NGC 522, 891, and 4013), all fast rotators, there are regions in projected

radius and height which are redder than  $J - K_s \sim 1.3$ . For NGC 891 and 522 this only occurs in the very central region of the galaxy. In the context of the discussion in 4, we found it instructive to compare these colors with nearby spiral galaxies, preferably at low inclination, in three other samples. In this projection the effects of dust attenuation in the near-infrared ought to be minimal. To facilitate comparison, we integrated our attenuation-corrected colors over height above the mid-plane, and plot these integrated colors as a function of projected radius in Figure 18. The range of  $J - K_s$  colors decrease significantly in this projection, with only the very central points for NGC 891 and 4013 having  $J - K_s > 1.3$ .

#### 4.2.1. Comparison to other samples

Two of the nearby spiral galaxy samples (Terndrup et al. 1994 and Jarrett et al. 2003) contain galaxies over a wide range of type and inclination. In Terndrup et al. (1994), 7 of the 43 galaxies are convincingly below 45 deg, two of which are early-type spirals (S0/Sa). None of the other 5 have  $J - K_s > 1$ , but of the two early-type galaxies, NGC 2681 (type Sa)



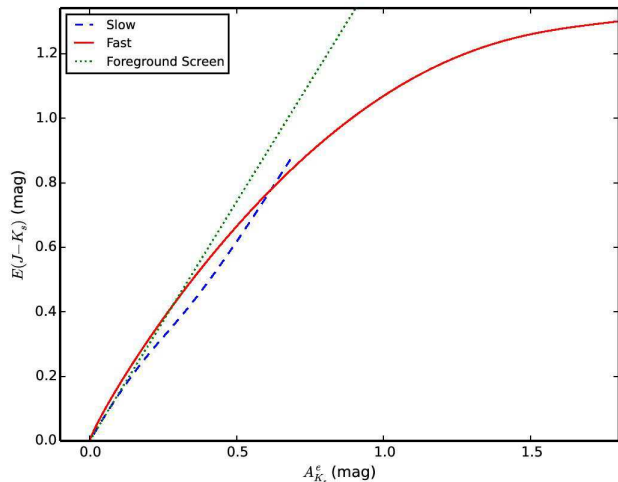


FIG. 16.— Color excess,  $E(J-K_s)$  as a function of  $A_{K_s}^e$  predicted by our RT modeling for fast- and slow-rotators (red solid and blue dashed lines, respectively). For comparison we show this function for the foreground screen model of Cardelli et al. (1989) as a green dotted line.

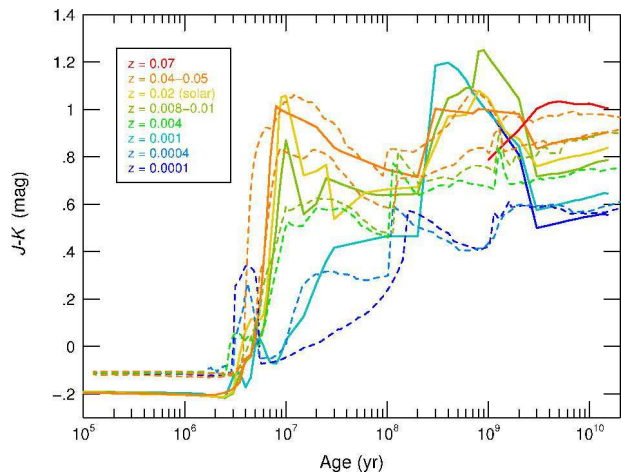


FIG. 17.— Near-infrared colors for SSPs plotted as a function of age and metallicity for the same models used in Figure 4 ( $J-K_s$ ; dashed lines), as well as for the models of Maraston (2005) ( $J-K$ , solid lines).

has colors are between  $1 < J-K_s < 1.35$ , with a mean disk color of  $J-K_s \sim 1.2$ , while the other (NGC 474) has a comparable nuclear color. Jarrett et al. (2003) find that that barred spirals tend to have redder nuclear colors, peaking at  $J-K_s > 1.1$ . Many of these galaxies, however, are considerably inclined (e.g., NGC 253, which has a strong bar and nuclear starburst, with colors of  $J-K_s \sim 2$  in this region).

To focus our comparison on purely low inclination systems, we inspected surface-photometry performed on foreground-corrected 2MASS images from a third study of 231 galaxies with nearly face-on orientation. The sample preferentially selects intermediate type galaxies similar to those we intended to select for the fast-rotators in the current study of edge-on systems. These face-on systems formed the Phase-A parent sample of the DiskMass Survey (DMS) described in Bershady et al. (2010a); the photometry and foreground correction are identical to

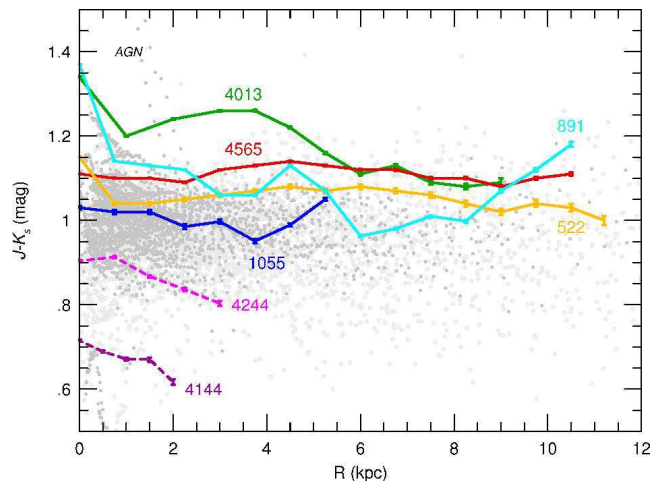


FIG. 18.— Attenuation-corrected  $J-K_s$  colors as a function of projected radius, integrated over  $\pm 2$  kpc in height for fast rotators and  $\pm 1$  kpc for slow rotators. Galaxies in our edge-on sample are represented by colored lines and are labeled by NGC. Points represent photometry of 231, low-inclination, intermediate-type spirals from the parent sample of the DiskMass Survey (see text). Filled (dark grey) points have color errors of  $< 0.1$  mag; open (light grey) points have color errors between 0.1 and 0.2 mag. The inner color profile of two of these galaxies with known AGN are marked.

that described in Martinsson et al. (2013). An important point to note is that the DMS sample was intentionally biased *against* selecting galaxies with strong or large bars.

Figure 18 shows the DiskMass Survey photometry superimposed on the vertically integrated colors of the galaxies in the current study. In general, the 2MASS images have insufficient depth to provide high-precision surface-photometry of spiral disks. We have chosen to limit the face-on sample data to those apertures with color errors  $< 0.1$  mag. This clearly biases the comparison to high surface-brightness disks. To show that this does not significantly affect the resulting color distribution we have also plotted the colors for apertures with errors between 0.1 and 0.2 mag. While there are subtle effects that we will explore elsewhere, the primary change is simply to broaden the color distribution by 0.1 mag due to larger errors. Consequently, we focus our comparison here to the highest-quality surface-photometry of this face-on sample.

In terms of the vertically integrated colors, all but NGC 4013 lie within the observed color distribution of the DMS face-on sample. In the DMS, we find two cases (UGC 1727 and 9149) with  $J-K_s \gg 1.2$  at small radius. Both galaxies have Seyfert nuclei. It is conceivable that the very red  $J-K_s \geq 1.5$  nuclear colors in NGCs 522, 891, and 4013, when seen edge on, are due to small levels of AGN activity. An additional 5 galaxies in the face-on sample have colors reaching  $1.3 < J-K_s < 1.4$  in their central 1-2 kpc (UGC 3701, 4542, 6157, 12270, 12893). This is a small fraction of the entire Phase A sample, and the  $J-K_s$  colors even in the face-on sample could still suffer from some attenuation. However, we do note that NGC 4013 does have the most pronounced and extended x-shaped morphology (see Figure 1) of our sample, which is likely indicative of an extended, and possibly strong bar. Such systems are absent in the DMS sample, and as noted by Jarrett et al. (2003) tend to have redder  $J-K_s$  colors.

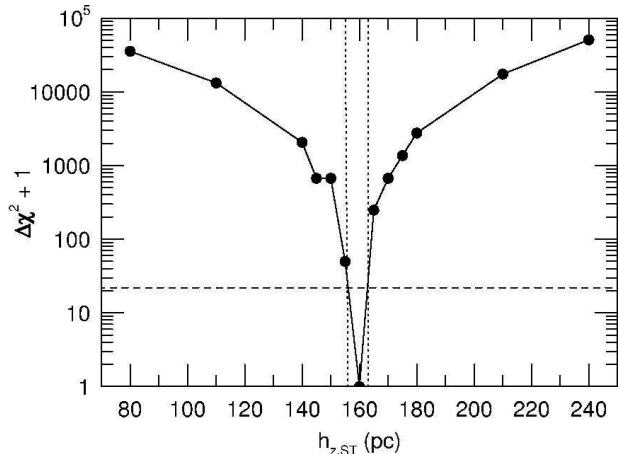


FIG. 19.— Difference between global minimum  $\chi^2$  value for 3-component disk model with 8 degrees of freedom for NGC 891 ( $R > 3\text{kpc}$ ), and minimum  $\chi^2$  values for other values of the vertical scale-height of the super-thin disk component,  $h_{z,ST}$ . The  $3\sigma$  (99.73%) confidence limit on  $h_{z,ST}$  is estimated from the intersection with the dashed horizontal dashed line, given by the dotted vertical lines.

We conclude that the majority of the attenuation estimates and corrected colors are accurate, but that NGC 4013 may be too red by 0.15 mag in  $J - K_s$  at projected radii below 4-5 kpc. If this is indeed a color excess, it implies a systematic error in  $A_{K_s}^e$  of at most 0.1 mag in this one case.

## 5. MULTI-COMPONENT MODEL FITTING

We utilize the same basic fitting scheme as in Paper 1, featuring a 2D Levenberg-Marquardt non-linear least-squares algorithm run multiple times with randomized initial parameter guesses to ensure a global minimum is reached. However, unlike in Paper 1, the assumption that our galaxies are viewed perfectly edge-on is incorrect (especially obvious for NGC 4565). Therefore we add the inclination of the galaxy as another free parameter, which means we can no longer separate the  $R$  and  $z$  components of a galaxy. Following Aoki et al. (1991) the integrated luminosity of an exponential disk is

$$I(R, z) = \rho_0 \int_{-\infty}^{\infty} \exp\left(-\frac{\sqrt{R^2 + t^2 \sin^2 i}}{h_R} - \frac{|z \sin i - t \cos i|}{h_z}\right) dt, \quad (2)$$

where  $i$  is the inclination,  $h_R$  and  $h_z$  are the scale-length and scale-height, and  $\rho_0$  is a normalization factor.

Equation 2 must be numerically integrated, which is time-consuming. We replaced the core of our fitting algorithm with a C++ function to do the actual integration, using a highly efficient double-exponential integration library<sup>8</sup> to ensure fast performance. Computation efficiency is important because each model must be produced along millions of sight-lines in our high resolution images. The load is exacerbated by the need to oversample the data in order to perform an accurate seeing convolution (which we now do in  $z$  and  $R$ , as opposed to just in  $z$ , as we had in Paper 1). As it will become clear

<sup>8</sup> <http://www.codeproject.com/Articles/31550/Fast-Numerical-Integration>

later, another extension of the present work is to include more complicated structure than in our previous analysis. These additions include multiple disk truncations, rings, and Sérsic profiles of varying index,  $n$ .<sup>9</sup> Based on our inability to discern between disks with exponential, sech, or  $\text{sech}^2$  vertical light distributions in Paper 1 we only fit exponential models to reduce the total compute time in our analysis.

Our fitting machinery is further augmented by a distributed network of computers operated by the Center for High Throughput Computing at the University of Wisconsin-Madison. This network uses the publicly available HTCondor software (Thain et al. 2005) to manage job submission and execution, and enables us to massively parallelize our Levenberg-Marquardt fitting procedure<sup>10</sup>. As a consequence we were able to run 1000 iterations per model—a factor of 10 more than in Paper 1—and to explore more free parameters in our models on relatively short timescales. This improvement led to more robust estimates of fitted parameters for increasingly complex galaxy models, without which we would not have been able to characterize the wide variety of morphologies in our sample in a reasonable amount of time. The model fits presented in the following sections used over 25 years of computation time on a single CPU.

### 5.1. Robustness and Uniqueness

Multi-component models of one-dimensional vertical light profiles are prone to degeneracies, manifest in covariance between component vertical scales and normalizations. These degeneracies are ameliorated (and the covariance reduced) by fitting the two-dimensional light distribution instead of one-dimensional profiles (e.g., see discussion in Morrison et al. 1997). However, even with the two-dimensional profile fitting we undertake here, it is difficult to anticipate the degree of model parameter degeneracy without directly understanding the uncertainties in their estimation. Given the complexity of our models, we have made an assessment of the degree to which this is an issue in our analysis.

In the subsequent analysis, we use the boot-strap method to estimate uncertainties in our parameter estimates. Standard error estimates from the nonlinear fitting are often too small (Morrison et al. 1994), while mapping out the full  $N$ -dimensional  $\chi^2$  space of our models is computationally prohibitive, even with the distributed processing described in the previous section. The boot-strap errors are small (often under 2%), which provides an initial indication that parameter covariance is not a significant concern.

To verify that boot-strap error estimates are reasonable, we explored the model for NGC 891 that we will come to in §5.2.1, given in the first column of Table 3.

<sup>9</sup> Because even a Sérsic component with a large ellipticity will be much less flat than a disk and all of our galaxies are very close to edge-on, we treat all bulges as though they are viewed edge-on to save on computational time.

<sup>10</sup> Due to its complexity and the degree of customization required to make our code compatible with our distributed computing environment, this software is not as readily amenable to general use by other researchers. However, we have made it available at <https://github.com/AndrewRook/astro/tree/master/galaxyfit>, to serve at least as a resource for others seeking to add distributed computing capabilities to their software.

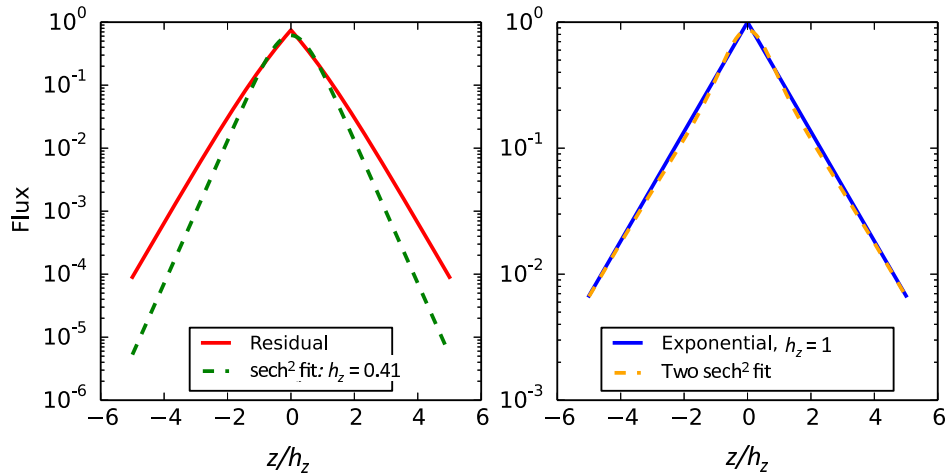


FIG. 20.— Decomposition of exponential vertical fitting function into two  $\text{sech}^2$  functions, as described in the text. The left-hand panel shows the fit of the second  $\text{sech}^2$  function to the residual from the difference between the exponential and first  $\text{sech}^2$  functions, normalized at large heights,  $z$ . The right hand panel shows the resulting composite profile compared to the original exponential profile.

This model has three exponential disks fit to the two-dimensional light distribution outside of a 3 kpc radius from the center of the galaxy. We chose this model because it is representative of our model complexity for the one galaxy where we have reanalyzed the attenuation correction; analysis of parameter robustness is particularly relevant to later discussion. The model has 8 free parameters since the thick disk scale length and scale height is fixed to literature values, and the inclination and center radial position are fixed (the center vertical position is a free parameter, but it is not tabulated.) We focus here on the super-thin scale-height,  $h_{z,ST}$ , as this is a parameter of central interest in this work, and because it might reasonably be considered to be covariant with the scale-height of the thin-disk component  $h_{z,T}$ .

Our numerical experiment considered a series of fixed values of  $h_{z,ST}$  between 80 and 240 pc, bracketing the best-fitting value of 160 pc. By allowing the model to optimize the remaining 7 parameters for each fixed value of  $h_{z,ST}$ , we find the minimum  $\chi^2$  value rapidly increases as  $h_{z,ST}$  departs from the best fit value of 0.16 kpc. Based on a  $\Delta\chi^2$  confidence interval, we find  $h_{z,ST}$  is constrained to  $\pm 3$  pc at the 99.73% ( $3\sigma$ ), consistent with our boot-strap estimates. Within these constraints the variations in the remaining six parameters are equally small. In short, the parameter estimates on scale-height, scale-length and surface-brightness from our model fitting are remarkably well constrained, with little covariance given the adopted model fitting functions.

However, there is a second flavor of degeneracy which arises from our choice of fitting functions. This was explored in Paper 1 for NGC 891 in the context of varying the vertical luminosity profile from exponential to a  $\text{sech}^2$  distribution. It is straightforward to show that it is possible to decompose a single exponential function into two  $\text{sech}^2$  with a high degree of accuracy. One example is shown in Figure 20. In this case, one of the  $\text{sech}^2$  components is required to have the same asymptotic scale-height and normalization as the exponential. The result is that the second  $\text{sech}^2$  has half the luminosity and  $\sim 40\%$  of the scale-height of the original exponential. In this one-dimensional case, it would imply that every exponential super-thin disk component we fit in our sub-

sequent analysis could be reinterpreted as having a much thinner  $\text{sech}^2$  sub-component.

This interpretation is not entirely fair because it is based on a one-dimensional analysis and it makes some a priori assumption of what is the correct distribution function. In fitting two-dimensional light distribution with either exponential or  $\text{sech}^2$  vertical distribution functions, we find we need the *same* number of components (Schechtman-Rook & Bershady 2013). In other words, there is no mathematical motivation for invoking an additional component. For NGC 891, instead we found in Paper 1 that the best-fitting multi-component disk models with  $\text{sech}^2$  vertical profiles tend to have shorter scale-heights and longer (exponential) scale-lengths than those models with exponential vertical profiles. Both of these relative changes are at the  $\sim 25\%$  level such that the effect on disk oblateness is roughly a factor of 1.5. The change in the scale-height is qualitatively consistent with the illustration in Figure 20, but the effect is smaller, and again there is no need for extra components.

Concerning the point about what distribution function is correct, Comerón et al. (2011c), for example, take a physical approach of deriving dynamically consistent fitting functions. While in some sense this is desirable, it is a one-dimensional dynamical model and hence limited to fitting one-dimensional light profiles. Since we wish to mitigate parameter covariance in multi-component models by fitting the two-dimensional light distribution, and because the corresponding dynamical model becomes considerably more complicated, in our analysis we provide a phenomenological description of the light profile, parameterized with a simple, analytic function. In any event, the fitting function derived by Comerón et al. 2011c is intermediate between an exponential and  $\text{sech}^2$  function, and so it is bracketed by the limiting phenomenological models considered in this discussion.

To summarize: We adopt an exponential vertical fitting function. Our resulting model parameters are well constrained, with little parameter covariance. However, our resulting model parameters deviate systematically from an identical analysis adopting a different vertical fitting function, but in a well-defined way. In the case of a  $\text{sech}^2$  function, the conversion between parameteriza-

tions can be approximated given the above information based on the NGC 891 modelling of Paper 1.

### 5.2. Individual Galaxy Fits

While we use the same general framework to find our best fits, each galaxy is unique; there is no ‘one-size-fits-all’ fitting procedure. Therefore, while some elements may be similar, we discuss our fits to each galaxy individually. We order the galaxies in this section not by NGC number but rather by the complexity of the system, starting with our four fast-rotators and then moving to our two slow-rotating galaxies. Additionally, for NGCs 891, 4244, and 4565, the three most spatially extended galaxies in our sample, we boxcar-smoothed the images with a kernel  $0''.3$  on a side. By performing this smoothing (roughly  $3 \times 3$  pixels on WHIRC) we were able to dramatically decrease our fitting times without significantly impacting our ability to recover very thin galaxy structure, as the resolution of these images was more than twice the size of the smoothing kernel.

It is also worth discussing the nomenclature we will use, which has not always been consistent in the literature. This is especially relevant because the light distribution of the galaxies in our sample does not always follow the nested super-thin + thin + thick disk paradigm of the MW and NGC 891. (We prefer to use the term ‘super-thin’ instead of ‘young’ or ‘star-forming’ because with our data alone the true age of these disks is unknown, although in some cases, as discussed in the previous section, the  $J - K_s$  indicates the mid-plane light is indeed dominated by young stars.) Generally, when confronted with a galaxy which requires three disks with scale-heights all significantly different from each other, we use super-thin, thin, and thick to describe the three disks as a function of increasing scale-height. For galaxies with two disks we use ‘thin’ and ‘thick’, and only ‘thin’ for apparently single-disk systems; generally we find that these disks have similar values of scale-height as the thin and thick disks in full three disk systems like the MW. In one case (NGC 1055) we find that the two most luminous disks have comparable scale-heights and total luminosities, but very different scale-lengths, and so we refer to them simply as disks 1 and 2.

It is important to note that our naming convention does not, nor is it intended to, convey any information about the astrophysics of these galaxies. It is possible, for instance, that two disks which we give the same designation to are the result of very different formation processes. Our naming scheme only provides a convenient reference for the different components of a galaxy. The model  $K_s$ -band luminosities given in the following tables are in solar units, adopting  $L_{\odot, K} = 3.909 \times 10^{18} \text{ erg s}^{-1} \text{ Hz}^{-1}$ , as we did in Paper 1.

#### 5.2.1. NGC 891

Despite the changes to our attenuation correction methodology, we do not expect to find significant changes in the intrinsic disk morphologies. Therefore we begin in much the same way as Paper 1, although we skip the one and two disk models and first constrain a model with three disks at radii larger than 3 kpc. Additionally, after careful inspection of NGC 891’s surface brightness profiles, we added an outer truncation of the super-thin disk

to this model; as we will show in subsequent sections such a feature is fairly common in the fast rotating galaxies in our sample.

The results of this model are shown as blue dashed lines in Figure 21 and in the left column of Table 3. The new outer disk truncation occurs around 10 kpc, and can clearly be seen on the right side of Figure 21. The new attenuation correction results in two main changes to our results from Paper 1: the *total* luminosity of the galaxy is  $\sim 25\%$  fainter, and the luminosity profile is shallower. The luminosity change is entirely due to the change in attenuation correction, and is independent of the model fitting. The profile shape change is reflected in larger super-thin and thin disks scale-heights (100% and 62% increase, respectively) and scale-lengths (68% and 47% increase, respectively).<sup>11</sup> Given our discussion and analysis in §5.1, these changes are robust, and reflect the change in the profile shape, and are not due to parameter covariance. Despite the decrease in the total luminosity as well as the increase in the scale-height of the super-thin disk, the luminosity ratios between all of NGC 891’s stellar components are essentially unchanged between Paper 1 and this work.

Using this model to fix most of the disk parameters, we then extended our fits into the central portions of NGC 891 by adding an inner truncation for all three disks, a bar (mimicked by an exponential disk), as well as a small nuclear disk—the same scheme as in Paper 1. The best fitting instance of this model is shown as the solid red line in Figure 21 and in the right column of Table 3. This model generally does a good job of fitting NGC 891’s surface brightness profile, roughly comparable to the fit quality of the equivalent model in Paper 1 (See Figure 21 of that work for the most direct comparison). The change in the  $\chi^2$  values between the two models in Table 3 is significant, as can be seen in the residual images in Figure 21.

#### 5.2.2. NGC 4013

Comerón et al. (2011b) performed 1D disk fits to this galaxy and found that three stellar disks were required to fit the IRAC  $3.6 \mu\text{m}$  vertical light profile. They adopt the same distance for NGC 4013 as we do, and their thinnest disk has  $h_z \sim 125$  pc while their intermediate-height disk has  $h_z \sim 565$  pc, comparable to the super-thin and thin disks in the MW and NGC 891. Furthermore, they found that the thickest of these three disks had a scaleheight of  $\sim 3$  kpc, about two times larger than ‘normal’ for a traditional thick disk.

Similar to Paper 1, we first exclude the central 4 kpc of the galaxy, chosen by eye to avoid contamination from NGC 4013’s X-shaped orbits, and focus our fit on the disk structure. Because of NGC 4013’s almost exactly edge-on inclination, we fix the inclination at  $90^\circ$ . Our data go deep enough to easily recover the two thinner disks in NGC 4013, but we are not able to probe large enough heights to easily fit the extended  $h_z = 3$  kpc disk. However, by fixing the scaleheight of a third disk component to the scaleheight found for this disk by Comerón et al. (2011b), we find that our models do benefit from its in-

<sup>11</sup> These changes are relative to the results using exponential vertical fitting functions in Schechtman-Rook & Bershady 2013; this work also considers  $\text{sech}^2$  vertical fitting functions.

TABLE 3  
NGC 891 BEST-FITTING MODELS

Parameter <sup>a</sup>	Value		Units
	Three Disks <sup>b</sup>	Three Disks+ Bar+Nuclear Disk <sup>c</sup>	
$\mu_{0,ST}$	14.35±0.01	14.41±0.03	mag arcsec <sup>-2</sup>
$h_{R,ST}$	3.29±0.03	3.36±0.05	kpc
$h_{z,ST}$	0.16±0.00	0.16±0.00	kpc
$L_{ST}$	$4.20 \times 10^{10}$	$2.99 \times 10^{10}$	$L_{\odot,K}$
$\mu_{0,T}$	15.93±0.02	15.93 <sup>g</sup>	mag arcsec <sup>-2</sup>
$h_{R,T}$	5.70±0.06	5.70 <sup>g</sup>	kpc
$h_{z,T}$	0.47±0.00	0.47 <sup>g</sup>	kpc
$L_T$	$6.21 \times 10^{10}$	$5.67 \times 10^{10}$	$L_{\odot,K}$
$\mu_{0,Th}$	18.46±0.02	18.46 <sup>g</sup>	mag arcsec <sup>-2</sup>
$h_{R,Th}$	4.80 <sup>d</sup>	4.80 <sup>d</sup>	kpc
$h_{z,Th}$	1.44 <sup>d</sup>	1.44 <sup>d</sup>	kpc
$L_{Th}$	$1.56 \times 10^{10}$	$1.38 \times 10^{10}$	$L_{\odot,K}$
$\mu_{0,nuc}$	...	12.89±0.02	mag arcsec <sup>-2</sup>
$h_{R,nuc}$	...	0.20±0.00	kpc
$h_{z,nuc}$	...	0.10±0.00	kpc
$L_{nuc}$	...	$7.62 \times 10^9$	$L_{\odot,K}$
$\mu_{0,bar}$	...	15.02±0.01	mag arcsec <sup>-2</sup>
$h_{R,bar}$	...	1.33±0.02	kpc
$h_{z,bar}$	...	0.57±0.00	kpc
$L_{bar}$	...	$2.52 \times 10^{10}$	$L_{\odot,K}$
$R_{trunc,1}^e$	...	2.79±0.08	kpc
$R_{trunc,2}^f$	9.92±0.03	9.92 <sup>g</sup>	kpc
$L_{tot}$	$1.20 \times 10^{11}$	$1.33 \times 10^{11}$	$L_{\odot,K}$
$\chi_{\nu,inner}^2$	18.62	4.96	...
$\chi_{\nu,outer}^2$	3.47*	3.47	...
$\chi_{\nu,total}^2$	7.39	3.86*	...

<sup>a</sup> *ST*, *T*, *Th*, *nuc*, and *bar* denote parameters that we associate with the super-thin disk, thin disk, thick disk, nuclear disk, and bar (respectively).

<sup>b</sup> Only fit to regions of the galaxy with  $R > 3$  kpc.

<sup>c</sup> Fit performed over entire radial range of data.

<sup>d</sup> Fixed to literature value (see Paper 1 for details).

<sup>e</sup> Inner truncation for the super-thin, thin, and thick disks, outer truncation for the bar and nuclear disks.

<sup>f</sup> Outer truncation for the super-thin disk only.

<sup>g</sup> Fixed to the value found in the Three Disks model.

<sup>h</sup> Reduced  $\chi^2$ . *inner* and *outer* correspond to the regions inside and outside of the 3 kpc fitting cutoff, while *total* is for both regions together. (\*) denotes the  $\chi_{\nu}^2$  that was minimized by each model.

clusion. A plot showing our best-fitting 3-disk model is shown in Figure 22, with the individual parameters detailed in Table 4.

It is clear from Figure 22 that NGC 4013 requires an inner truncation for all three disks as well as an outer truncation for the thinnest disk only. Therefore, as for NGC 891 we add an abrupt inner truncation to all three disk components, as well as an outer truncation for just the super-thin disk. To improve computation time, we fix the two thicker disks at the best-fitting values from the original un-truncated disks-only model; we leave the super-thin disk parameters free to ensure that the outer truncation (which was not masked out in our disk-only fits) is not biasing the super-thin disk fit.

Following our procedure for NGC 891, to fit the inner portions of NGC 4013 we added an exponential disk with an outer truncation at the radius of the inner disk truncation to mimic a bar component, as well as a nuclear star-forming disk. The best-fitting bar has a scale-height of 490 pc and scale-length of 1.46 kpc. This is roughly comparable to the scale-height of the intermediate-thickness disk component, but with only half the scale-length. The results for this more complex model are shown in Figure

22 and Table 4. The  $\chi^2$  values are reduced significantly compared to the original model, as seen in the residual images.

Like NGC 891, the exponential bar model for NGC 4013 is an imperfect fit at small radii. The model overpredicts the flux at small radii and medium heights, and underpredicts the light at the very center of the galaxy. These discrepancies are likely due to the fact that our exponential disk assumption, while a fairly close match to NGC 891's bar, is inadequate for the X-orbits visible in NGC 4013 (the strongest such feature in our sample). A model with a Sérsic bulge instead of an exponential bar was also tried, but did not improve the correspondence between data and model (and in fact made the fit worse).

However, given the fact that this mismatch is only an issue at very small radii, it should not impact the disk parameters we are most interested in measuring. It is clear we are accurately fitting NGC 4013's disks, and obtain reasonable results for our fitted parameters. We find a scale-height of 540 pc for our thin disk, almost identical to that of the intermediate disk in Comerón et al. (2011b). Our super-thin disk has a scale-height  $\sim 1.5$

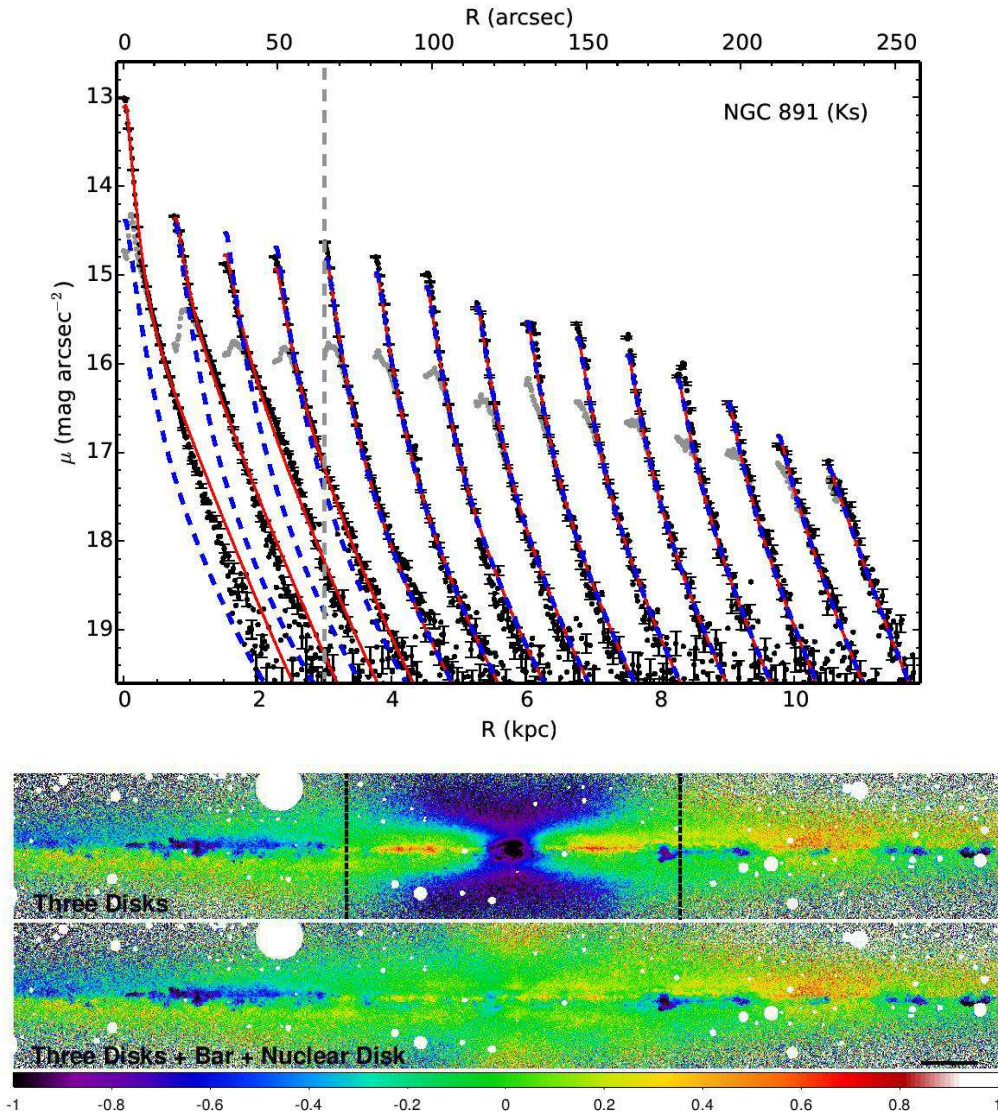


FIG. 21.— Top: best-fitting models for NGC 891. Gray and black points represent un-corrected and attenuation corrected data (respectively), where each set of points shows a vertical profile starting at the radius of the innermost point. The blue dashed lines show the best fitting three disk model (with only an outer truncation for the super-thin disk), fit to all regions outside of 3 kpc in radius (denoted by the vertical gray dashed line). The solid red lines show the best fitting three disk + exponential bar + nuclear disk model, fit to the entire profile. This latter model also has an inner truncations for all three disks and an outer truncation for the thinnest disk, and were fit at all radii. To improve S/N the data in the 1D profiles have all been binned to  $5'' \times 0''.3$  ( $R \times z$ ). Bottom: magnitude residual (data - model) images. Dashed black lines show the radial limits of our fits, where appropriate, and the solid black line indicates 1 kpc at our assumed distance. Details of the model parameters are in Table 3

times as large as Comeron’s thinnest disk. This discrepancy could arise because of our different choices of fitting function (in Paper 1 we found that more rounded vertical profiles produced thinner disks, especially for thinner components), or from our use of 2D fits rather than multiple 1D analyses.

The addition of the outer super-thin disk truncation is quite important for accurately determining the scale-length of the super-thin disk, which increases by  $\sim 15\%$  in the model with a bar. The super-thin disk has a scale-length only 80% as long as the thin disk, but is 2.3 times flatter than the thin disk. The thick disk scale-length is 1.4 times as long as the thin disk, but due to its extremely large scale-height this still results in a decrease of  $\frac{h_R}{h_z}$  to about 1.3.

### 5.2.3. NGC 4565

To avoid NGC 4565’s obvious inner truncation we first restrict our models to fit outside of  $R=5$  kpc. We find (as do Comeron et al. 2011c) that only two disks are needed to model most of the light outside of this radius, except for the contribution from the ring-like structure visible in Figure 11. We therefore chose to change our models to ones with two disks and a ring, adding to our fitting software a gaussian ring with the same functional description

TABLE 4  
NGC 4013 BEST-FITTING MODELS

Parameter <sup>a</sup>	Value		Units
	Three Disks <sup>b</sup>	Three Disks+ Bar+Nuclear Disk <sup>c</sup>	
$\mu_{0,ST}$	14.27±0.00	14.53±0.01	mag arcsec <sup>-2</sup>
$h_{R,ST}$	1.94±0.01	2.25±0.01	kpc
$h_{z,ST}$	0.21±0.00	0.21±0.00	kpc
$L_{ST}$	$4.36 \times 10^{10}$	$2.25 \times 10^{10}$	$L_{\odot,K}$
$\mu_{0,T}$	16.05±0.02	16.05 <sup>e</sup>	mag arcsec <sup>-2</sup>
$h_{R,T}$	2.80±0.01	2.80 <sup>e</sup>	kpc
$h_{z,T}$	0.60±0.01	0.60 <sup>e</sup>	kpc
$L_T$	$3.49 \times 10^{10}$	$2.50 \times 10^{10}$	$L_{\odot,K}$
$\mu_{0,Th}$	19.04±0.02	19.04 <sup>e</sup>	mag arcsec <sup>-2</sup>
$h_{R,Th}$	3.95±0.01	3.95 <sup>e</sup>	kpc
$h_{z,Th}$	2.96 <sup>d</sup>	2.96 <sup>d</sup>	kpc
$L_{Th}$	$1.55 \times 10^{10}$	$1.28 \times 10^{10}$	$L_{\odot,K}$
$\mu_{0,nuc}$	...	13.81±0.03	mag arcsec <sup>-2</sup>
$h_{R,nuc}$	...	0.13±0.00	kpc
$h_{z,nuc}$	...	0.11±0.00	kpc
$L_{nuc}$	...	$2.34 \times 10^9$	$L_{\odot,K}$
$\mu_{0,bar}$	...	14.91±0.00	mag arcsec <sup>-2</sup>
$h_{R,bar}$	...	1.46±0.01	kpc
$h_{z,bar}$	...	0.49±0.00	kpc
$L_{bar}$	...	$2.54 \times 10^{10}$	$L_{\odot,K}$
$R_{trunc,1}^f$	...	2.94±0.01	kpc
$R_{trunc,2}^g$	...	10.29±0.01	kpc
$L_{tot}$	$9.40 \times 10^{10}$	$8.80 \times 10^{10}$	$L_{\odot,K}$
$\chi_{\nu,inner}^2$	3.21	0.97	...
$\chi_{\nu,outer}^2$	0.25*	0.24	...
$\chi_{\nu,total}^2$	1.57	0.57*	...

<sup>a</sup> *ST*, *T*, *Th*, *nuc*, and *bar* denote parameters that we associate with the super-thin disk, thin disk, thick disk, nuclear disk, and bar (respectively).

<sup>b</sup> Only fit to regions of the galaxy with  $R > 4$  kpc.

<sup>c</sup> Fit performed over entire radial range of data.

<sup>d</sup> Fixed to literature value (see text for details).

<sup>e</sup> Fixed to the value found in the Three Disks model.

<sup>f</sup> Inner truncation for the super-thin, thin, and thick disks, outer truncation for the nuclear disk and bar.

<sup>g</sup> Outer truncation for the super-thin disk.

<sup>h</sup> Reduced  $\chi^2$ . *inner* and *outer* correspond to the regions inside and outside of the 4 kpc fitting cutoff, while *total* is for both regions together. (\*) denotes the  $\chi_{\nu}^2$  that was minimized by each model.

as used in de Looze et al. (2012):

$$I(R, z) = \rho_0 \int_{-\infty}^{\infty} \exp\left(-\frac{(\sqrt{R^2 + t^2 \sin^2 i} - R_0)^2}{2\sigma_0^2} - \frac{|z \sin i - t \cos i|}{h_z}\right) dt, \quad (3)$$

where  $R_0$  is the central ring radius and  $\sigma_0$  is the radial dispersion of the ring. To help fit the thick disk, we used an average of the thick disk scale-heights found in the 1D fits done for NGC 4565 by Comerón et al. (2011c). Because their fits produced much smaller values for the thick disk  $h_z$  in their large radii bins ( $14.5 \text{ kpc} \lesssim R \lesssim 23 \text{ kpc}$ , regions outside of our WHIRC coverage), we averaged only the values in their two bins nearest the center of NGC 4565. (Note that all of the fits in Comerón et al. 2011c are outside of the radii where the ring feature is present.) We leave the scale-length and central surface brightness as free parameters, as they are not reported in Comerón et al. (2011c). The results of this fit are shown as the blue dashed line in Figure 23 and listed in the leftmost column of Table 5. This provides an adequate fit outside of  $R = 5 \text{ kpc}$ , but deviates substantially from

the data within that radius.

While our fitting of NGC 4013 closely followed the same procedure as we followed for NGC 891 in Paper 1, producing a good fit to NGC 4565 at all radii was a significant challenge, due largely to the unique morphology of this system. First, unlike in NGCs 891 and 4013, where the disk-only models clearly overpredict the central surface brightness at small radii, in NGC 4565 the model described above remains comparable or fainter than the peak surface brightness at all radii. Therefore it is unclear whether a disk truncation is actually needed, or if the ring merely creates the *appearance* of such a feature.

To improve our model fits at small radii and to investigate whether or not our data support an inner disk truncation, we next held constant the free parameters of the two disks from our previous best-fitting model and added a nuclear disk and Sérsic bulge.<sup>12</sup> This model was fit to the full radial range of data, and since the ring abutted our 5 kpc cutoff from the previous fit we allowed it to vary freely. The results of this fit are reported in

<sup>12</sup> We attempted to use an exponential bar-like component instead of a bulge but it produced a poor fit, possibly because unlike NGCs 891 and 4013, NGC 4565 has a very faint X pattern.

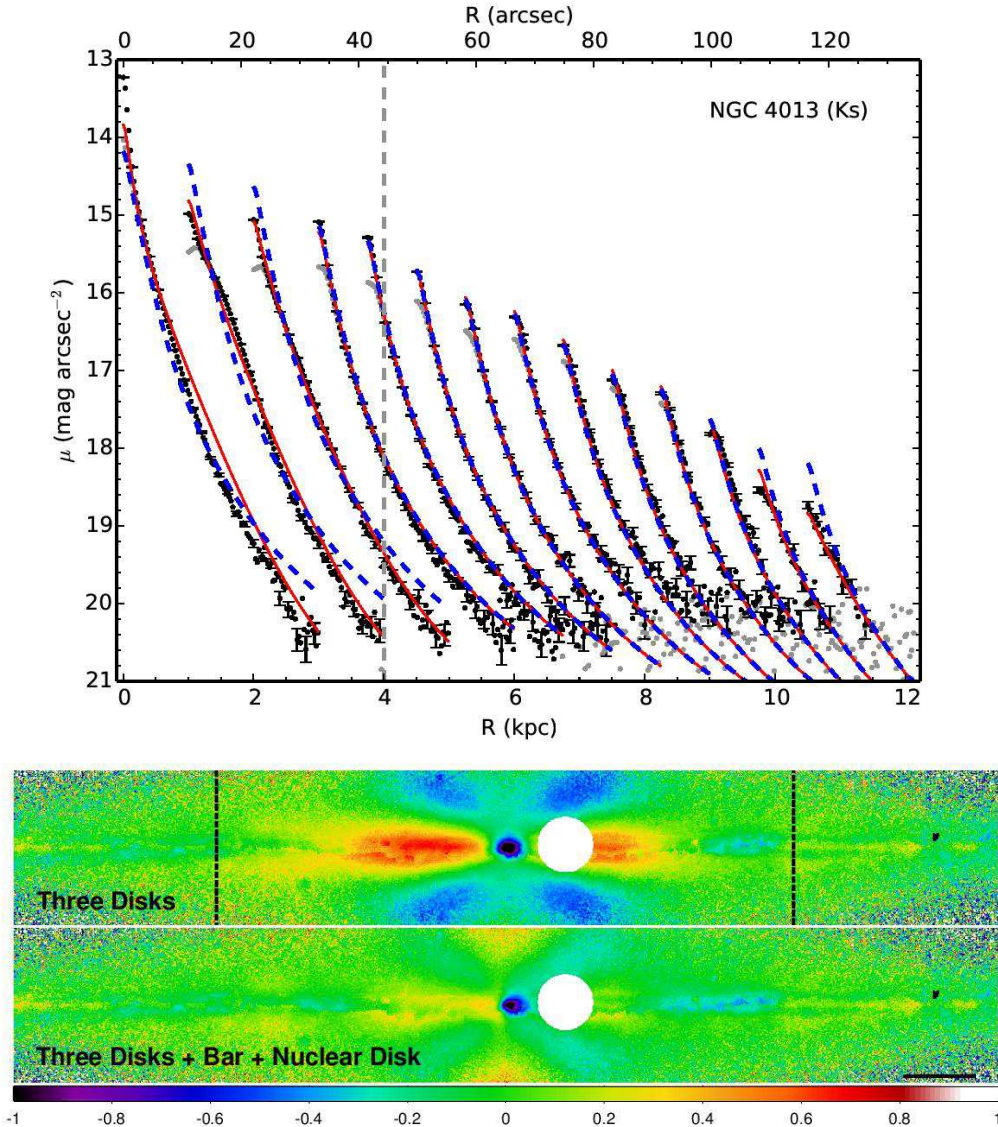


FIG. 22.— Similar to Figure 21, but for NGC 4013. The blue dashed lines show the best fitting three disk model (with no truncations), fit to all regions outside of 4 kpc in radius (denoted by the vertical gray dashed line). The solid red lines show the best fitting three disk + exponential bar + nuclear disk model. This latter model also has an inner truncations for all three disks and an outer truncation for the thinnest disk, and were fit at all radii. To improve S/N the data in the 1D profiles have all been binned to  $5'' \times 0''.3$  ( $R \times z$ ). Details of the model parameters are in Table 4.

the central column of Table 5 and plotted in Figure 23 with green dot-dashed lines. This model is a significant improvement at small radii from the initial model, but in this radial range it over-predicts the amount of light at the smallest and largest heights. From our experience fitting NGC 891 and 4013, this indicates the need for an inner disk truncation (to remove model light from the mid-plane) but without the redistribution of light into a bar (to remove light at large height).

We then repeated this fit, adding in an outer truncation for the nuclear disk and an inner truncation for the other two disks. This third model is plotted with red solid lines in Figure 23 and shown in the right column of Table 5. The addition of the truncation allows this model to match the data at large heights over the entire radial range. However, while significantly better than the model with no truncation (the corrected

Akaike information criterion, AIC,<sup>13</sup> drops by  $\sim 8\%$ ; Burnham & Anderson 2002) even this model is unable to fully reproduce the detailed shape of the light profiles near the mid-plane. In particular, the offset peaks and central troughs of the profiles between  $2 \lesssim R \lesssim 5$  kpc seen in Figure 23 remain problematic.

One reason our models maybe failing to match the complex mid-plane structure is that we are seeing an overabundance of light from the inner edge of NGC 4565's ring due to dust scattering of bulge light. To investigate this we looked at the profiles of the individual quadrants of NGC 4565, under the assumption that this effect would show up as a systematic offset in surface brightness between quadrants showing the back

<sup>13</sup> In the limit where the number of data points is much larger than the number of model parameters,  $AIC \sim \chi^2 + 2k$ , where  $k$  represents the number of model parameters.



TABLE 5  
NGC 4565 BEST-FITTING MODELS

Parameter <sup>a</sup>	Value			Units
	Two Disks+Ring+		Two Disks+Ring+Bulge+	
	Two Disks+Ring <sup>b</sup>	Bulge+Nuclear Disk <sup>c</sup>	Nuclear Disk+Truncation <sup>c</sup>	
$\mu_{0,T}$	15.38±0.01	15.38 <sup>d</sup>	15.38 <sup>d</sup>	mag arcsec <sup>-2</sup>
$h_{R,T}$	5.96±0.01	5.96 <sup>d</sup>	5.96 <sup>d</sup>	kpc
$h_{z,T}$	0.35±0.00	0.35 <sup>d</sup>	0.35 <sup>d</sup>	kpc
$L_T$	$8.02 \times 10^{10}$	$8.02 \times 10^{10}$	$6.04 \times 10^{10}$	$L_{\odot,K}$
$\mu_{0,Th}$	18.86±0.02	18.86 <sup>d</sup>	18.86 <sup>d</sup>	mag arcsec <sup>-2</sup>
$h_{R,Th}$	5.44±0.06	5.44 <sup>d</sup>	5.44 <sup>d</sup>	kpc
$h_{z,Th}$	2.23 <sup>e</sup>	2.23 <sup>e</sup>	2.23 <sup>e</sup>	kpc
$L_{Th}$	$1.89 \times 10^{10}$	$1.89 \times 10^{10}$	$1.36 \times 10^{10}$	$L_{\odot,K}$
$\mu_{0,nuc}$	...	13.45±0.02	13.49±0.02	mag arcsec <sup>-2</sup>
$h_{R,nuc}$	...	0.16±0.00	0.18±0.00	kpc
$h_{z,nuc}$	...	0.18±0.00	0.17±0.00	kpc
$L_{nuc}$	...	$6.55 \times 10^9$	$6.71 \times 10^9$	$L_{\odot,K}$
$\mu_{0,ring}$	18.07±0.04	18.33±0.01	16.11±0.08	mag arcsec <sup>-2</sup>
$r_{0,ring}$	5.34±0.02	5.39±0.01	4.55±0.23	kpc
$\sigma_{0,ring}$	0.42±0.01	0.41±0.01	0.94±0.03	kpc
$h_{z,ring}$	0.27±0.00	0.36±0.01	0.30±0.01	kpc
$L_{ring}$	$4.67 \times 10^9$	$4.94 \times 10^9$	$2.69 \times 10^{10}$	$L_{\odot,K}$
$\mu_{0,bulge}$	...	15.48±0.01	15.20±0.01	mag arcsec <sup>-2</sup>
$R_e$	...	1.50±0.00	1.77±0.03	kpc
$a/b$	...	1.36±0.00	1.73±0.03	kpc
$n^f$	...	0.69±0.01	0.71±0.01	
$L_{bulge}$	...	$3.26 \times 10^{10}$	$4.50 \times 10^{10}$	$L_{\odot,K}$
$i$	87.59±0.01	87.59 <sup>d</sup>	87.59 <sup>d</sup>	degrees
$R_{trunc,1}^g$	...	...	5.68±0.35	kpc
$L_{tot}$	$1.04 \times 10^{11}$	$1.43 \times 10^{11}$	$1.53 \times 10^{11}$	$L_{\odot,K}$
$\chi_{\nu,inner}^2$ <sup>h</sup>	122.16	7.19	6.14	...
$\chi_{\nu,outer}^2$ <sup>h</sup>	3.23*	3.24	3.33	...
$\chi_{\nu,total}^2$ <sup>h</sup>	52.15	4.87*	4.49*	...

<sup>a</sup>  $T$ ,  $Th$ ,  $nuc$ , and  $ring$  denote parameters that we associate with the thin disk, thick disk, nuclear disk, and ring (respectively).

<sup>b</sup> Only fit to regions of the galaxy with  $R > 5$  kpc.

<sup>c</sup> Fit performed over entire radial range of data.

<sup>d</sup> Fixed to Two Disks+Ring model value.

<sup>e</sup> Fixed to literature value (see text for details).

<sup>f</sup> Sérsic index.

<sup>g</sup> Inner truncation for the thin and thick disks, outer truncation for the nuclear disk.

<sup>h</sup> Reduced  $\chi^2$ . *inner* and *outer* correspond to the regions inside and outside of the 5 kpc fitting cutoff, while *total* is for both regions together. (\*) denotes the  $\chi^2_{\nu}$  that was minimized by each model.

and edges of the ring. However, we could find no concrete evidence for this offset. In fact, it appears that two quadrants diagonally opposite from each other (the upper left and lower right quadrants in Figure 1) show an excess of flux. It is not clear why this should be, although if NGC 4565 did have a weak bar at this position angle, that might explain the observed behavior. While a full exploration of this effect is beyond the present scope, it should not affect our analysis of the broader disk parameters.

Our best-fitting model bulge has an effective radius of 1.77 kpc and an axial ratio of  $\sim 1.75$ . Additionally, it has a Sérsic index of 0.71. This is close to an exponential radial light profile, but the light distribution is much less oblate than the central light concentrations we modeled as “bars” in the previous two galaxies NGC 891 and 4013. The final disk components yield a thin disk with  $h_z = 350$  pc,  $\sim 90\%$  the height found at  $3.6\mu\text{m}$  by Comerón et al. (2011c) (averaged over all of their fits) and  $\sim 75\%$  the optical height fit by de Looze et al. (2012). In this case differences between fitting functions would only serve to increase this disparity, as adjusting from an exponential to a sech or sech<sup>2</sup> vertical distri-

bution would only decrease our  $h_z$ . A survey of other literature fits indicates that overall our thin-disk  $h_z$  is anomalously small (Wu et al. 2002), although most of these studies assume that NGC 4565 is perfectly edge-on, which would bias fits to larger values of  $h_z$ . However, the model of de Looze et al. (2012) has inclination comparable ( $\sim 0.25^\circ$  smaller) than ours. Given the fact that most of the larger measurements for this quantity come from optical data (with the exception of Rice et al. 1996) and that our results are close to those found at  $3.6\mu\text{m}$  by Comerón et al. (2011c), it seems plausible that this discrepancy could be the result of insufficient reddening corrections of the optical light profiles.

None of our models produce fits containing a (non-nuclear) disk component with a scale-height consistent with a MW, NGC 4013, or NGC 891-like super-thin disk. The stellar ring, the component spatially associated with CO emission (and therefore star formation), has a scale-height  $\gtrsim 85\%$  of the thin disk. While our inability to fit the offset peaks of the vertical profiles for  $2 \gtrsim R \gtrsim 5$  kpc could potentially leave room for a super-thin component, given the quality of our fits at larger radii such a component would likely be quite faint, with a smaller relative

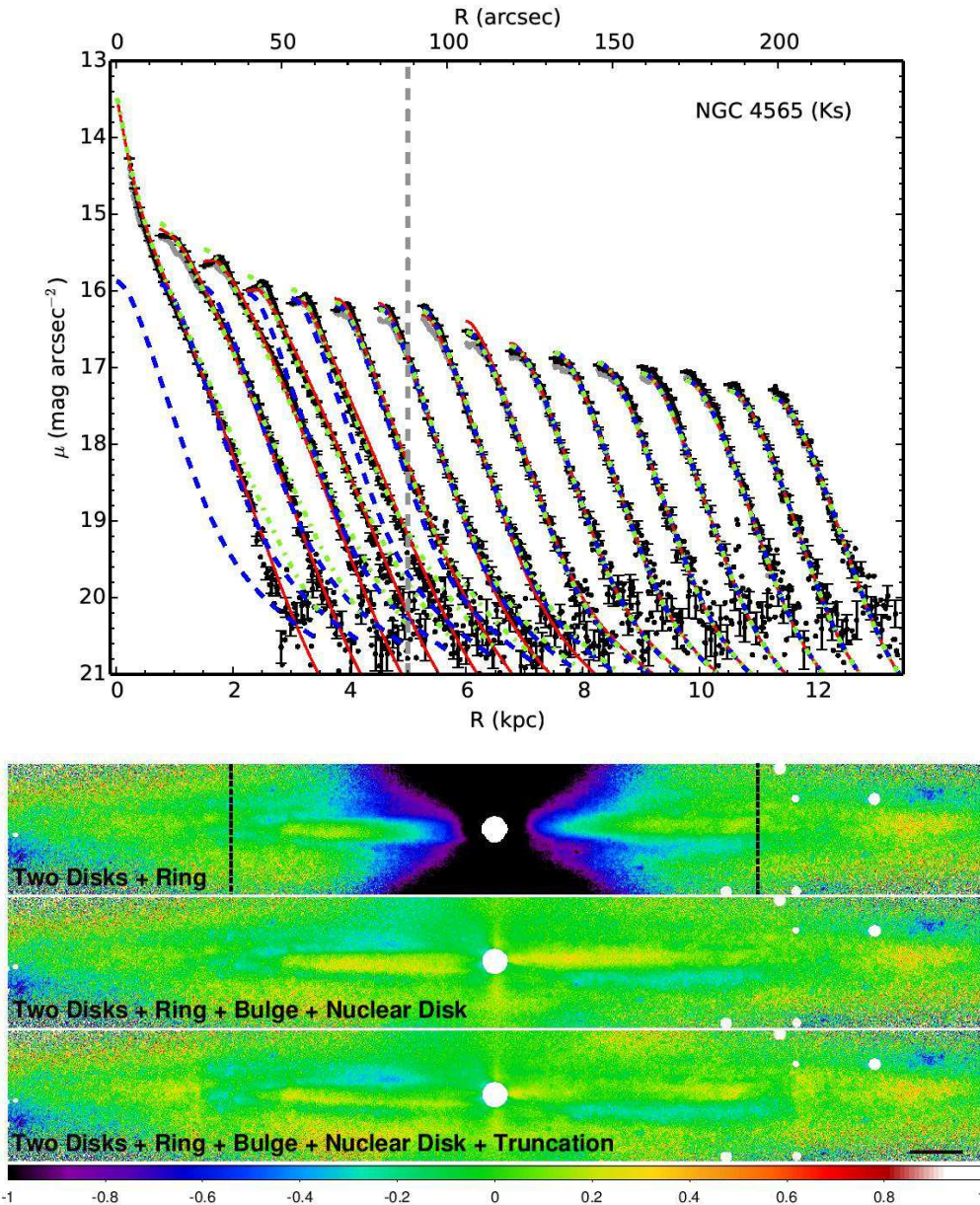


FIG. 23.— Similar to Figure 21, but for NGC 4565. Here the blue dashed lines show the best fitting two disk + ring model (the model shown in the left column of Table 5), fit to all regions outside of 5 kpc in radius (denoted by the vertical gray dashed line). The green dot-dashed lines show the best fitting two disk + ring + Sérsic bulge + nuclear disk model without a truncation (center column of Table 5), while the solid red lines show the best fit to that same model with an added disk truncation (right column of Table 5). To improve S/N the data in the 1D profiles have all been binned to  $5'' \times 0''.3$  ( $R \times z$ ).

$K_s$ -band luminosity compared to the super-thin disks of NGCs 891 and 4013.

#### 5.2.4. NGC 522

Comerón et al. (2011c) produce several one-dimensional fits of NGC 522, reporting thin and thick disk scale-heights of  $\sim 200$  and  $\sim 830$  pc, respectively. We begin by fitting our own version of that model, restricted to  $R > 4$  kpc. Based on a visual inspection of the surface brightness profiles (see Figure 24) the outer part of the disk appears to be truncated, and so based on our results for NGC 891 and 4013 we also include an outer truncation of the thinner disk. Due to the relatively small scale-height found

by Comerón et al. (2011c) for NGC 522’s thick disk, our data is sensitive enough that we do not have to fix this parameter in our fits (as we had done for previous galaxies). The results of this model are given in the left panel of Table 6 and shown as the blue dashed lines in Figure 24.

NGC 522’s surface-brightness profile is notable for several reasons. First, the outer disk truncation at  $\sim 13$  kpc in radius appears to be a downward break of the global radial surface brightness profile rather than a truncation of a single disk component, as seen in NGCs 891 and 4013. Modeling such breaks in the radial slope is beyond the scope of this paper. However, our simple outer truncation provides a better fit than a model with no trunca-

TABLE 6  
NGC 522 BEST-FITTING MODELS

Parameter <sup>a</sup>	Value			Units
	Two Disks <sup>b</sup>	Two Disks+Bulge <sup>c</sup>	Two Disks+Bulge+Bar <sup>c</sup>	
$\mu_{0,T}$	15.55±0.00	15.62±0.00	15.54±0.00	mag arcsec <sup>-2</sup>
$h_{R,T}$	7.93±0.08	10.00 <sup>d</sup>	7.66±0.07	kpc
$h_{z,T}$	0.38±0.00	0.41±0.00	0.38±0.00	kpc
$L_T$	$4.90 \times 10^{10}$	$4.71 \times 10^{10}$	$3.84 \times 10^{10}$	$L_{\odot,K}$
$\mu_{0,Th}$	18.01±0.03	18.01 <sup>e</sup>	18.01 <sup>e</sup>	mag arcsec <sup>-2</sup>
$h_{R,Th}$	9.55±0.16	9.55 <sup>e</sup>	9.55 <sup>e</sup>	kpc
$h_{z,Th}$	1.22±0.02	1.22 <sup>e</sup>	1.22 <sup>e</sup>	kpc
$L_{Th}$	$3.98 \times 10^{10}$	$3.94 \times 10^{10}$	$3.66 \times 10^{10}$	$L_{\odot,K}$
$\mu_{0,bar}$	...	...	16.23±0.01	mag arcsec <sup>-2</sup>
$h_{R,bar}$	...	...	5.00 <sup>d</sup>	kpc
$h_{z,bar}$	...	...	0.64±0.00	kpc
$L_{bar}$	...	...	$1.26 \times 10^{10}$	$L_{\odot,K}$
$\mu_{0,bulge}$	...	14.88±0.02	14.84±0.03	mag arcsec <sup>-2</sup>
$R_e$	...	1.10±0.01	1.09±0.01	kpc
$a/b$	...	1.45±0.01	1.57±0.01	kpc
$n^f$	...	1.30±0.01	1.39±0.02	kpc
$L_{bulge}$	...	$1.11 \times 10^{10}$	$9.03 \times 10^9$	$L_{\odot,K}$
$i$	88.49±0.02	88.49 <sup>e</sup>	88.49 <sup>e</sup>	degrees
$R_{trunc,1}^g$	...	1.25±0.03	4.45±0.05	kpc
$R_{trunc,2}^h$	13.18±0.03	13.18 <sup>e</sup>	13.18 <sup>e</sup>	kpc
$L_{tot}$	$8.88 \times 10^{10}$	$9.76 \times 10^{10}$	$9.66 \times 10^{10}$	$L_{\odot,K}$
$\chi_{\nu,inner}^2$	4.10	0.57	0.54	...
$\chi_{\nu,outer}^2$	0.65*	0.66	0.65	...
$\chi_{\nu,total}^2$	1.68	0.64*	0.61*	...

<sup>a</sup>  $T$ ,  $Th$ , and  $nuc$ , denote parameters that we associate with the thin disk, thick disk, and nuclear disk (respectively).

<sup>b</sup> Only fit to regions of the galaxy with  $R > 4$  kpc.

<sup>c</sup> Fit performed over entire radial range of data.

<sup>d</sup> Parameter minimized to the upper boundary of allowed parameter space.

<sup>e</sup> Fixed to Two Disks model value.

<sup>f</sup> Sérsic index.

<sup>g</sup> Inner truncation for the thin and thick disks, outer truncation for the bar.

<sup>h</sup> Outer truncation for the thin disk only.

<sup>i</sup> Reduced  $\chi^2$ . *inner* and *outer* correspond to the regions inside and outside of the 4 kpc fitting cutoff, while *total* is for both regions together. (\*) denotes the  $\chi_{\nu}^2$  that was minimized by each model.

tions (and will therefore result in more accurate luminosity estimates), so we continue to include this component in our other models.

NGC 522's disk is also quite flat in radius, with scale-lengths roughly 1.5-2 times as large as those found for the other fast rotators in our sample. This results in a scale-length to scale-height ratio of  $\sim 20$  for the thin disk, significantly larger than found in normal spirals (Bershady et al. 2010b). It appears that NGC 522 is an outlier in this regard, but note that our measurements may be biased because of the distance-dependence of our attenuation correction (Section 3.3.1). However, we would expect that correcting for this bias would tend to decrease both  $h_z$  and  $h_R$ , which could result in either a larger or smaller ratio of  $\frac{h_R}{h_z}$  depending on how exactly the data is biased.

We see no evidence for a super-thin disk component in NGC 522, although due to the uncertainty in our dust correction at this distance we reiterate that we may be insensitive to such a component. An inner disk truncation does appear to be warranted by the data, although it is not nearly as obvious as for NGC 891 or 4013. A visual inspection of Figure 1 shows a central morphology closer to that of NGC 4565 than the other fast rotators (chiefly in the lack of an obvious X-shape), so we choose to use a Sérsic bulge instead of a bar to model NGC 522's

inner light profile.

It is unclear whether or not a separate disk (akin to either the bar or nuclear disk components of NGCs 891, 4013, or 4565) inside of the truncation is needed in this galaxy, so we first fit a model without one (dot-dashed green lines in Figure 24 and the center column of Table 6). This model slightly overpredicts the central surface brightness between  $\sim 2$  and  $\sim 4$  kpc in radius. Including an inner disk produces an excellent fit in this region (solid red lines in Figure 24 and rightmost column of Table 6). The change in the residual structure appears less dramatic, and indeed the AIC value decreases by only 3%. This disk is quite extended, with  $h_z$  between the equivalent values found in the thin and thick disks. This result is generally consistent with what we fit for bar components in NGCs 891 and 4013, and therefore we adopt that nomenclature for this component.

We note, however, that NGC 522's bar is much more extended in the radial direction than in either NGC 891 or NGC 4013, and actually minimizes to the largest value allowed in our fit (5 kpc). It is possible that this is an indication that NGC 522's bar may be physically different than the bars we find in our other fast rotators, or possibly the conflation of two distinct morphological components. Regardless of the correct interpretation for this component, however, because it is truncated cleanly

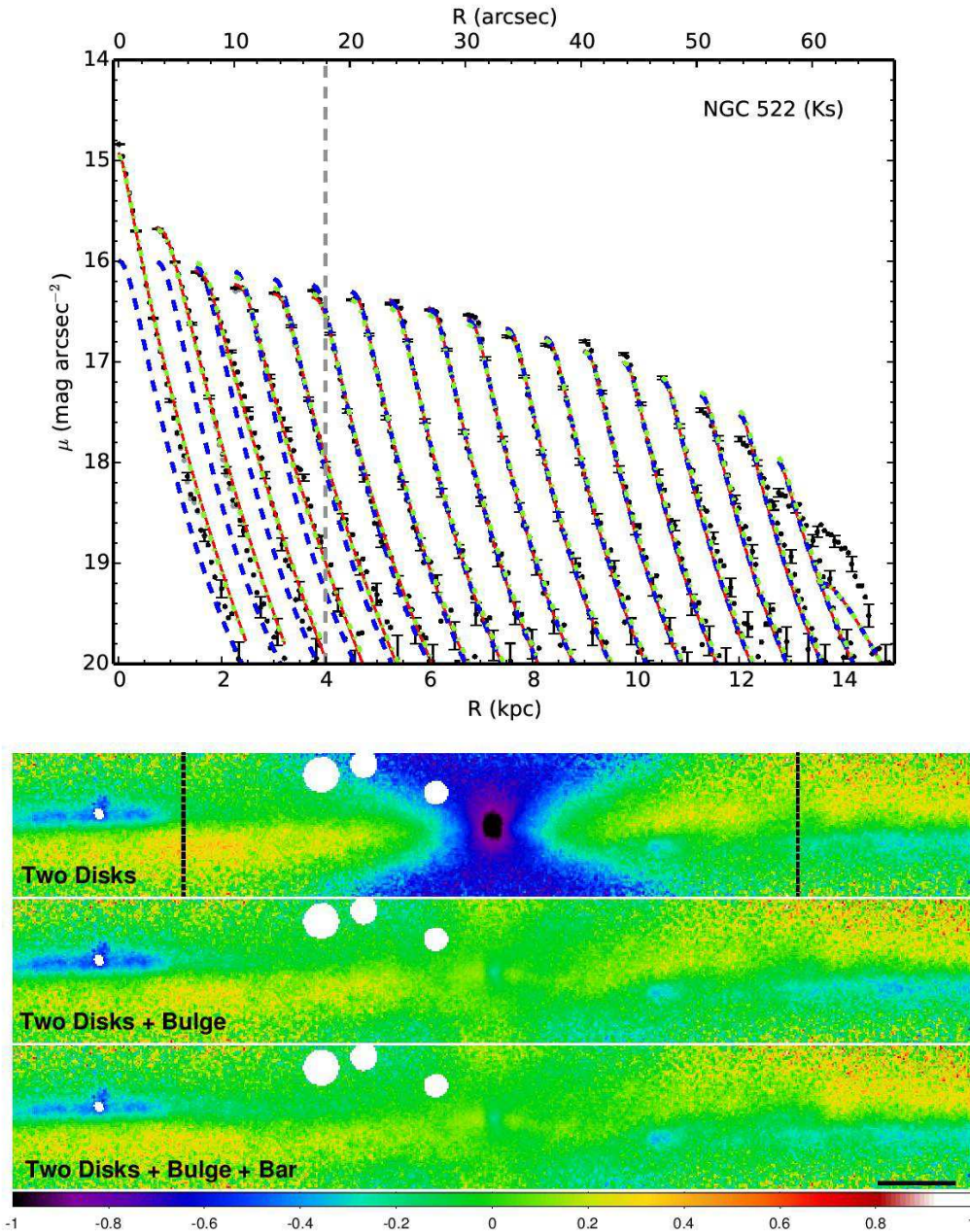


FIG. 24.— Similar to Figure 21, but for NGC 522. From left to right in Table 6: blue dashed lines (two disk model fit outside of 4 kpc), green dot-dashed lines (two disk model with Sérsic bulge), and red solid lines (two disk model with Sérsic bulge and exponential bar). To improve S/N the data in the 1D profiles have all been binned to  $1'' \times 0''.3$  ( $R \times z$ ).

at 4.45 kpc in radius it will have little effect on our estimation of this galaxy’s disk parameters (which are only present outside of this radius). Assuming it is directly comparable, this bar component is also much fainter (relative to the other components in the galaxy) than in NGCs 891 and 4013, which is a reasonable result given the comparative faintness of X-shaped bar features in NGC 522 (just barely visible in Figure 1).

#### 5.2.5. NGC 1055

NGC 1055 is morphologically very different from the other fast-rotators in our sample, notably in its bright, extended bulge (most visible in the SDSS image in Figure 1), but also in the large number of coherent dust

features visible away from the midplane. It is in a loose group with the extremely fast-rotating (HyperLEDA gives  $V_{rot} \sim 280 \text{ km sec}^{-1}$ ) spiral Messier 77, and a recent interaction between these two systems could explain the apparent disarray in NGC 1055’s disk.

While its unique features make it an especially interesting object to examine, they also conspire to make NGC 1055 tremendously difficult to model. Due to the expansive nature of the bulge, we must abandon our usual practice of first fitting just the disk components, and instead we are compelled to include a Sérsic bulge in all of our models and simultaneously constrain the bulge and disk parameters. Since we are no longer ignoring the bulge contribution for any models, we do not mask out

TABLE 7  
NGC 1055 BEST-FITTING MODELS

Parameter <sup>a</sup>	Value			Units
	One Disk <sup>b</sup>	Two Disks <sup>b</sup>	Two Disks+Truncated Disk <sup>b</sup>	
$\mu_{0,tr}^c$	...	...	15.49±0.01	mag arcsec <sup>-2</sup>
$h_{R,tr}^c$	...	...	3.38±0.09	kpc
$h_{z,tr}^c$	...	...	0.29±0.00	kpc
$L_{tr}^c$	...	...	$9.00 \times 10^9$	$L_{\odot,K}$
$\mu_{0,1}$	11.17±0.00	14.17±0.003	14.05±0.02	mag arcsec <sup>-2</sup>
$h_{R,1}$	1.80±0.00	1.45±0.003	1.60±0.01	kpc
$h_{z,1}$	0.01 <sup>d</sup>	0.19±0.001	0.10±0.00	kpc
$L_1$	$3.34 \times 10^{10}$	$3.23 \times 10^{10}$	$2.10 \times 10^{10}$	$L_{\odot,K}$
$\mu_{0,2}$	...	16.89±0.01	16.02±0.04	mag arcsec <sup>-2</sup>
$h_{R,2}$	...	2.82±0.01	10.00 <sup>e</sup>	kpc
$h_{z,2}$	...	1.26±0.00	0.15±0.01	kpc
$L_2$	...	$3.40 \times 10^{10}$	$3.20 \times 10^{10}$	$L_{\odot,K}$
$\mu_{0,bulge}$	12.48±0.01	8.32±0.02	10.38±0.05	mag arcsec <sup>-2</sup>
$R_e$	5.93±0.01	8.00 <sup>e</sup>	8.00 <sup>e</sup>	kpc
$a/b$	1.83±0.00	1.50±0.01	1.44±0.00	kpc
$n^f$	3.19±0.01	6.00 <sup>e</sup>	4.67±0.02	
$L_{bulge}$	$8.13 \times 10^{10}$	$3.94 \times 10^{10}$	$7.94 \times 10^{10}$	$L_{\odot,K}$
$i$	83.88±0.00	86.21±0.00	85.50±0.03	degrees
$R_{trunc,1}^g$	...	...	1.46±0.01	kpc
$R_{trunc,2}^g$	...	...	4.03±0.01	kpc
$L_{tot}$	$1.15 \times 10^{11}$	$1.06 \times 10^{11}$	$1.41 \times 10^{11}$	$L_{\odot,K}$
$\chi_{\nu,total}^2$ <sup>h</sup>	0.40	0.39	0.37	...

<sup>a</sup> *tr* denotes parameters that we associate with the truncated disk.

<sup>b</sup> Fit performed over regions of the galaxy with  $R < 6$  kpc.

<sup>c</sup> We call this disk the truncated disk rather than a super-thin disk, because it does not have a smaller scale-height than the nominal thin disk. See text for discussion.

<sup>d</sup> This parameter minimized to the lower boundary of the allowed parameter space.

<sup>e</sup> This parameter minimized to the upper boundary of the allowed parameter space.

<sup>f</sup> Sérsic index.

<sup>g</sup> Truncations are for the truncated disk only, where truncation 1 is the inner truncation and truncation 2 is the outer truncation.

<sup>h</sup> Reduced  $\chi^2$ . Since all models for NGC 1055 were fit over the same spatial regions, we only report the total  $\chi_{\nu}^2$ .

the central region of our data for any of our fits. Additionally, given the rapidly vanishing disk flux at larger radii we choose to fit our models only to regions with radius less than 6 kpc, as marked in Figure 13, which also avoids portions of the outer disk which likely have a substantial warp.

In all of our models there is a clear preference for a very large ( $R_e \gtrsim 6$  kpc) bulge, the quantitative consequence of the bright spheroidal component notably visible in the images. Our first model, consisting of a bulge and single disk, is listed in the leftmost column of Table 7 and shown with blue dashed lines in Figure 25. This model does a reasonable job fitting the data at small radii, but underpredicts the midplane surface brightness when  $2.5 \gtrsim R \gtrsim 4.5$  kpc and poorly matches the extended light at  $R \gtrsim 5$  kpc. This model predicts an extremely thin ( $h_z \lesssim 10$  pc) disk.

A model with a second disk (green dot-dashed line in Figure 25 and the middle column of Table 7) does a better job reproducing the data at large radii. Its thinnest disk has  $h_z = 190$  pc, much thicker than that of the single-disk model. The bulge parameters also change significantly with the addition of a second disk, with larger central surface brightness and effective radius. Despite these increases the total bulge luminosity actually *decreases*. This is due to the Sérsic index  $n$ , which doubles compared to its value in the single disk model – while the bulge has a brighter central surface brightness, the surface brightness decreases at a much faster rate, resulting

in a bulge that is fainter overall. The two disks have very different thicknesses, with  $\frac{h_{z,2}}{h_{z,1}} \sim 6$ . However, the total luminosity of the two disks is very similar, an unusual feature considering we generally find the thickest disk to be significantly fainter than the thinner component(s).

The only region in Figure 25 that is still poorly reproduced by the model with a bulge and two disks is near the midplane, around 3-4 kpc in radius. It is not immediately clear what is happening here; the excess only persists over  $\sim 2$  kpc, smaller than what we associate with a disk component in NGC 4013 and 891, but larger (and less peaked) than NGC 4565's ring. Additionally, if this excess is the sign of another disk, it would need to contain at least an outer truncation, but given how well the two disk model fits the midplane flux inside of 2 kpc this disk may also need to have an inner truncation. Indeed, when we add a third disk component we find the fit prefers having both inner and outer truncations of roughly 1.5 and 4 kpc, respectively. We list this model in the rightmost column of Table 7; it is represented as the red solid curves in Figure 25. This model still appears to underpredict the mid-plane surface-brightness and over-predict the light at large heights between radii of 2-5 kpc, which might indicate a thinner truncated component would be preferable.

While not perfect, this third model does a fairly good job fitting NGC 1055's entire light distribution. The AIC value for this model is 7% lower than our initial mode,

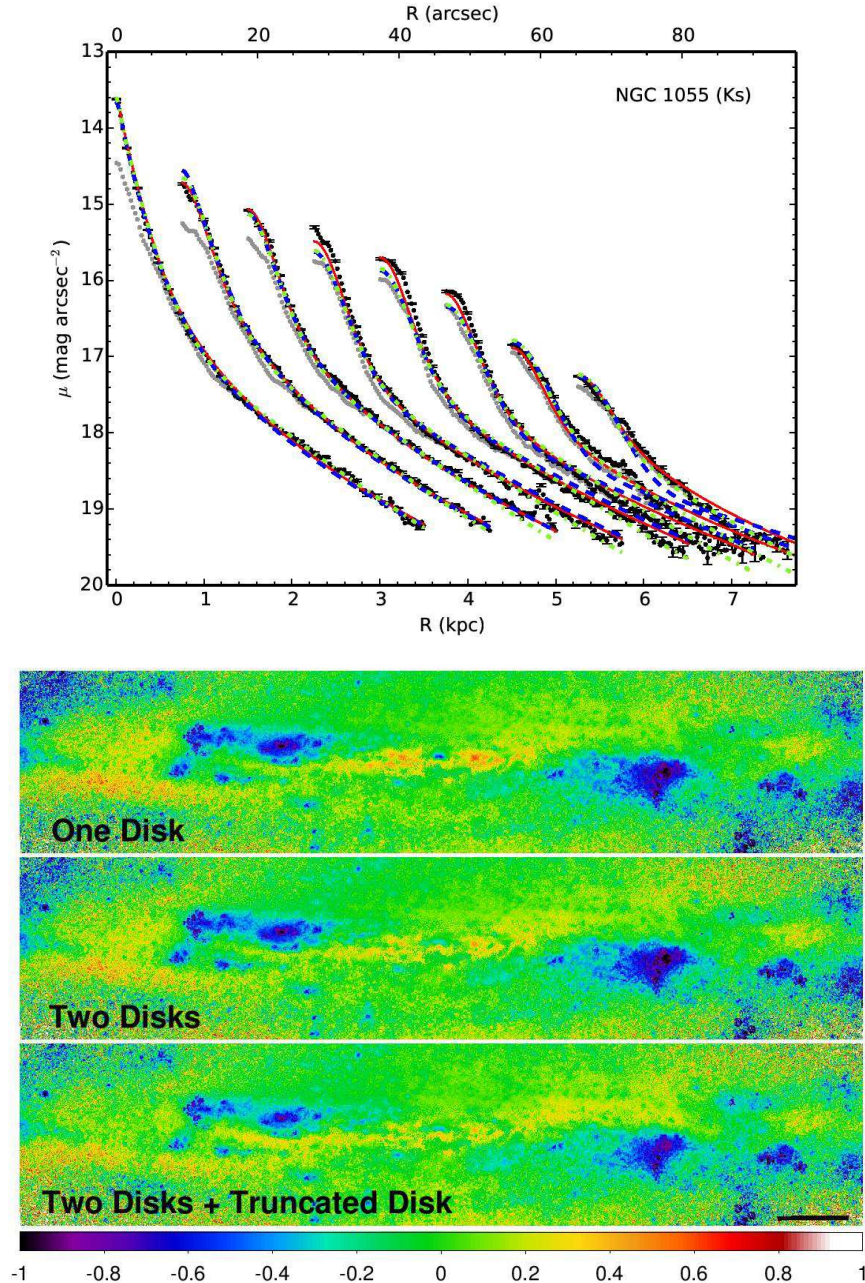


FIG. 25.— Similar to Figure 21, but for NGC 1055. Here we show the best fitting models with a Sérsic bulge and: one disk (blue dashed lines), two disks (green dot-dashed lines), and three disks with one containing inner and outer truncations (red solid lines). To improve S/N the data in the 1D profiles have all been binned to  $5'' \times 0''.3$  ( $R \times z$ ). Details of the model parameters are in Table 7.

and 4% lower than our second model. The scale-length of one of the disks minimizes to the upper boundary of our parameter space (10 kpc), but given the overall quality of the fit and the fact that increasing this parameter even more would have a minimal effect on the radial regions we are able to probe, increasing the range of our parameter space would have a negligible impact on our results. The bulge contains over 50% of the total  $K_s$ -band luminosity, comparable to the single disk model, and dominates the light profile along nearly every sight-line. This model is also notable for the sheer thinness of its disks. The doubly-truncated component, with scale-height only 290 pc, is at least twice as thick as the other

two disks. Despite the limits of our ability to model NGC 1055 given its disturbed morphology, the fits we can make all point strongly to the presence of significant amounts of starlight with  $h_z \lesssim 200$  pc.

#### 5.2.6. NGC 4244

Because this galaxy is essentially bulgeless (save for a small nuclear star cluster; Comerón et al. 2011a) we only need to mask out the innermost 1 kpc to avoid contamination. A single disk is the only component necessary to fit our NGC 4244 data outside of 1 kpc, as shown as the blue dashed lines in Figure 26 and detailed in the left column of Table 8. While there is currently an ongoing debate about whether NGC 4244 has a thick

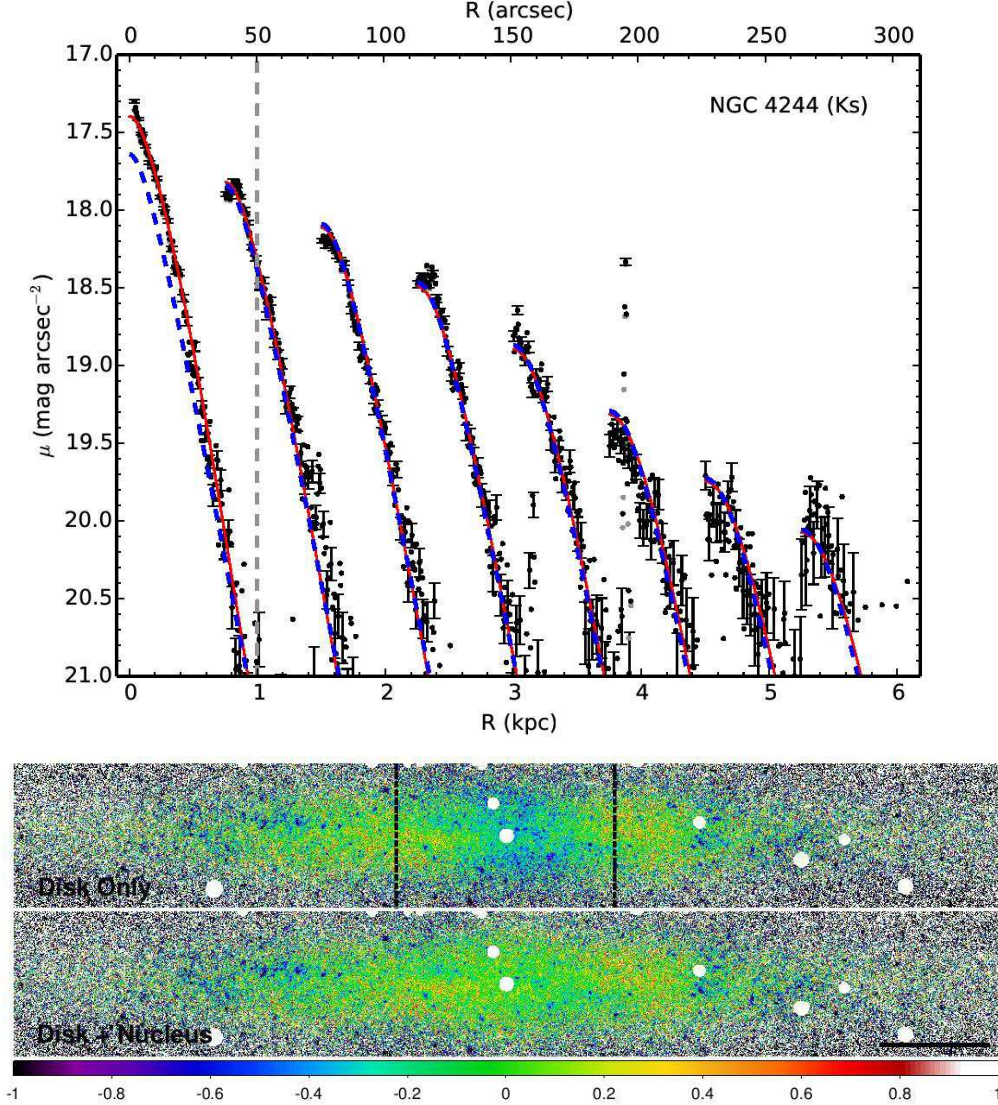


FIG. 26.— Similar to Figure 21, but for NGC 4244. The blue dashed lines show the best fitting single-disk model, fit to all regions outside of 1 kpc in radius (denoted by the vertical gray dashed line). The solid red lines show the best fitting single disk + Sérsic bulge model, which was fit at all radii. To improve S/N the data in the 1D profiles have all been binned to  $10'' \times 0''.3$  ( $R \times z$ ). Details of the model parameters are in Table 8.

disk (see Comerón et al. 2011a for a discussion), we note that our data is not sensitive enough to measure such a disk even if it does exist. Our best-fitting disk is almost identical to that found using optical data for NGC 4244 (Fry et al. 1999 and Seth et al. 2005), further evidence that NGC 4244 is nearly dust-free. Our fitted inclination falls between the literature measurements of Olling (1996) and Zschaechner et al. (2011).

We next re-fit NGC 4244, adding a Sérsic bulge model to the single disk to fit the nuclear star cluster. Because of the unresolved nature of the central star-cluster core and the PSF mismatch between IRAC and WHIRC images, the attenuation correction fails at the very center of NGC 4244. We therefore avoid fitting the inner 3.5 arcsec, or  $\sim 70$  pc in radius. Since the fitted nucleus has a half-light radius of 460 pc, the excluded light given the profile shape should only be  $\sim 2\%$  of the total luminosity of the nucleus component. The best-fitting model for these additional free parameters well-reproduces the

observed surface brightness distribution, and is shown alongside our initial model as red solid lines in Figure 26 and in the right column of Table 8; the AIC value for this is reduced from our initial model by about 3%. The resulting nucleus-to-disk luminosity ratio is 0.05, similar to that found in the optical (0.02, Fry et al. 1999).

### 5.2.7. NGC 4144

Modeling NGC 4144 is challenging because at large radii there is a clear asymmetry in the light distribution, visible both in our WHIRC and SDSS images (Figure 1). This asymmetry appears to increase at larger radii. Therefore we choose to perform our fits restricted to be within a projected radius of 2 kpc from the galaxy center. As it turns out, given the faintness of this galaxy there is little data outside this area that would add significant additional constraints on our models. Even with this restriction the disk appears to flare, with larger radii having flatter vertical profiles (Figure 27).

TABLE 8  
NGC 4244 BEST-FITTING MODELS

Parameter <sup>a</sup>	Value		Units
	Disk Only <sup>b</sup>	Disk+Nucleus <sup>c</sup>	
$\mu_{0,T}$	17.25±0.01	17.15±0.02	mag arcsec <sup>-2</sup>
$h_{R,T}$	1.80±0.01	1.84±0.01	kpc
$h_{z,T}$	0.25±0.00	0.23±0.00	kpc
$L_T$	$3.09 \times 10^9$	$3.19 \times 10^9$	$L_{\odot,K}$
$\mu_{0,nucleus}$	...	19.05±0.02	mag arcsec <sup>-2</sup>
$R_e$	...	0.46±0.00	kpc
$a/b$	...	1.21±0.02	kpc
$n^d$	...	0.53±0.02	kpc
$L_{nucleus}$	...	$1.59 \times 10^8$	$L_{\odot,K}$
$i$	86.53±0.05	85.81±0.10	degrees
$L_{tot}$	$3.09 \times 10^9$	$3.35 \times 10^9$	$L_{\odot,K}$
$\chi_{\nu,inner}^2$ <sup>e</sup>	2.44	2.17	...
$\chi_{\nu,outer}^2$ <sup>e</sup>	1.73*	1.73	...
$\chi_{\nu,total}^2$ <sup>e</sup>	1.86	1.81*	...

<sup>a</sup>  $T$  denotes parameters that we associate with the thin disk.

<sup>b</sup> Only fit to regions of the galaxy with  $R > 1$  kpc.

<sup>c</sup> Fit performed over entire radial range of data.

<sup>d</sup> Sérsic index.

<sup>e</sup> Reduced  $\chi^2$ . *inner* and *outer* correspond to the regions inside and outside of the 1 kpc fitting cutoff, while *total* is for both regions together. (\*) denotes the  $\chi_{\nu}^2$  that was minimized by each model.

TABLE 9  
NGC 4144 BEST-FITTING MODELS

Parameter <sup>a</sup>	Value		Units
	One Disk <sup>b</sup>	Disk+Bulge <sup>c</sup>	
$\mu_{0,T}$	17.78±0.01	19.28±0.01	mag arcsec <sup>-2</sup>
$h_{R,T}$	0.98±0.01	2.19±0.02	kpc
$h_{z,T}$	0.35±0.00	0.55±0.00	kpc
$L_T$	$1.45 \times 10^9$	$1.28 \times 10^9$	$L_{\odot,K}$
$\mu_{0,bulge}$	...	17.64±0.00	mag arcsec <sup>-2</sup>
$R_e$	...	1.07±0.01	kpc
$a/b$	...	3.54±0.01	kpc
$n^d$	...	0.90±0.00	kpc
$L_{bulge}$	...	$6.42 \times 10^8$	$L_{\odot,K}$
$i$	85.18±0.09	88.32±0.00	degrees
$L_{tot}$	$1.45 \times 10^9$	$1.92 \times 10^9$	$L_{\odot,K}$
$\chi_{\nu,inner}^2$ <sup>e</sup>	0.66	0.48	...
$\chi_{\nu,outer}^2$ <sup>e</sup>	0.48*	0.49	...
$\chi_{\nu,total}^2$ <sup>e</sup>	0.58	0.48*	...

<sup>a</sup>  $T$  denotes parameters that we associate with the thin disk.

<sup>b</sup> Only fit to regions of the galaxy with  $R > 1$  kpc.

<sup>c</sup> Fit performed over entire radial range of data.

<sup>d</sup> Sérsic index.

<sup>e</sup> Reduced  $\chi^2$ . *inner* and *outer* correspond to the regions inside and outside of the 1 kpc fitting cutoff, while *total* is for both regions together. (\*) denotes the  $\chi_{\nu}^2$  that was minimized by each model.

A single disk fit, restricted to the region between 1 and 2 kpc in radius and shown as the blue dashed lines in Figure 27 and the leftmost column of Table 9, does a generally poor job of fitting the data. At small radii this model underpredicts the light at small heights and overpredicts the light at large heights. Even at larger radii, where the model is directly constrained, it underpredicts the high-latitude light. The telltale flattening of the radial midplane profile we see in NGCs 891 and 4013 (e.g. the ridgeline of the profiles in Figure 22) does not exist here. This indicates that an inner disk truncation is not a viable solution.

Based on a visual inspection NGC 4144 does not appear to have a significant bulge component. Consequently, we next attempted to fit a two-disk model to the entire radial range of the galaxy. Such a fit results in low inclination ( $\sim 76^\circ$ ), a very thin inner disk ( $h_z = 30$  pc), and an exceptionally thick outer disk with  $h_R/h_z < 1$ . The two-disk model does an excellent job fitting the mid-plane light at small radii, but increasingly under-predicts the light near the mid-plane at larger radii. However, without any argument about the astrophysical plausibility of such an unusual disk, we can dismiss this model simply because it predicts far too much light at large scale-heights. For this reason we do not tabulate or plot the fit. Nonetheless, the model results are informative regarding limitation in modeling late-type, slow-rotating galaxies without well-defined mid-plane dust-lanes, as follows.

Literature values for NGC 4144's inclination (e.g., 82 degrees in Rhee & van Albada 1996 from LEDA, and 86.2 degrees from the current measurements in HyperLEDA, both based on optical axial ratios and assumed disk axial ratios) are comparable to what we found in our single-disk model, but are significantly higher than what we found in our two-disk model. Visual inspection of archival HST images<sup>14</sup> yields the impression that this galaxy could indeed be at an inclination in the range of 70 to 80 degrees, based on the intermittent ring of star-formation regions and patchy dust in the nuclear regions. However, without a clear morphological features such as a coherent, thin dust-lane, the impression is inconclusive. What is clear is that the thinness of the inner disk in the two-disk model is only possibly in a model at relatively low inclination. This reflects the inherent degeneracy between separating intrinsic oblateness from inclination angle.

Given the thickness of the second disk in the two-disk model, we next turned to a disk plus bulge model. We found a single disk and a Sérsic bulge were able to fit the data at all radii and heights (shown as the red solid line in Figure 27) better than the previous models, and with no failings. The AIC value for this model is 16% lower than for our initial model. The fitted parameters of this model are listed in the rightmost column of Table 9. The bulge is quite flattened ( $a/b=3.54$ ) and has a Sérsic index near unity, making it similar, but not identical to, an exponential disk with the same oblateness. While the bulge has a brighter central surface brightness, the disk component has twice the luminosity of the bulge due to its more extended light distribution.

Based on this two-component model, NGC 4144's disk has a fairly large scale-height of 550 pc, roughly twice that estimated from other studies in the near-infrared. For example, Seth et al. 2005 find a  $K_s$ -band scale-height of 228.5 pc, assuming an inclination of 83 degrees. This discrepancy could be due to contamination from the bulge component, which contains a substantial amount of the total  $K_s$ -band luminosity, but most likely reflects the degeneracy between inclination and disk oblateness noted above. For example, in our disk plus bulge model the best-fitting inclination is  $\sim 88$  degrees. We also note

<sup>14</sup> From the Hubble Legacy Archive at [http://hla.stsci.edu/cgi-bin/display?image=HST\\_9765\\_19\\_ACS\\_WFC\\_F814W%2F9765\\_19\\_ACS\\_WFC\\_F606W](http://hla.stsci.edu/cgi-bin/display?image=HST_9765_19_ACS_WFC_F814W%2F9765_19_ACS_WFC_F606W).



that some models fits with comparable  $\chi^2$  to our best-fitting model but have  $h_z \sim 100$  pc and inclinations closer to 81 degrees. We would caution against interpretation of disk scale-heights in this or other work until a better understanding of the three-dimensional geometry of this non-asymmetric galaxy is understood.

## 6. DISCUSSION

### 6.1. Attenuation Profiles

For the six galaxies analyzed in this work, an inspection of Figures 9 through 15 (excluding NGC 522) shows there is a clear distinction between the fast-rotating systems and the slow-rotators. The fast-rotators contain a fair amount of attenuation ( $\gtrsim 0.6$  mag near the mid-plane), while the two slow-rotating spirals have almost zero  $K_s$ -band attenuation. In Figure 28 we compare the vertical  $K_s$ -band attenuation profiles of our sample. The data have been scaled by the scale lengths and heights of what we call the ‘thin’ disk in our best-fitting models (the rightmost fits in Tables 3-9).<sup>15</sup> While not a perfect solution given the complexity of fitting some of these galaxies and the fact that most are not perfectly edge on, this scaling should allow for less biased comparisons than purely physical units like kpc, as previously shown in Figures 9 to 15.

Despite the rough distinction between fast and slow rotators, nearly every galaxy in Figure 28 has a visually distinct attenuation profile *shape*. To first order, this is an inclination effect. It is not a coincidence that the two nearly perfectly edge-on galaxies NGC 891 and 4013 both have centrally-peaked profiles with steep dropoffs from the midplane to nearly zero attenuation by  $1 h_{z,T}$ . Relative to NGC 4013, NGC 891 simply has more attenuation.

For slightly less inclined systems, NGC 4565’s more extended attenuation profile shows how much more transparent massive spiral galaxies become only  $\sim 3^\circ$  away from edge-on (see Figure 17 of Schechtman-Rook et al. 2012). NGC 4565 has only a couple of small regions with  $A_{K_s}^c \geq 0.5$  mag. Much of the dust in this galaxy appears to be concentrated in a narrow ring, clearly visible in Figure 11, and evident in the attenuation profile at  $0.1 h_R$ . This ring has been previously identified in molecular gas (Sofue & Nakai 1994) as well as in dust emission (Kormendy & Barentine 2010; de Looze et al. 2012). This dust morphology likely indicates NGC 4565 is not as similar to the other fast-rotators as would be assumed from the un-corrected images, and in fact it is the only galaxy in our sample that is known to have an active nucleus (e.g. Chiaberge et al. 2006). This activity may be responsible for the unusual *decrease* in attenuation at small radii near the mid-plane.

NGC 1055, in contrast, despite being at similar inclination as NGC 4565, has much more dust attenuation even though it has only half the neutral gas mass (cf. Thilker et al. 2007 and Dahlen et al. 2005). NGC 1055 also has more attenuation at larger heights than any of the other galaxies in our sample. Since we find both galaxies have similar inclination, NGC 1055’s extended

dust distribution is likely to be due to significant reservoirs of extraplanar dust and not merely the result of viewing this galaxy with  $i < 90^\circ$ . This is interesting because NGC 1055 also has disturbed morphology which may indicate recent interactions are the cause of this extended dust layer.

### 6.2. Vertical Color Gradients and Disk Heating

The evidence from our analysis is that most of the galaxies in our sample exhibit near-infrared ( $J - K_s$ ) color gradients in their vertical light profiles, and in some galaxies these vertical gradients change with radius. Color gradients encode information about changes in stellar populations. The existence of such gradients presents the question of how they arise and if, for example, the gradients support a picture of dynamical heating of the stellar disks. Correlation of these gradients with the multi-component disk structure is informative in this regard.

In general, color gradients are rather modest at large heights ( $z > 0.5$  kpc) in the fast rotators and at all heights in the slow rotators; colors in these regions *at a given height* are remarkably similar at all radii for any given galaxy. Distinguishing between age and metallicity is premature without further spectrophotometric diagnostics, but the smooth disk light distribution and the lack of radial structure at  $z > 0.5$  kpc in fast rotators (evident in Figures 9-12) suggests the stellar populations are dynamically relaxed, and hence old. Stellar population synthesis models indicate that metallicity is the primary driver of colors at these ages (Figure 17), but we cannot rule out a changing admixture of young and old populations with height.

At smaller heights the fast-rotator color gradients have much more structure, changing both with radius and between galaxies. Moving from large heights toward the mid-plane the gradients generally become steeper between  $0.2 \text{ kpc} < z < 0.5 \text{ kpc}$ , and then flatten at  $z < 0.2$  kpc, in some cases even getting bluer near the mid-plane (NGC 891 and 4565). The reddest colors tend to be found near  $z = 0.2$  kpc, which is a factor of two above our physical resolution limit even for NGC 522, our most distant source. The reddest colors in this region are quite high, with  $(J - K_s) > 1$ , which can only be matched in stellar population synthesis models with the presence of a large contribution from intermediate-age (0.2-2 Gyr) populations.

The two fast-rotating galaxies with super-thin disks (NGC 891 and 4013) also show the most dramatic changes in vertical gradients with radius. In both galaxies, the reddest colors near  $z = 0.2$  kpc are found in the inner regions ( $R < 3 \text{ kpc}$ ), where the disk components are truncated and their bars dominate the projected light. As a consequence of their very red colors at intermediate heights, these regions have the strongest gradients toward bluer colors at larger heights ( $z > 0.2$  kpc). The mid-plane colors never get bluer than  $(J - K_s) = 1$ , while the reddest colors are between  $1.2 < (J - K_s) < 1.4$ . These very red colors are indicative only of near-infrared star-light dominated by intermediate-age populations (see Section 4.1 and Figure 17). This suggests that the bars in these two galaxies are dynamically young and that their creation rapidly shut down star-formation in the inner regions. Bluer mid-plane colors, which fall

<sup>15</sup> There is one exception to this: due to the odd behavior of the two brightest disks in our most complex NGC 1055 model, we choose to use the scale-height of disk 1 from the two disk model instead.

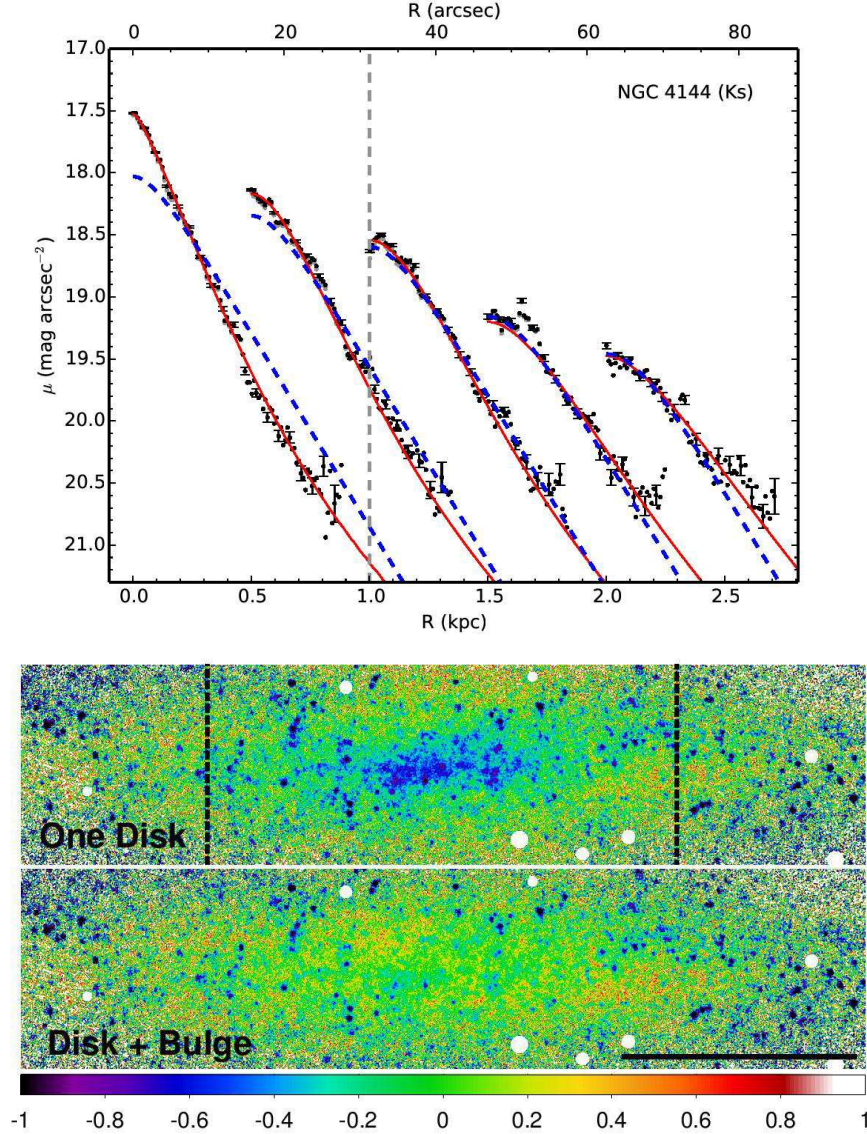


FIG. 27.— Similar to Figure 21, but for NGC 4144. The blue dashed lines show the best fitting single-disk model, fit to all regions outside of 1 kpc in radius (denoted by the vertical gray dashed line). The solid red lines show the best fitting single disk + Sérsic bulge model, which was fit at all radii. To improve S/N the data in the 1D profiles have all been binned to  $10'' \times 0''.3$  ( $R \times z$ ). Details of the model parameters are in Table 9.

TABLE 10  
LUMINOSITY DISTRIBUTION SUMMARY<sup>a</sup>

NGC	Super-thin Disk				Thin Disk				Thick Disk				%L				
	$\mu_0$	$h_R$	$h_z$	%L	$\mu_0$	$h_R$	$h_z$	%L	$\mu_0$	$h_R$	$h_z$	%L	Ring	Nuclear	Disk	Bar	Bulge
891	14.4	3.4	0.16	22	15.9	5.7	0.47	43	18.5	4.8	1.44	10	0	6	19	0	0
4013	14.5	2.3	0.21	26	16.0	2.8	0.60	28	19.0	4.0	2.96	14	0	3	29	0	0
4565	...	...	...	0	15.4	6.0	0.35	40	18.9	5.4	2.23	9	18	4	0	29	0
522	...	...	...	0	15.5	7.7	0.38	40	18.0	9.6	1.22	38	0	0	13	9	0
1055	14.0	1.6	0.10	15	16.0	10.0	0.15	23	15.5	3.4	0.29	6	0	0	0	56	0
4244	17.2	1.8	0.23	95	...	...	...	0	...	...	...	0	0	0	0	5	0
4144	...	...	...	0	19.3	2.2	0.55	67	...	...	...	0	0	0	0	33	0

<sup>a</sup> Surface brightness values ( $\mu_0$ ) are  $K_s$ -band mag arcsec<sup>-2</sup>, scale-lengths and scale-heights have units of kpc, and the luminosity percentage of each component (%L) is relative to the total modeled luminosity in the  $K_s$ -band. All models shown here can be found in the right-most columns of Tables 3-9. Disks for NGC 1055 are arranged in order of increasing  $h_z$ .

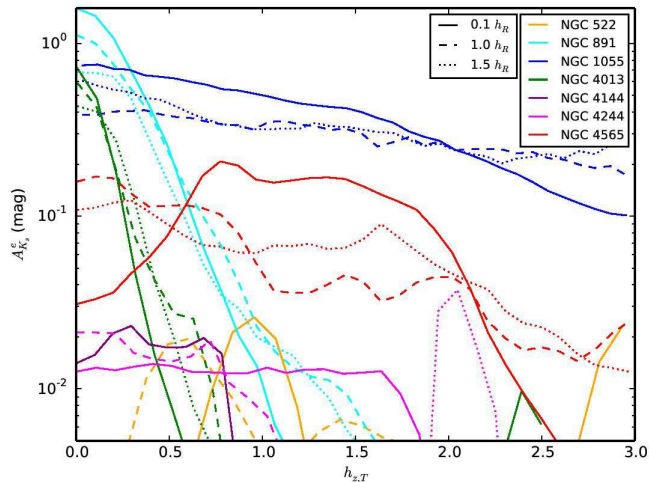


FIG. 28.— Projected vertical  $K_s$ -band attenuation profiles as a function of best-fitting thin disk scale-height. Profiles are shown at multiple thin disk scale-lengths to facilitate comparison between the galaxies.

below  $(J - K_s) = 1$  in NGC 891, are found in the radial region where super-thin disks are present in these galaxies, and indeed the gradients diminish above  $z = 0.2$  kpc.

For the fast-rotating galaxies without major super-thin components, we still note color gradients that correlate with their disk structure. The small, super-thin nuclear disk in NGC 4565 does appear to lead to bluer colors near the mid-plane at small radii. In NGC 522, vertical color gradients are largest at intermediate radii ( $6\text{kpc} < R < 8\text{kpc}$ ), where the thin disk contributes most to the total disk luminosity.

It is also interesting that the one exception to the discussion of vertical color gradients in fast-rotators is NGC 1055, which has disturbed morphology indicative of a recent or on-going interaction. It is well known that minor mergers heat disks in galaxy simulations (e.g., Walker et al. 1996). The clear lack of a vertical color gradient in this galaxy is consistent with this merger picture, in which any gradients that may have been present prior to the merger are removed from the mixing effects of the relatively more impulsive disk heating from a single merger event. The *absence* of a vertical color gradient in this galaxy is also verification that the *presence* of vertical color gradients in our other fast rotators are not artifacts of our attenuation correction. Despite the broader apparent vertical distribution of dust in this galaxy seen in Figure 28, due in part to its non-edge-on orientation and its disturbed morphology, there is a significant gradient in the attenuation with height. Indeed, the *uncorrected* colors do show a pronounced gradient (Figure 13). The lack of a thick disk component for this galaxy is somewhat puzzling in the context of a minor merger or interaction. We note the model degeneracy between disk thickness and inclination, discussed in the context of NGC 4144, may be an issue here as well, although for NGC 1055 there are good constraints on the thin inclination from the dust geometry. Overall, the disk system of this galaxy has near-infrared colors that are consistent with either a very metal rich stellar population or one dominated by intermediate-age stars. It may be that

the disk here is relatively young, having formed recently after a more major merger that produced or contributed to the significant bulge component.

The picture emerging from this discussion is that the disk structure parameterized in Section 5 does indeed correlate with, and offer insight on, the color gradients found in Section 4.1. The general behaviour is consistent with a dynamical heating model where the mid-plane is dominated by the youngest populations, intermediate age stars dominate the light at intermediate heights, while older stellar populations dominate at large heights. With additional spectrophotometric constraints it may be possible to use vertical gradients in stellar populations as chronometers of relatively recent dynamical heating of disks.

### 6.3. Disk Oblateness and Luminosity Ratios: Implications for Disk Maximality

To facilitate comparisons between galaxy disk structural parameters we gather together the surface-brightness, scale-lengths, scale-heights and relative  $K_s$ -band luminosity fractions from our best fitting models from Tables 3-9 in Table 10. The Table suggests rough definitions of a “super-thin disk” having  $h_z < 250\text{pc}$ , a “thin disk” having  $300 < h_z < 600\text{pc}$ , and a “thick disk” having  $h_z > 1\text{kpc}$  for this galaxy sample—not unreasonable in the context of the MW.

While the two slow rotators have very different distributions of light between their disk and bulge components, overall their total luminosities are fairly similar (within a factor of two). Unsurprisingly, the fast rotators are all at least 25 times more luminous than the slow rotators. These are all reflections of the well-known scaling relation between luminosity and rotation speed. NGC 1055 is especially interesting, as while it is one of the slower fast-rotators in our sample it has a luminosity more consistent with galaxies rotating  $\gtrsim 30\text{ km sec}^{-1}$  faster. This is largely due to the light contribution from NGC 1055’s prodigious bulge, which accounts for over 50% of the total  $K_s$ -band light in the galaxy.

All of the fast-rotating galaxies have multi-component disks. Excluding NGC 1055’s disturbed morphology, the other four (NGCs 891, 4013, 4565, and 522) show a general trend toward thicker components having larger scale lengths, but with *decreasing* axial ratios  $h_R/h_z$ . In other words, larger and thicker disks are less flattened. This may reflect the relative efficiency of disk heating in the radial and vertical dimensions. The conjecture could be tested by measuring the radial stellar velocity dispersion as a function of scale height either directly or through a dynamical proxy such as asymmetric drift between the tangential motion of gas and stars.

We focus now on just these four fast rotators since their disk structural parameters are likely most relevant to the DiskMass Survey calibration of  $h_R/h_z$  (Bershady et al. 2010b). The disk components in these galaxies, including nuclear disks and NGC 4565’s ring, contribute  $75 \pm 5$  (we quote mean and full range throughout this section) to their total  $K_s$  luminosity. Of this, the nuclear disks only contribute  $3 \pm 3\%$ .

We find  $h_R/h_z$  values of  $16_{-6}^{+5}$ ,  $13_{-9}^{+7}$ , and  $4_{-2}^{+4}$  for the super-thin, thin, and thick disks (respectively). In the context of the DMS, these values are still too small to im-

TABLE 11  
 INFRARED AB COLORS<sup>a</sup>

NGC	$L_K$ ( $10^{10} L_\odot$ )	$M_{\text{HI}}/L_K$ ( $M_\odot/L_\odot$ )	$K - m_{24}$	$K - m_{25}$	$K - m_{60}$	$m_{60} - m_{100}$
891	13.3	0.044	0.312	0.40	2.89	1.02
4013	8.80	0.049	...	-0.08	2.30	1.34
1055	14.1	0.040	...	0.57	2.89	1.11
4565	15.3	0.098	-0.86	-0.83	0.82	1.64
522	9.66	0.011	...	...	1.55	1.31
4244	0.335	0.31	-0.38	...	...	...
4144	0.192	0.25	-0.26	...	...	...

<sup>a</sup>  $L_K$  and  $f_K$  are the best-fitting model *total* luminosity and apparent flux (adopting distances in Table 1) in the  $K_s$  band from this study (see Tables 3 - 9). Remaining fluxes are from the literature (see text):  $m_{24}$  is the  $24\mu\text{m}$  magnitude measured using the Spitzer MIPS instrument;  $m_{25}$ ,  $m_{60}$ ,  $m_{100}$  are IRAS 25, 60 and  $100\mu\text{m}$  magnitude measurements, respectively.

ply maximal disks based on the observed, face-on stellar velocity dispersions (Bershady et al. 2011). Moreover, for the two disks with super-thin components (NGCs 891 and 4013), the thin and thick components have axial ratios  $h_R/h_z$  of  $6.5 \pm 2$ , and  $2.5 \pm 1$ . The small axial ratios for these two galaxies are a reflection of the increased oblateness of the *thin* components in the galaxies that are *without* super-thin components, which we discuss in the next section.

Thin disks contribute  $37_{-9}^{+4}\%$  to the total  $K_s$  luminosity while thick disks contribute  $18_{-8}^{+20}\%$ , so it is possible to characterize their contribution in luminosity roughly as  $L_T \sim 2L_{Th}$ . For the two galaxies that have super-thin disks (NGCs 891 and 4013), those components contribute  $24 \pm 2\%$  to the total  $K_s$  luminosity. This translates into roughly  $L_T + L_{Th} \sim 2L_{ST}$  for these systems.

#### 6.4. Presence of Super-Thin Disks

##### 6.4.1. Slow-Rotators

Given their well-known lack of narrow dust lanes (Dalcanton et al. 2004) and the correlation between dust and star formation (e.g. Boquien et al. 2011), it is perhaps unsurprising to find that NGC 4244 and 4144 have little-to-no evidence for the existence of a MW-like star-forming super-thin disk. However, NGC 4244’s disk is moderately thin in relative and absolute terms given its vertical scale height of 230 pc and oblateness ( $h_R/h_z = 8$ ). NGC 4144’s light profile is more complicated, but it seems clear that neither galaxy contains the nested super-thin+thin+thick disk structure we find in most of our fast-rotating galaxies. This does *not* mean that slow rotating galaxies cannot form very thin and flattened disks; UGC 7321 for instance, a member of the class of “super-thin” low-surface brightness disk galaxies, has a stellar disk scale-height of  $\sim 150$  pc but  $V_{rot} < 100$  km  $\text{sec}^{-1}$  and no distinct dust lane (Matthews 2000).

##### 6.4.2. Fast-Rotators

The results for all of the fast-rotators are phenomenologically richer than for their slow-rotating counterparts in this study. As we noted earlier, to first order the mass of the galaxy (its rotation speed) correlates with the number of distinct components required to model the light distribution. The distinct nature of the *model* components may or may not reflect distinct *physical* components, e.g., we could be approximating continuous distributions of age, metallicity and structural parameters.

However, this correlation hints at the increase in complexity we might expect to see in the hierarchical build-up of more massive systems that have assembled in a weakly-disruptive fashion, i.e., in a way such that they have remained dynamically cold by virtue of, say, the gas-richness or angular momentum alignment of their merging events. In this context the structural decomposition of these edge-on spiral galaxy light profiles reads like an archaeological record of their mass assembly and dynamical heating. We distinguish three groups, namely those with regular morphology and super-thin components, (NGC 891 and 4013), those with regular morphology but without super-thin components (NGC 4565 and 522), and those with disturbed morphology (NGC 1055). No doubt this grouping reflects the limited sample size of this study, but it still enables some conclusions to be drawn about the nature of super-thin disks in massive spiral galaxies.

Both NGC 891 and 4013 have similar relative luminosity in the super-thin disk components, but NGC 4013 has a thin disk that has half the flattening and two-thirds the relative luminosity as the thin disk for NGC 891. The “missing” thin disk luminosity can be accounted for if attributed to the prominently visible bar component of NGC 4013, which has a comparable total luminosity to the super-thin and thin disks. It is interesting to consider this in the context of the relative thickness of the disks in NGC 4013 and 891.

As mentioned previously, Comerón et al. (2011b) find that NGC 4013 has disks with unusually large  $h_z$ . Comerón et al. (2011b) choose to label their disks as “thin”, “thick”, and “extended”. However, given that we do not find any significant additional very thin component we designate the three disks as “super-thin”, “thin”, and “thick” (as outlined in Sections 5.2.2 and 6.3). Based on our best fits the scale-heights of NGC 4013’s two thinner disks are  $\sim 20\%$  larger than their apparent analogs in NGC 891; NGC 4013’s thickest disk is twice as vertically extended than its putative counterpart in NGC 891. NGC 4013’s disk oblateness is significantly decreased;  $h_R/h_z$  is roughly 2-3 times smaller than in NGC 891 for all three disks.

It is unclear why NGC 4013’s disks would be so much less oblate than other fast rotating spirals. Comerón et al. (2011c) find other galaxies with similar  $V_{rot}$  but disks with more “normal” thicknesses (e.g., PGC 013646). The ratios of disk luminosity to dynamical mass

within  $2.2h_R$  would argue in favor of NGC 4013 having a more maximal disk than NGC 891, assuming similar  $K_s$ -band mass-to-light ratios. All else being equal in the dynamical history of these disks, this would argue in favor of NGC 4013 having thinner disks. However, the process (particularly the sources) of disk heating is not a well understood phenomenon. Certainly the abundance of gas in this galaxy would be consistent with a quick reformation of a super-thin disk after some relatively minor merger (e.g., Puech et al. 2012), but the same could be said of NGC 891 as well. The telling difference between these two galaxies is the prodigious neutral hydrogen warp first detected by Bottema et al. (1987), and what appears to be an associated giant stellar tidal stream (Martínez-Delgado et al. 2009).

In an absolute sense, NGC 4013's thick disk scale-height of  $\sim 3$  kpc is larger than what can be produced in simulations of minor mergers (Kazantzidis et al. 2008). However, disks made through minor interactions tend to be flared at large radii (Villalobos & Helmi 2008), so it is possible that what we see in projection as a very thick disk is just the flared or warped outer portions of a thinner, inner disk. In contrast, Comerón et al. (2011b) advocate that a disk this thick must have formed at high redshift, when the galaxy was in the process of initial buildup and had elevated levels of gas turbulence and heating via giant star-forming clouds. This is consistent with the apparent ubiquity of thick disks at high redshift, e.g., Elmegreen & Elmegreen (2006) and Förster Schreiber et al. (2009), but it would imply such thick disks should be fairly more common in the local universe, while Comerón et al. (2011b) report only 2 in 46 of their galaxies contain such a thick disk. Therefore in addition they suggest the disk of NGC 4013 must have been further heated by a single, significant merger event. This would require fine-tuning of the merger event since, for example, simulations following multiple minor mergers fail to produce such thick disks (Kazantzidis et al. 2008). As dramatic as the giant stellar tidal stream found by Martínez-Delgado et al. (2009) appears, they estimate the progenitor merger object was relatively low mass ( $6 \times 10^8 M_\odot$ ).

An alternative and perhaps simpler explanation is that the thickness of the disks in NGC 4013 is a projection effect of a warp in the stellar disk seen clearly in the gas disk. If the warp were oriented as the HI, we would expect to see the asymmetry in the vertical light profile. Such an asymmetry is not apparent in our residual images (Figure 22), but a more complicated, pretzel-like distribution of luminosity at lower surface-brightness at much larger radii is clearly visible in the deep optical images of Martínez-Delgado et al. (2009). This morphology may be consistent with the HI flare, but clearly there is additional structure in what appears to be tidal streams. If the apparent thick disks seen in any galaxy are due to warps or flaring, it may be possible to probe this condition with integral-field spectroscopy assuming the systems is dynamically stable. In this case, the off-plane line-of-sight velocity distribution function would be skewed increasingly toward lower tangential velocities at larger heights since an increasing fraction of the stars would be situated away from the tangent point. Changing dust attenuation over the height and radius of the disk would complicate such a measurement, however, and

would need to be carefully controlled for by any future investigations along these lines.

While the thickness of NGC 4013's disk components is difficult to explain unless they are the projection of a warp or tidal disturbance, the galaxy still requires three nested disks to fit its integrated light profile like in NGC 891 or the MW. The remaining three fast-rotating galaxies in our sample present further complexity. While the two disks necessary to fit the data for NGC 4565 closely resemble the thin and thick disks of the MW and NGC 891 in terms of scale-heights and total luminosities, we see no strong evidence for a super-thin component—even the stellar emission associated with the CO-rich ring has  $h_z \sim 300$  pc. Given that this galaxy is only slightly ( $\sim 20\%$ ) farther away than NGC 891, and that we recover components with  $h_z \leq 200$  pc in galaxies even more distant than NGC 4565, this is not a resolution issue. It's possible that, while outwardly similar to the MW and NGC 891, NGC 4565 is just not forming many new stars. The minimal amounts of extraplanar dust (Howk & Savage 1999, unlike in NGCs 4013 and 891; see Rueff et al. 2013; Howk & Savage 1997) would corroborate this argument.

The need for a ring to fit NGC 4565's light profile is also unusual, insofar in that none of the other six galaxies in this work required such a component. Buta (1990) notes that prominent rings are preferentially observed in early-type disk galaxies. While both NGC 891 and NGC 4565 are classified as Sb in HyperLEDA, given that NGC 4565's central light concentration is better fit with a bulge model, it could actually be an earlier type. Another possibility is that this feature is a pseudo-ring caused by the projection of the bar or the spiral arms, which Buta (1990) indicates is more common for later-type spirals.

Like NGC 4565, NGC 522 also does not appear to require a super-thin disk. Given its large distance we have noted our concerns for the accuracy of the attenuation-corrected vertical profile. The lower physical resolution we have for this galaxy would tend to reduce the contrast in the correction between regions of high and low attenuation when these regions are spatially proximate and unresolved, as we would expect near the disk mid-plane. However, the disk structural parameters for these two galaxies are remarkably similar. In particular, their thin-disk components are nearly identical in size and thickness, and both contribute 40% to the total  $K_s$ -band luminosity, comparable to NGC 891's thin-disk but twice as flat in terms of  $h_R/h_z$ . (Their thin-disk oblateness is comparable to the super-thin oblateness of NGC 891 and 4013.) Their thick disks are also not dissimilar to that of NGC 891, although NGC 522 stands out at having the largest thick-disk luminosity (and scale-length) in both absolute and relative terms. What also differentiates both NGC 4565 and NGC 522 from NGC 891 and 4013 is the diminished strength of nuclear disks, and stronger bulge versus bar components. One might speculate that nuclear and super-thin disks are both manifestations of relatively recent gas accretion. The distinction between bulge and bar seems less clear, particularly given the low Sérsic indices we find ( $n \sim 1$ ) for these systems, with axial ratios not very different from those of the bars in NGC 891 and 4013.

Finally, while NGC 1055 is not directly comparable to any of the more isolated fast rotators we have studied,

it is interesting to note that despite clear signs of interaction and containing a bulge component more luminous than any disk by a factor of  $>2$ , this galaxy manages to have disk components with scale-height  $<200$  pc. In fact, roughly 38% of its total  $K_s$ -band luminosity is in such super-thin components, and all of the disk components have scale-heights below 300 pc. Either the very thin disks are sufficiently self-gravitating or gas-rich and dissipative to be robust against tidal disruption, or they have reformed rapidly. The large amount of attenuation in this galaxy indicates the presence of abundant HI (estimated at  $10^{9.56} M_\odot$  by Thilker et al. 2007).

#### 6.4.3. Infrared Colors as a Diagnostic

An exasperating outcome of our modeling is the roughly even split between fast-rotating spirals with and without super-thin *stellar* disks that appear, based on their optical and near-infrared images and colors, to be rather similar. Only with attenuation corrected high angular resolution near-infrared images and 2D profile fitting is the presence of the super-thin components revealed. This is rather unsatisfactory, particularly in the context of dynamical studies of galaxies that are not viewed edge-on, such as the DiskMass Survey.

However, with the supposition that the super-thin disks are star-forming regions, it is reasonable to expect that either a *large* gas to stellar mass ratio or a *small* near to mid/far-infrared luminosity ratio would indicate the presence of a super-thin disk. To test this hypothesis we have compiled our total  $K_s$ -band model luminosities along with literature values for atomic hydrogen mass from HyperLEDA, as well as Spitzer and IRAS mid- and far-infrared luminosities from NED<sup>16</sup> in Table 11. Colors are in the AB system. Wherever possible we used the IRAS values from Sanders et al. (2003). Unfortunately, molecular gas-mass estimates remain surprisingly hard to come by in the literature or in on-line databases, but we note the correlation between mid-IR  $24\mu\text{m}$  and CO fluxes used by Westfall et al. (2011) based on data in Leroy et al. (2008).

Inspection of the tabulated colors indicates that the atomic gas to stellar mass ratio (technically,  $M_{HI}/L_K$ ) is *not* a good diagnostic of the presence of a super-thin disk, most likely because atomic gas is a necessary but not sufficient condition for star-formation. In contrast, the near- to mid/far-infrared colors *do* seem to correlate with the presence of a super-thin disk in the expected sense that a relative enhancement of mid- and far-infrared flux (from dust warmed by star-formation) accompanies the presence of a super-thin stellar disk. Further corroborating this astrophysical picture is the indication that the 60 to  $100\mu\text{m}$  color appears to be slightly enhanced when the near- to mid/far-infrared is depressed, i.e., when there is more dust emission per unit stellar emissivity, the dust emission appears to be somewhat warmer. As best we can reckon given our limited statistics and extant literature data,  $K - m_{60} > 1.86_{-0.31}^{+0.44}$  is the threshold for the presence of a significant super-thin disk component in fast-rotating spiral galaxies.

#### 6.5. Face-on Profiles of Truncated Galaxies

The model fits for the slow rotating galaxies in our sample contain disk components that do not require radial truncations. From this fact we can infer these galaxies should have a classical Type I face-on radial surface brightness profiles (Freeman 1970). We have confirmed this by re-projecting the models to a face-on orientation and plotting them in the left panel of Figure 29). It is also clear from inspection of Table 10 that these slow-rotating disks have central disk surface-brightness 4 to 10 times lower than that of a Freeman disk (Freeman 1970) which would have  $\mu_0(K) = 18.15 \pm 0.5$  for colors in the plausible range of  $3 < (B - K) < 4$ .

The necessity of an inner disk truncation for our fast rotators indicates that these galaxies may have more complex face-on light distributions. Of interest is the possibility that the inner disk truncation may give rise to Freeman Type II profiles, where there is an apparent down-turn of the light profile at intermediate radius where the dominance of the disk and bulge (and/or bar) transitions. Using an inner disk truncation to produce Type II profiles has been employed by Kormendy (1977) and Baggett et al. (1998). The application here is different because our analysis is based on fitting the edge-on light distributions where the radial truncation, if it exists, is seen in projection. However, by virtue of this projection we are able to capture the vertical dependence of disk truncation as we have done in the preceding sections. Specifically, the truncation radii of different thickness disk components are not always the same.

The right panel of Figure 29 shows the face-on radial profiles predicted by our models of NGCs 891, 4013, 4565, 522, and 1055. These disks all have central surface brightness values within a factor of 2 of the Freeman value, much brighter than the slow-rotators. Since the truncations we used in our models are abrupt in radius they produce unrealistic discontinuities in the face-on profiles. (In projection to edge-on this abruptness is naturally smoothed.) We therefore convolve the regions within 1.0 kpc of any truncations using a uniform kernel of 0.25 kpc. To ensure continuity, points near the edges of the smoothed region are constructed of a weighted average between the smoothed and unsmoothed profiles, with more weight being given to the unsmoothed data closer to the edge of the smoothing region. We use the Meijer G functional form described by Baes & Gentile (2011) to reproject our fitted bulges.

Two of the five galaxies exhibit light profile morphology that would clearly be classified as Type II (inner break). NGC 4013 and 522 show dips in their light profile around their innermost truncations near 3 kpc and 4.5 kpc respectively. NGC 891's inner truncation is less obvious, although it too produces a lower-amplitude break near 2.7 kpc where its disks truncate; it might also be classified as a Type II profile. NGC 4565 is more difficult to identify, largely due to the bump at  $R \sim 5.5$  kpc caused by its ring. If the flux excess caused by the ring was considered to be small-scale structure and masked from the fit (as is often done, e.g. Baggett et al. 1998) NGC 4565 would almost certainly be classified as having a Type I profile. Despite its disturbed morphology NGC 1055's face-on appearance is that of a Type I spiral, although the outer truncation in the profile is clearly visible (around 4 kpc). Our results suggest that inner Type II profiles are at least sometimes caused by truncations

<sup>16</sup> <http://nedwww.ipac.caltech.edu/>.

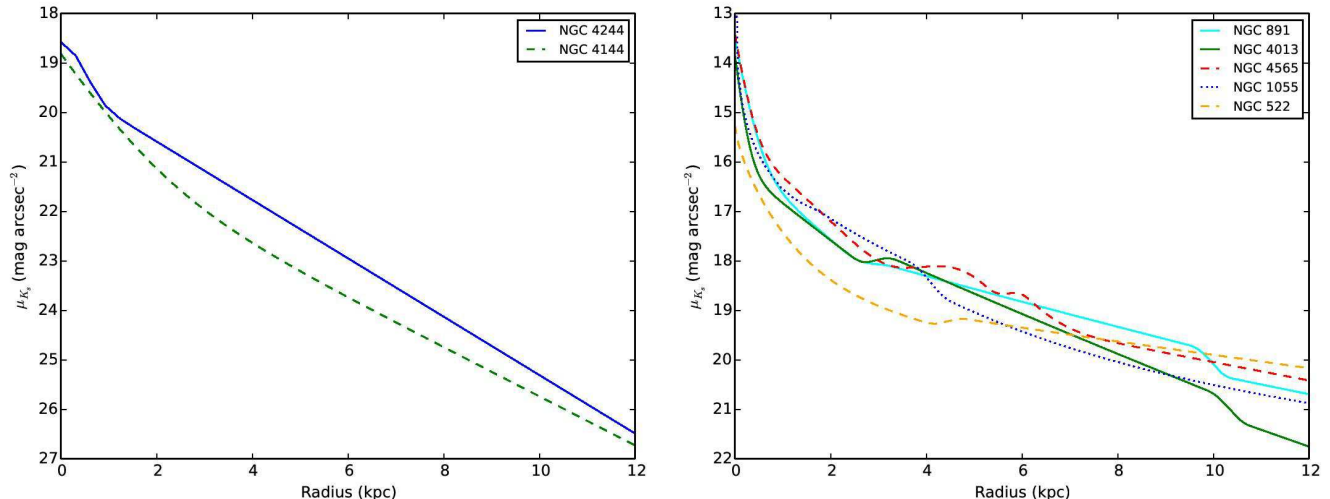


FIG. 29.— Predicted face-on radial surface brightness profiles for the galaxies in our sample. Left: slow rotators. Right: fast rotators. The line styles of the fast rotators correspond to galaxies with super-thin disks (solid lines), galaxies without (dashed lines), and galaxies with disturbed morphologies (dotted lines).

in the disk luminosity distributions.

## 7. SUMMARY

We have expanded our study of the intrinsic NIR light distribution of spiral galaxies, begun in Paper 1 for NGC 891, to a sample of seven spiral galaxies at a variety of rotation speeds ranging from 69 to 245 km s<sup>-1</sup>. This work makes advances in three broad areas. First, on a technical level, we have generalized our method for estimating and correcting for dust attenuation in the near-infrared. This method is now applicable to a wide range of dust morphologies, and requires no assumptions about the intrinsic infrared colors of stellar populations. We have also dramatically increased the complexity of our model two-dimensional light-profiles, and the dynamic range over which we can probe model parameters. Second, on a descriptive level, we have characterized the multiplicity of disk structure, and the trends this multiplicity exhibits with rotation speed—at least within the limitations of the present sample. Third, we have found a correlation between disk structure, as manifest in our modeling, and the attenuation-corrected NIR color gradients in height and radius. This correlation points to an astrophysical explanation for the origins of this structure in disk heating.

At a technical level, we continue to utilize 3D radiative transfer models to estimate the attenuation due to dust (both emission and absorption), and in this work we further develop these models for a more realistic representation of the dust and stellar distributions in slower-rotating spirals. To compute the attenuation accurately for the entire sample we also improved upon the correction scheme of Paper 1, where we assumed a constant color of  $(K_s - 4.5\mu\text{m}) = 0$  for the unattenuated star-light. While this is a suitable approximation for NGC 891, in this study we find that sample galaxies have a small but non-negligible range of IR colors ( $-0.1 < (K_s - 4.5\mu\text{m}) < 0.5$ ) in regions where there is little dust attenuation.

In this study we incorporate SSP models with our estimated *differential* attenuation in the  $J, H, K_s, 3.6\mu\text{m}$  and  $4.5\mu\text{m}$  bands, simultaneously constraining the age,

metallicity, and attenuation for every binned pixel. To produce accurate attenuation corrections in regions of low S/N, we employed adaptive binning based on the Voronoi tessellation. While the estimates of age and metallicity are uncertain and quite degenerate, our purpose here has been to estimate the attenuation, which we find is *not* particularly covariant with other model parameters that produce suitably good fits to the multi-band data. Specifically, we estimate the accuracy of our attenuation corrections is 0.1 mag in the  $K_s$  band; comparable accuracy is achieved for the color excess  $E(J - K_s)$  for  $A_{K_s}^e < 0.5$  mag. This enables us to construct reliable two-dimensional NIR surface-brightness and color profiles.

We have fit two-dimensional models of galaxy light profiles to our attenuation-corrected images using an improved Levenberg-Marquardt minimization algorithm that increases flexibility relative to our previous application in Paper 1. In the current analysis we are able to fit a broader variety of analytic functions (including rings and generalized Sérsic profiles), as well as inclination. The increased sophistication of the models was required in order to accurately reproduce the features clearly seen in the attenuation-corrected galaxies, and to account for the fact that few of the galaxies in our sample are perfectly edge on. The need for additional model complexity is illustrated in one-dimensional comparison of surface-bright profiles and two-dimensional residual maps. These visual assessments are corroborated and quantified by significant decreases in  $\chi^2$  values with additional model parameters. In all cases, the presence of non-axisymmetric structure in the observed galaxies light distributions results in significant residuals with respect to even our most complex, but always axisymmetric, models. The non-axisymmetric residuals ultimately limit our ability to reliably constrain additional model complexity. For the galaxies analyzed in this study we appear to be above this limit, but approaching it for the three cases of NGC 522, NGC 1055, and NGC 4244.

We obtained dramatic increases in computational power by optimizing our software to use local, distributed

computing resources. This was critical for enabling us to probe a wider range of models, thereby increasing the robustness of our conclusions since we could fully explore some of the inherent degeneracies in our parameters (e.g., disk oblateness and inclination for NGC 4144). With the exception of NGC 4144, inclination is well constrained in our models, and the remaining model parameters for disk scale-length, height, and luminosity are also well constrained even in the context of three-component disks.

At a descriptive level we find that in such a detailed examination all the galaxies in our sample have unique qualities. Even arguably the two most similar galaxies, NGCs 891 and 4013, have fairly different scale-heights and bar-to-disk luminosity ratios. A general trend is the need for fewer structural components to accurately model slow rotating spirals (lower-mass disks are simpler).

In fast rotators the most common features seem to be the presence of inner disk truncations. The commonality of these truncations may be a key to understanding why some face-on spiral galaxies appear to have inner breaks in their radial profiles. When reprojected to a face-on projection, our best-fitting models for several of our fast rotating galaxies yield radial surface-brightness profiles with breaks similar to classic Type-II morphology (Freeman 1970). Whether or not the bars in these instances act to *radially* redistribute stars to produce the break, it is clear they are responsible for redistributing the stars into a thicker *vertical* distribution at small radii ( $< 1h_R$ ).

Our slow rotators both have Type-I profiles and appear to be without bars, from which we conclude that Magellanic irregulars are absent from our sample; their disks generally appear to have  $h_z$  comparable to the thin disks in fast rotating spirals. With the exception of NGC 4144, the vertical disk structure is well constrained or all galaxies in our sample, with systematic errors in inclination below 1 deg for all galaxies in our sample exception for NGC 4144. Given the lack of well-defined, thin dust-lane and apparent irregularity in the star light for NGC 4144, the inclination estimate is highly covariant with scale-height. We caution that estimates of NGC 4144’s disk scale height here or in the literature are highly uncertain (to within factors of 5).

Roughly half of our sample of fast-rotating disks contain a super-thin ( $h_z < 250$  pc) disk component. This demonstrates that super-thin disks are not ubiquitously significant components of massive, star-forming spiral galaxies, but they are common. It also serves to confirm that NGC 891 and the MW are not alone in their nested multi-component disk structure, in which thinner disk components are also radially smaller. In particular, NGC 4013 appears to have super-thin, thin and thick components with similar luminosity ratios to NGC 891.

However, each of NGC 4013’s disks are more oblate than their putative counterparts in NGC 891, being both thicker and radially shorter. The extreme thickness of NGC 4013’s thickest disk is quite difficult to explain in the theoretical paradigm of disk heating through minor mergers; this is either a clue that the nested disk structure we see in our own galaxy may arise from a variety of merger histories or alternatively that the decreased oblateness of NGC 4013’s disks are due to projection of a warp in the stellar disk seen clearly in the neutral gas. Given the giant, stellar tidal stream known to exist in

this system, apparently due to a low-mass progenitor, a third alternative is that our theoretical understanding of disk heating from minor mergers is incomplete. As a further example, NGC 1055 also has super-thin disk components; what is unusual about this galaxy is its disturbed morphology and pronounced lack of a *thick* disk. While the complexity of its light distribution precludes a definitive characterization of its intrinsic disk structure, our results indicate very thin disks may survive or be able to reform efficiently after merger events in gas rich systems (e.g. Hopkins et al. 2009).

Neither apparent optical and near-infrared morphology or gas richness of galaxies in our sample provide a good predictor of a super-thin disk component. For example, despite frequently being named as a good analog to the MW (e.g. van der Kruit 1984; Shaw & Gilmore 1989; Jones 1989), no super-thin component is necessary to fit NGC 4565’s vertical light profile. However, for the fast rotators, we do find that an enhancement of mid- and far-infrared flux relative to the  $K_s$  band does correlate with the presence of a super-thin disk component. This is consistent with super-thin disks being associated with young stellar populations and star-formation. In future work we intend to use this criterion to estimate the statistical frequency of super-thin disks using larger galaxy samples, and also apply this result to the DiskMass Survey for an improved dynamical analysis.

The two fast-rotating galaxies without super-thin disks (NGCs 4565 and 522) do have the thinnest and most oblate “thin” disk components, which may be indicative of recent, but perhaps not on-going (or vigorous) star-formation. NGC 4565 is known to be one of the few massive galaxies with little extraplanar dust, a feature which usually signifies outflows from young, massive stars (Howk & Savage 1999). A ring-like *stellar* feature with a radius of  $\sim 4.5$  kpc is clearly seen in NGC 4565 from even a cursory visual inspection of the attenuation-corrected NIR image; the ring has a thickness comparable to that of NGC 4565’s thin disk. NGC 4565 is the only galaxy in our sample requiring such a feature. It is also the only galaxy in our sample with a known active nucleus, which plausibly may be responsible for the relatively diminished current star-formation and absence of a super-thin disk.

With the exception of the one morphologically disturbed galaxy in our sample (NGC 1055), all show distinctive, attenuation-corrected near-infrared ( $J - K_s$ ) color gradients with height above their mid-planes. The trends are significant with respect to our estimated systematic errors, and correlate with the independently estimated disk components, e.g., super-thin, thin, etc. The general trends are to bluer  $J - K_s$  colors at larger heights, which could reflect both gradients in age and metallicity. Our fast rotating galaxies have strong color gradients at small heights, with  $J - K_s$  increasing by 0.2-0.4 mag from the high-latitude value of  $\sim 1$ , and peaking near  $z \sim 0.2$  kpc. These near-mid-plane colors imply the existence of a significant population of intermediate-age AGB (carbon) stars. In some galaxies, notably NGC 891, the  $J - K_s$  color also becomes significantly bluer below  $z \sim 0.2$  (where NGC 891’s super-thin disk dominates the light profile).

These results paint a picture consistent with a disk heating scenario in which stars form in a dynamically-cold super-thin gas layer, and diffuse at some rate to less



oblate (thicker, dynamically warmer) distributions. The rate of heating and its discreteness (i.e., whether heating is a continuous or episodic process) are of general interest in understanding how disk galaxies evolve. Determining whether super-thin disks are transient structures—rapidly destroyed by mergers to form the thin and thick disks, or are slowly and continuously evolving components—requires both a larger statistical sample of galaxies and better estimates of stellar ages. The results here suggest that with suitable additional spectrophotometric measurements it may be possible to utilize stellar chronometers to measure the heating rate of disks. At the same time it is also clear that edge-on spiral galaxies contain a significant amount of information on the stellar populations of these systems by virtue of these vertical gradients. In contrast to post star-burst systems used to probe the relative importance of AGB stars in the integrated stellar populations of galaxies (e.g., Kriek et al. 2010, Zibetti et al. 2013), where the young component may contribute only a small fraction of the near-infrared light, here we are utilizing the unique geometry of disk vertical structure to probe a significant dynamic range in mean stellar population age.

Overall this work has shown that while the MW’s vertical structure is clearly not unique, the local universe contains a wide range of disk structure even for intermediate-type, fast-rotating systems. The limiting factor in ob-

taining a statistical understanding of this structure is the relative small number of galaxies which are close enough to edge on and nearby enough to be adequately resolved. Better resolution imaging data, particularly in the mid-infrared, should be possible with the *James Webb Space Telescope* (JWST) NIRCAM instrument.<sup>17</sup> With the advent of JWST, a much increased volume will become available for this kind of study, yielding the larger sample sizes necessary to probe the diversity of disk structure and potentially the fossil record of disk heating.

This research was directly supported by the U.S. National Science Foundation (NSF) AST-1009471. MAB acknowledges the generous hospitality of the Institute for Cosmology and Gravitation (University of Portsmouth) and financial support of the Leverhulme Foundation. The authors are grateful to John MacLachlan for sharing his NGC 4244 data, and Arthur Eigenbrot for his significant assistance with data collection. Computational support came from the UW-Madison Department of Computer Sciences Center For High Throughput Computing (CHTC), supported by the Wisconsin Alumni Research Foundation, the NSF and the U.S. Department of Energy Office of Science as part of the Open Science Grid. We also made use of SDSS and 2MASS<sup>18</sup>, databases and archives.

#### REFERENCES

- Abadi, M. G., Navarro, J. F., Steinmetz, M., & Eke, V. R. 2003, *ApJ*, 597, 21
- Aoki, T. E., Hiromoto, N., Takami, H., & Okamura, S. 1991, *PASJ*, 43, 755
- Aumer, M., & Binney, J. J. 2009, *MNRAS*, 397, 1286
- Baes, M., & Gentile, G. 2011, *A&A*, 525, A136
- Baggett, W. E., Baggett, S. M., & Anderson, K. S. J. 1998, *AJ*, 116, 1626
- Bershady, M. A. 1995, *AJ*, 109, 87
- Bershady, M. A., Martinsson, T. P. K., Verheijen, M. A. W., et al. 2011, *ApJ*, 739, L47
- Bershady, M. A., Verheijen, M. A. W., Swaters, R. A., et al. 2010a, *ApJ*, 716, 198
- Bershady, M. A., Verheijen, M. A. W., Westfall, K. B., et al. 2010b, *ApJ*, 716, 234
- Bessell, M. S., & Brett, J. M. 1988, *PASP*, 100, 1134
- Bianchi, S. 2008, *A&A*, 490, 461
- Bird, J. C., Kazantzidis, S., Weinberg, D. H., et al. 2013, *ApJ*, 773, 43
- Boquien, M., Calzetti, D., Combes, F., et al. 2011, *AJ*, 142, 111
- Bottema, R., Shostak, G. S., & van der Kruit, P. C. 1987, *Nature*, 328, 401
- Bovy, J., Rix, H.-W., Liu, C., et al. 2012, *ApJ*, 753, 148
- Bruzual, G., & Charlot, S. 2003, *MNRAS*, 344, 1000
- Burnham, K. P., & Anderson, D. R. 2002, *Model selection and multimodel inference: a practical information-theoretic approach* (Springer)
- Buta, R. 1990, *ApJ*, 351, 62
- Cappellari, M., & Copin, Y. 2003, *MNRAS*, 342, 345
- Cardelli, J. A., Clayton, G. C., & Mathis, J. S. 1989, *ApJ*, 345, 245
- Carpenter, J. M. 2001, *AJ*, 121, 2851
- Chiaberge, M., Gilli, R., Macchetto, F. D., & Sparks, W. B. 2006, *ApJ*, 651, 728
- Comerón, S., Knapen, J. H., Sheth, K., et al. 2011a, *ApJ*, 729, 18
- Comerón, S., Elmegreen, B. G., Knapen, J. H., et al. 2011b, *ApJ*, 738, L17
- . 2011c, *ApJ*, 741, 28
- Connolly, A. J., Szalay, A. S., Bershady, M. A., Kinney, A. L., & Calzetti, D. 1995, *AJ*, 110, 1071
- Dalcanton, J. J., & Bernstein, R. A. 2000, *AJ*, 120, 203
- Dalcanton, J. J., Yoachim, P., & Bernstein, R. A. 2004, *ApJ*, 608, 189
- de Looze, I., Baes, M., Bendo, G. J., et al. 2012, *MNRAS*, 427, 2797
- Du, Q., Faber, V., & Gunzburger, M. 1999, *SIAM Review*, 41, 637
- Eggen, O. J., Lynden-Bell, D., & Sandage, A. R. 1962, *ApJ*, 136, 748
- Elmegreen, B. G., & Elmegreen, D. M. 2006, *ApJ*, 650, 644
- Fioc, M., & Rocca-Volmerange, B. 1997, *A&A*, 326, 950
- Förster Schreiber, N. M., Genzel, R., Bouché, N., et al. 2009, *ApJ*, 706, 1364
- Freeman, K. C. 1970, *ApJ*, 160, 811
- Frogel, J. A., Persson, S. E., Matthews, K., & Aaronson, M. 1978, *ApJ*, 220, 75
- Frogel, J. A., & Whitford, A. E. 1987, *ApJ*, 320, 199
- Fry, A. M., Morrison, H. L., Harding, P., & Boroson, T. A. 1999, *AJ*, 118, 1209
- Gonzalez, O. A., Rejkuba, M., Zoccali, M., et al. 2013, *A&A*, 552, A110
- Holwerda, B. W., Bianchi, S., Böker, T., et al. 2012, *A&A*, 541, L5
- Hopkins, P. F., Cox, T. J., Younger, J. D., & Hernquist, L. 2009, *ApJ*, 691, 1168
- Hawk, J. C., & Savage, B. D. 1997, *AJ*, 114, 2463
- . 1999, *AJ*, 117, 2077
- Jarrett, T. H., Chester, T., Cutri, R., Schneider, S. E., & Huchra, J. P. 2003, *AJ*, 125, 525
- Jones, T. J. 1989, *AJ*, 98, 2062
- Kamphuis, P., Holwerda, B. W., Allen, R. J., Peletier, R. F., & van der Kruit, P. C. 2007, *A&A*, 471, L1
- Kazantzidis, S., Bullock, J. S., Zentner, A. R., Kravtsov, A. V., & Moustakas, L. A. 2008, *ApJ*, 688, 254
- Kormendy, J. 1977, *ApJ*, 217, 406
- Kormendy, J., & Barentine, J. C. 2010, *ApJ*, 715, L176
- Kotulla, R., Fritze, U., Weilbacher, P., & Anders, P. 2009, *MNRAS*, 396, 462
- Kriek, M., Labbé, I., Conroy, C., et al. 2010, *ApJ*, 722, L64
- Leroy, A. K., Walter, F., Brinks, E., et al. 2008, *AJ*, 136, 2782

<sup>17</sup> <http://jwst.nasa.gov/nircam.html>.

<sup>18</sup> <http://www.ipac.caltech.edu/2mass/releases/allsky/>

- MacLachlan, J. M., Matthews, L. D., Wood, K., & Gallagher, J. S. 2011, *ApJ*, 741, 6
- Maraston, C. 2005, *MNRAS*, 362, 799
- Martínez-Delgado, D., Pohlen, M., Gabany, R. J., et al. 2009, *ApJ*, 692, 955
- Martinsson, T. P. K., Verheijen, M. A. W., Westfall, K. B., et al. 2013, *A&A*, 557, A130
- Matthews, L. D. 2000, *AJ*, 120, 1764
- Meixner, M., Smee, S., Doering, R. L., et al. 2010, *PASP*, 122, 451
- Morrison, H. L., Boroson, T. A., & Harding, P. 1994, *AJ*, 108, 1191
- Morrison, H. L., Miller, E. D., Harding, P., Stinebring, D. R., & Boroson, T. A. 1997, *AJ*, 113, 2061
- Mucciarelli, A., Origlia, L., Ferraro, F. R., Maraston, C., & Testa, V. 2006, *ApJ*, 646, 939
- Olling, R. P. 1996, *AJ*, 112, 457
- Omohundro, S. M. 1989, *Five Balltree Construction Algorithms*, Tech. Rep. TR-89-063, International Computer Science Institute
- Patrel, G., Petit, C., Prugniel, P., et al. 2003, *A&A*, 412, 45
- Persson, S. E., Aaronson, M., Cohen, J. G., Frogel, J. A., & Matthews, K. 1983, *ApJ*, 266, 105
- Puech, M., Hammer, F., Hopkins, P. F., et al. 2012, *ApJ*, 753, 128
- Purcell, C. W., Kazantzidis, S., & Bullock, J. S. 2009, *ApJ*, 694, L98
- Rayner, J. T., Cushing, M. C., & Vacca, W. D. 2009, *ApJS*, 185, 289
- Rhee, M.-H., & van Albada, T. S. 1996, *A&AS*, 115, 407
- Rice, W., Merrill, K. M., Gatley, I., & Gillett, F. C. 1996, *AJ*, 112, 114
- Robitaille, T. P. 2011, *A&A*, 536, A79
- Ruff, K. M., Howk, J. C., Pitterle, M., et al. 2013, *AJ*, 145, 62
- Sanders, D. B., Mazzarella, J. M., Kim, D.-C., Surace, J. A., & Soifer, B. T. 2003, *AJ*, 126, 1607
- Schechtman-Rook, A., & Bershady, M. A. 2013, *ApJ*, 773, 45
- Schechtman-Rook, A., Bershady, M. A., & Wood, K. 2012, *ApJ*, 746, 70
- Seon, K.-i., Witt, A. N., Shinn, J.-h., & Kim, I.-j. 2014, *ApJ*, 785, L18
- Seth, A. C., Dalcanton, J. J., & de Jong, R. S. 2005, *AJ*, 130, 1574
- Shaw, M. A., & Gilmore, G. 1989, *MNRAS*, 237, 903
- Sofue, Y., & Nakai, N. 1994, *PASJ*, 46, 147
- Terndrup, D. M., Davies, R. L., Frogel, J. A., Depoy, D. L., & Wells, L. A. 1994, *ApJ*, 432, 518
- Thain, D., Tannenbaum, T., & Livny, M. 2005, *Concurrency - Practice and Experience*, 17, 323
- Thilker, D. A., Bianchi, L., Meurer, G., et al. 2007, *ApJS*, 173, 538
- Tokunaga, A. T. 2000, *Infrared Astronomy*, ed. A. N. Cox, 143
- van den Bergh, S., & Pierce, M. J. 1990, *ApJ*, 364, 444
- van der Kruit, P. C. 1984, *A&A*, 140, 470
- Villalobos, Á., & Helmi, A. 2008, *MNRAS*, 391, 1806
- Walker, I. R., Mihos, J. C., & Hernquist, L. 1996, *ApJ*, 460, 121
- Westfall, K. B., Bershady, M. A., Verheijen, M. A. W., et al. 2011, *ApJ*, 742, 18
- Wu, H., Burstein, D., Deng, Z., et al. 2002, *AJ*, 123, 1364
- Yoachim, P., & Dalcanton, J. J. 2006, *AJ*, 131, 226
- York, D. G., Adelman, J., Anderson, Jr., J. E., et al. 2000, *AJ*, 120, 1579
- Zibetti, S., Gallazzi, A., Charlot, S., Pierini, D., & Pasquali, A. 2013, *MNRAS*, 428, 1479
- Zschaechner, L. K., Rand, R. J., Heald, G. H., Gentile, G., & Kamphuis, P. 2011, *ApJ*, 740, 35

## APPENDIX

## NGC 4244 ATTENUATION CORRECTION

Multiple authors have fit RT models to NGC 4244, two notable recent efforts being that of MacLachlan et al. (2011) and Holwerda et al. (2012). We use the results from these works as starting points for our models, which are run using HYPERION (Robitaille 2011). To obtain input SEDs we use the method of Bianchi (2008), splitting a PEGASE (Fioc & Rocca-Volmerange 1997) synthesis model of a spiral galaxy into high-mass and low-mass components (as a proxy for young and old stars, respectively). For NGC 4244 we find that a Sc galaxy model at only 3 Gyr after formation provides the best fit to the data, an indication of the relative youth of this galaxy's stellar population. Additionally, unlike for NGC 891, we find that a lower dust density threshold for the addition of young stars to a grid cell is not required to reproduce the SED (shown in Figure 30). A list of the relevant parameters used in our fit is shown in Table 12.

To compute the attenuation correction we use the same technique as in Paper 1, producing model images with and without dust and taking the ratio. The ratio image is compared to a ( $K_s - 4.5\mu\text{m}$ ) image on a pixel-by-pixel basis. We then fit this relationship. NGC 891 required a piecewise fit, where pixels with  $(K_s - 4.5\mu\text{m}) < 1.3$  were well fit by a fourth order polynomial and pixels with redder colors followed a linear trend. For NGC 4244, since there is much less attenuation, there are no pixels with  $(K_s - 4.5\mu\text{m}) > 1.3$ , so we just fit the fourth-order polynomial (note that these fits are for the dust distribution called Model A in Paper 1). The spectra used for this modeling have intrinsic colors of  $(K_s - 4.5\mu\text{m}) \sim 0$ . To make this fully general for any intrinsic  $(K_s - 4.5\mu\text{m})$  color, however, we formulate these relations in terms of the color excess  $E(K_s - 4.5\mu\text{m})$ , as discussed in the text:

$$A_J^e = -0.03 + 1.12 \times E(K_s - 4.5\mu\text{m}) + 7.42 \times E(K_s - 4.5\mu\text{m})^2 - 26.44 \times E(K_s - 4.5\mu\text{m})^3 + 29.82 \times E(K_s - 4.5\mu\text{m})^4 \quad (\text{A1})$$

$$A_H^e = -0.01 + 0.67 \times E(K_s - 4.5\mu\text{m}) + 4.92 \times E(K_s - 4.5\mu\text{m})^2 - 16.41 \times E(K_s - 4.5\mu\text{m})^3 + 18.35 \times E(K_s - 4.5\mu\text{m})^4 \quad (\text{A2})$$

$$A_{K_s}^e = -0.01 + 0.40 \times E(K_s - 4.5\mu\text{m}) + 3.24 \times E(K_s - 4.5\mu\text{m})^2 - 10.27 \times E(K_s - 4.5\mu\text{m})^3 + 11.33 \times E(K_s - 4.5\mu\text{m})^4. \quad (\text{A3})$$

Note that some of the higher-order coefficients on these fits are very large. This is because the models have  $\sim$ zero pixels with  $(K_s - 4.5\mu\text{m}) \gtrsim 0.4$  mag. Therefore these fits should *not* be used to correct any data with  $(K_s - 4.5\mu\text{m})$  colors redder than this, as the correction function will be erroneously dominated by these large high-order terms. A graphical representation of these corrections is overlaid on top of the model pixels used in the fit in Figure 31 along

TABLE 12  
NGC 4244 RT MODEL PARAMETERS

Parameter	Value	Units
Thin disk bolometric luminosity	$2.5 \times 10^9$	$L_{\odot}$
Star-forming disk bolometric luminosity	$1.3 \times 10^9$	$L_{\odot}$
Thin disk scale-length	1.9	kpc
Star-forming disk scale-length	3.4	kpc
Thin disk scale-height	0.2	kpc
Star-forming disk scale-height	0.2	kpc
Dust disk central density	$1.1 \times 10^{-26}$	$\text{g cm}^{-3}$
Dust disk scale-length	3.4	kpc
Dust disk scale-height	0.2	kpc
Dust clumping fraction	0.5	
Number of largest-scale clumps	130	

with the fit used in Paper 1<sup>19</sup>. We also show  $E(J - K_s)$  as a function of  $A_{K_s}^e$  for our attenuation corrections as well as the foreground screen model of Cardelli et al. (1989) in Figure 16.

While the PEGASE models provide a good fit, we also investigated the GALEV (Kotulla et al. 2009) models used by MacLachlan et al. (2011, private communication). We found that with the GALEV spectra the only way to produce a model that properly fit NGC 4244’s SED around  $5 \mu\text{m}$  was to decrease the fraction of PAHs in the model by a factor of  $\sim 4$ . The SED of that model is shown alongside our PEGASE model in Figure 30.

A dust distribution different from that found in the MW is not necessarily a problem, as low-mass spiral galaxies are known to have different metallicities than their high-mass counterparts (van den Bergh & Pierce 1990; Dalcanton et al. 2004) which would naturally result in a different grain distribution. However, while the shape of the attenuation corrections are very similar, the GALEV models also predict different intrinsic stellar ( $K_s - 4.5 \mu\text{m}$ ) colors. Because our new attenuation correction method only relies on the shape of the attenuation correction and uses SSPs to compute the attenuation zeropoints, the use of either input SEDs will therefore produce very similar results. To maximize consistency between our methodology between our galaxies, we choose to use the correction resulting from the PEGASE model. Ultimately, however, we show in Section 6.1 that the slow-rotating galaxies have negligible  $K_s$ -band attenuation over their entire disks, rendering the choice of attenuation correction largely academic in this work.

<sup>19</sup> Note that there is a typo in Appendix C of Paper 1. The

equation for  $A_{\text{H}}^e$  of Model B when  $(K_s - 4.5 \mu\text{m}) > 1.3$  should read  $1.75(K_s - 4.5 \mu\text{m}) + 0.22$ .

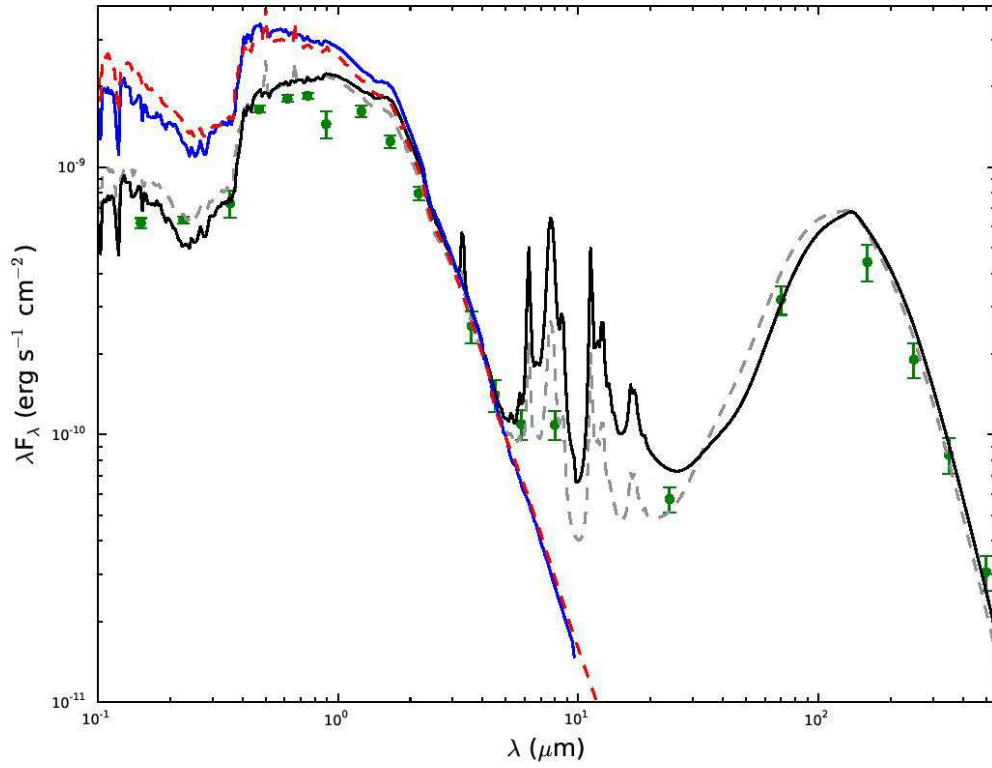


FIG. 30.— Model SEDs for NGC 4244. Green points show data and are the same as in MacLachlan et al. (2011). The blue solid line shows the input SED using the PEGASE stellar library, while the black solid line shows the corresponding HYPERION-processed output SED. The red and gray dashed lines show the input and output SEDs (respectively) from the GALEV evolutionary synthesis model (including the PAH reduction discussed in the text).

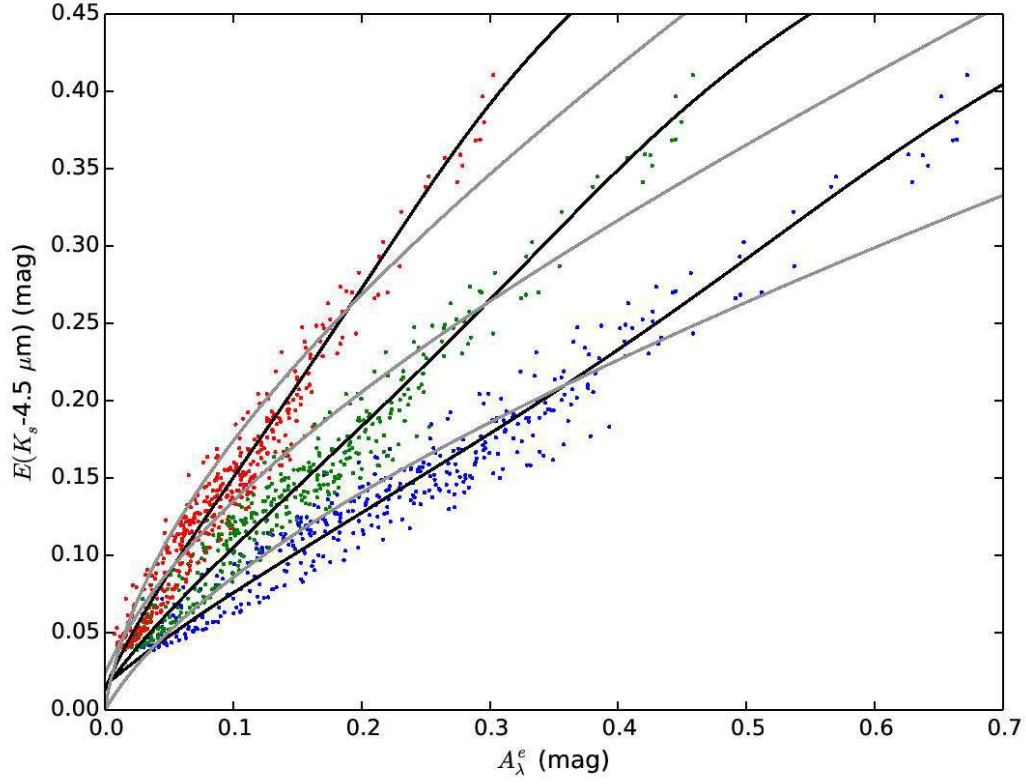


FIG. 31.—  $A_{\lambda}^e$  as a function of  $K_s-4.5\mu\text{m}$  color. Blue, green, and red points show individual J, H, and  $K_s$  model pixels, while black lines show the best-fit lines to those pixels. Gray lines show the best fits for NGC 891 using dust Model B in Paper 1. The differences between the two models (especially at low attenuation) are mainly due to the fact that, even though the same stellar library was used for both fits, the input SED for NGC 4244 is much younger than NGC 891.